2015

Density-Functional Theory+Dynamical Mean-Field Theory Study of the Magnetic Properties of Transition-Metal Nanostructures

Alamgir Kabir
University of Central Florida

STARS Citation
Kabir, Alamgir, "Density-Functional Theory+Dynamical Mean-Field Theory Study of the Magnetic Properties of Transition-Metal Nanostructures" (2015). *Electronic Theses and Dissertations, 2004-2019*. 1424.
https://stars.library.ucf.edu/etd/1424

DENSITY-FUNCTIONAL THEORY+DYNAMICAL MEAN-FIELD THEORY STUDY OF THE MAGNETIC PROPERTIES OF TRANSITION-METAL NANOSTRUCTURES

by

ALAMGIR KABIR
B.Sc. University of Dhaka, Bangladesh 2001
M.Sc. University of Dhaka, Bangladesh 2003

A dissertation submitted in partial fulfillment of the requirements
for the degree of Doctor of Philosophy
in the Department of Physics
in the College of Science
at the University of Central Florida
Orlando, Florida

Spring Term
2015

Major Professor: Talat S. Rahman

ABSTRACT

In this thesis, Density Functional Theory (DFT) and Dynamical Mean-Field Theory (DMFT) approaches are applied to study the magnetic properties of transition metal nanosystems of different sizes and compositions. In particular, in order to take into account dynamical electron correlation effects (time-resolved local charge interactions), we have adopted the DFT+DMFT formalism and made it suitable for application to nanostructures. Preliminary application of this DFT+DMFT approach, using available codes, to study the magnetic properties of small (2 to 5-atom) Fe and FePt clusters provide meaningful results: dynamical effects lead to a reduction of the cluster magnetic moment as compared to that obtained from DFT or DFT+U (U being the Coulomb repulsion parameter). We have subsequently developed our own nanoDFT+DMFT code and applied it to examine the magnetization of iron particles containing10-147 atoms. Our results for the cluster magnetic moments are in a good agreement with experimental data. In particular, we are able to reproduce the oscillations in magnetic moment with size as observed in the experiments. Also, DFT+DMFT does not lead to an overestimation of magnetization for the clusters in the size range of 10-27 atoms found with DFT and DFT+U. On application of the nanoDFT+DMFT approach to systems with mixed geometry – Fe_2O_3 film, which are periodic (infinitely extended), in two directions, and finite in the third. Similar to DFT+U, we find that the surface atom magnetic moments are smaller compared to the bulk. However, the absolute values of the surface atoms magnetic moments are smaller in DFT+DMFT. In parallel, we have carried out a systematic study of magnetic anisotropy in bimetallic $L1_0$ FePt nanoparticles (20-484 atoms) by using two DFT-based approaches: direct and the torque method. We find that the magnetocrystalline anisotropy (MCA) of FePt clusters is larger than that of the pure Fe and Pt ones. We explain this effect by a large hybridization of 3d Fe- and 5d Pt-atom orbitals, which lead to enhancement of the magnetic moment of the Pt atom, and hence to a larger magnetic anisotropy because of large spin-orbit coupling of Pt atoms. In addition, we find that particles whose (large) central layer consists of Pt atoms, rather than Fe, have larger MCA due to stronger hybridization effects. Such ‘protected’ MCA, which does not require protective cladding, can be used in modern magnetic technologies.

ACKNOWLEDGMENTS

First and Foremost I would like to thank my advisor Dr. Talat S. Rahman, without her support and guidance this work would not have been possible. All her personal and professional support helped me to give more time and work hard during my research. Her critical way of thinking about a problem, scientific criticism about my project, useful advises and thoughtful suggestions helps me to learn the way of scientific approach much better. Last and nevertheless her critical way of reviewing my writing for scientific journals helps me to learn the way of writing.

I am most grateful to the members of my committee, Dr. Abdelkader Kara, Dr. Enrique del Barco and Dr. Pieter G. kik for their time, and expertise throughout this study.

I am very grateful to Dr. Volodymyr Turkowski for his support in all the projects I have worked on, for his generosity, helpful scientific discussions and efforts to make things simple and transparent for me to understand in several projects during my PhD study. I would also like to thank Dr. Duy Le who has always patiently answered all my queries and helped learning many computational techniques. Thanks to all the group members, students and post-docs, T. Rawal, G. Shafai Erfani, Dr. M. Aminpour, Dr. S. I. Shah, Z. Hooshmand, S. Acharya, Dr. M. A. Ortigoza, Dr. S. Hong, Dr. A. Ramirez for their support and fruitful discussions

I sincerely want to thank Dr. Lyman Baker for his invaluable comments and discussions on all my publications and projects.

I would also like to thanks, the Department of Physics, University of Dhaka, Bangladesh for granting my study leave from the department to pursue my PhD.

Lastly, I would like to thank my family for all their immense love and support. Specially my parents, the care and support they have given to me is basically made me what I am today. I am very sorry to say that I lost both of my parents while I was working on my PhD. Both of my parents would be very happy today to see my works, but unfortunately they are no more in this world. I hope their souls are watching everything here and they are still praying for me.

Finally my deepest thanks to my loving wife Shahida Parvin, without her constructive way of maintaining my family I could not do any work. She give all her time and thinking to our daughters so that I can work peacefully and uninterruptedly. My heartiest love to our daughter Anisha T. Kabir and Sarah T. Kabir.

TABLE OF CONTENTS

LIST OF FIGURES

LIST OF TABLES

CHAPTER 1 INTRODUCTION

1.1 Strong electron-electron correlations and magnetism

Strongly correlated materials, which contain active localized d- and f-electronic orbitals, remain at the forefront of condensed matter and material physics research. Electron-electron correlations and the interplay between electronic, magnetic and structural degrees of freedom lead to incredibly rich phenomena[1]. Metal-insulator transition, heavy fermion phenomena, colossal magnetoresistance, and high temperature superconductivity take place in this class of systems with localized charge orbitals. From the perspective of basic science, these materials are fascinating precisely because of the richness of emergent phenomena due to high tenability of their properties (changing temperature, pressure, doping, etc.). The low-energy excitations in some of the materials are very different from the “standard” ones, demonstrating for example separation of charge and spin degrees of freedom and being genuinely collective in nature (for over-review of general properties of strongly correlated materials see, for example,[2]). In general, strong local interactions between the electrons in this type of bulk materials result in properties vastly different from those observed in the weakly-correlated systems.

The case of strongly correlated nanostructures is even more interesting, due to possibility to tune their properties by changing the system size and geometry. In this way one can change the material properties, by making them different from the bulk and very small systems, like clusters and molecules. The comparable number of surface and bulk atoms in the nanosystems allow to tune their properties, that include both surface and bulk features. The size-dependent evolution of the properties of nanostructures makes them very interesting from both theoretical and practical points of view.

Changing chemical composition of correlated nanosystems is another way to tune their already rich properties. [3] Synergistic effect of different factors, such as size, shape and chemical composition, that lead to very unusual properties of nanomaterials, has led to their widespread applications in catalysis[4], nanoelectronics[5], biomedicine[6,7], etc. Properties of nanomagnets, in most of which strongly correlated effects play an important role, are one of most active areas of research in nanoscience. One of the main reasons for this is the dramatically enhanced magnetic moments in nanosized particles, of Fe, Co and Ni, [8] and magnetic anisotropy[9] compared to the bulk values. These effects can be further enhanced in the case of nanoalloys. One of the major potential applications for magnetic nanoparticles is their use in data storage, triggered in particular by the discovery of spontaneous self-organization of magnetic FePt nanoparticles on a surface[10]. The underlying idea is to replace the comparatively large randomly oriented magnetic grains in conventional media with much smaller ferromagnetic nanoparticles, which may lead to a dramatic increase of the magneto-recording density. FePt nanoparticles due to their magnetic hardness are currently identified as the material of choice in this technological area.

Magnetic nanoparticles show promise for other modern and future technological applications, as in magnetic resonance imaging techniques,[11] drug carries[12] and cancer therapy[13] in medicine, and energy-harvesting technologies [14].

From the perspective of basic science, nanomaterials are fascinating precisely because their electronic and magnetic properties are quite different from their bulk counterparts, especially in the strongly correlated case. In order to explain these and predict new properties of correlated systems one needs to use suitable theoretical tools. In the case of nanostructures the situation gets even more complicated due to technical difficulties related to a large number of nonequivalent atoms in the system. Another complication comes from lack of knowledge of the exact structure of the particles in majority of cases, which constraints the theoretical studies of transition metal and other strongly correlated nanosystems in the empirical trial and error framework. In order to get rid of this difficulty, it is necessary to improve the techniques for generating interatomic potentials which will allow accurately prediction of particle structures by establishing the minimum energy configurations [10,15,16]. However, probably the most difficult task in correct description of the properties of strongly correlated nanostructures, similar to the bulk case, is accurately taking into account electron interaction effects. Standard DFT approaches, invoking the Local Density Approximation (LDA) and Generalized Gradient Approximation (GGA) are inappropriate, since the corresponding exchange-correlation (XC) potentials fail in the strongly correlated regime.[17] For example, GGA calculations predict bulk V_2O_3 to be metallic, whereas experimentally it is found to be an insulator[18]. Perhaps, the simplest way to take into account correlation effects beyond DFT is the DFT+U approximation[19]. In this approach one uses a phenomenological parameter U, which corresponds to the local on-site electron-electron repulsion energy. The U correction allows one to improve the DFT results in describing some properties of materials, such as the correct value of the bandgap. However, being essentially a mean-field approximation, DFT+U is not capable of reproducing many other properties of correlated systems. Some of the examples of failure of DFT+U include missing important peaks in the electronic spectral function[17] and wrong predictions of spin-ordering temperatures [20].

It has been shown during the last 10-15 years, that the majority of the deficiencies of the DFT+U solution can be overcome if one takes into account dynamical fluctuations, i.e. time-resolved electron-electron interactions. The corresponding theory, which takes into account temporal fluctuations but neglects the spatial ones (hence valid for systems with large atomic coordination number[21]), is called dynamical mean field theory (DMFT).[20,22,23] This theory combined with DFT (and called DFT+DMFT) allows one to reproduce majority of strongly correlated effects in most extended systems.[20] The details of the DFT+DMFT approach are given in Chapter 3.

In this thesis we present our generalization and applications of the DFT+DMFT formalism to study nanomagnets and demonstrate that it can be successfully used in this case as well.

1.2 Magnetism in extended systems

Localized orbitals and magnetism In solids, the outer electrons experience an electric field produced by the inner electrons and nuclei, and depending on the value of the angular momentum and some other parameters, these electrons can be either ”localized” or can move (be “itinerant”) in the presence of the field. In many transition metal systems the outer shell d-electrons are localized because of this effect. These localized electrons play crucial role in determining the magnetic properties of materials. Because of this importance of electron localization for magnetism, let us briefly formulate the criteria of localization in terms of the effective external potential, that consists of nuclei attraction and centrifugal repulsion terms, which acts on the electrons. The centrifugal part (potential for electrons moving around the nucleus) is defined by quantum mechanical angular momentum operator $L = \sqrt{\hbar^2 l(l+1)}$ (with l being orbital angular momentum quantum number of electrons), and is equal to $\frac{\hbar^2 l(l+1)}{2m_e r^2}$, where m_e is the electron mass and r is the radius of the electronic “orbital”. The Coulomb attractive potential between electron and nucleus has the standard form and is equal to $-\frac{Z^* e^2}{4\pi\epsilon_0 r}$, where Z^* is the effective nuclear charge $Z^* = Z - \sigma$ (σ is the screening parameter).[24] Therefore, the effective potential for an electron moving around the nucleus is

$$V_{eff}(r) = -\frac{Z^* e^2}{4\pi\epsilon_0 r} + \frac{\hbar^2 l(l+1)}{2m_e r^2}. \tag{1.1}$$

It follows from equation (1.1) that, the effective potential strongly depends on the value of the orbital momentum, which is one of the reasons for rather different orbital radius for d- and f-electrons as compared to that for the s- and p-states. A typical case of the different orbital charge density and effective potential dependencies on the distance from the center of the ion are shown in Fig 1. As it follows from Fig. 1, the 3d-electron charge density has maxima much closer to the nucleus whereas for 4p- and 4s-densities are further away.

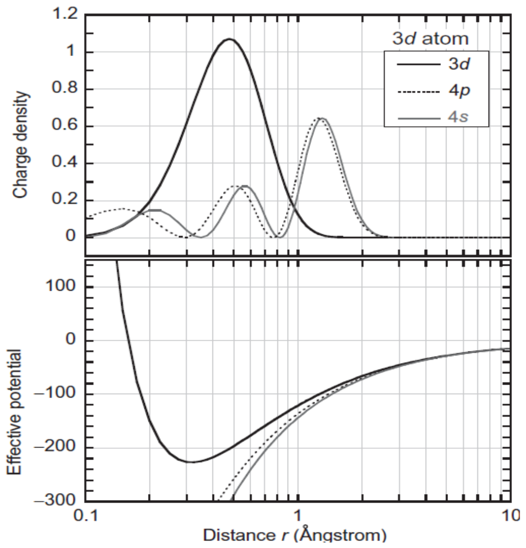

Figure 1: Radial dependencies of the charge density and effective potential a 3d transition metal atom with effective charge number Z*=10 (from Ref. [25]).

In other words, the atomic charge density and potential showed in the Fig. 1 confirm the statement of more localized charge density behavior for the d-orbital, while the other two orbital charges can be regarded as itinerant.

The localized charge approximation can be used to analyze the magnetic properties of systems by using Hund's rules applied to individual atoms. According to Hund, the states in the atom are filled by electrons first for one spin direction from largest to smallest (-L to L) value of the orbital momentum and then backwards for opposite spins (L to -L). Such an approximation allows one to get a first-try estimation for the magnetic moments in many systems, however it does not lead to an accurate quantitative description of magnetism in most of materials, in particular due to strictly integer values of the magnetic moment. (in units of Bohr magneton μ_B). For example, in the case of Fe with 6 electrons in the 3d orbital and 2 electrons in 4s orbital, the Hund's rules give the spin arrangement as given in Fig. 2

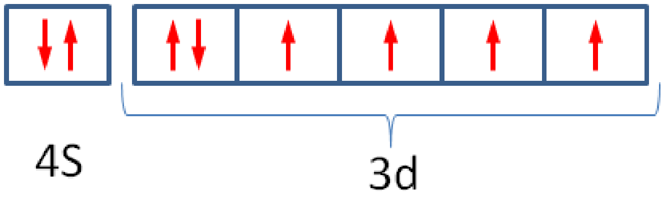

Figure 2 : The schematic of spin configuration of Fe according to the Hund's rule. Arrows indicate the spin direction.

Thus, the bulk Fe should have spin moment 4 μ_B, and similarly Co and Ni should have moments 3 μ_B and 2 μ_B, respectively. However, the experimental values for the magnetic moments in Fe, Co and Ni are 2.216 μ_B, 1.715 μ_B and 0.616 μ_B, correspondingly. [25] Inclusion of the orbital moments according to Hund's rule gives even higher magnetic moments of 6 μ_B, 6 μ_B and 5 μ_B for Fe, Co and Ni, respectively. This means that atomic model (localized electron) leads to a serious overestimation of the magnetic moments of the bulk transition metals, and one needs to go beyond it in order to describe the magnetism in a realistic manner.

The band theory of magnetism. An alternative to the local electron approximation is the band theory of magnetism, in which collective effects of many-electron system are taken into account. Due to inter-atomic hopping of electrons in solids (defined by overlap of the wave functions of electrons on different atoms) their electronic energy levels form bands of continuously filled states, which are described by the electron momentum vector k. Since the position of bands for opposite spin electrons may be shifted with respect to each other, one can have different number of spin up and spin down electrons in the system (states are filled beginning with lowest energy states). Therefore, one can explain the non-zero magnetic moment of the system also in terms of the band occupancies. This band theory was first applied to magnetic systems in mid-1930-ies by Mott[26], Slater[27] and Stoner[28,29], in the framework later called the Stoner Model. A remarkable success of this model is its ability to describe the magnetic moments of the system with non-integer Bohr magneton numbers. The idea of non-integer filled bands and how this result in continuous values for the magnetic moments can be obtained from Fig.3

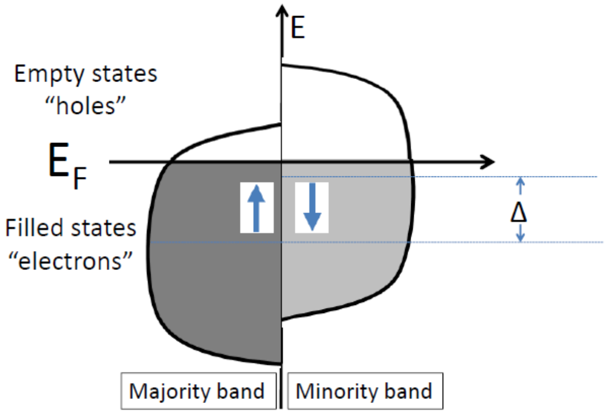

Figure 3: The shaded region represent filled electronic band below the Fermi energy and the empty band above the Fermi are represented by un-shaded region. The center of majority and minority spin band are separated by exchange splitting Δ. The quantization direction is taken to be parallel to the external field.

In the simplest case of zero temperature, all electronic states below the Fermi level are filled. Due to different position of the majority (spin-up) and minority (spin-down) bands with respect to the Fermi level, one can get a non-zero spin moment in the system. The moment is defined by difference of the number of majority and minority spins in the system:

$$N_e^{\downarrow} - N_e^{\uparrow} = \int_{-\infty}^{E_F} D^{\downarrow}(E)dE - \int_{-\infty}^{E_F} D^{\uparrow}(E)dE, \tag{1.2}$$

where $D(E)$ are the corresponding spin densities of states. More precisely, the magnetic moment is equal to $m = -2\mu_B \langle s_z \rangle /\hbar$, where $\langle s_z \rangle$ is the average spin in units of $\hbar$ (the negative electron charge gives gyromagnetic ratio (-2) for electron). Then, the expectation value of electron spin towards the quantization axis-z can be written as

$$m = -2\mu_B \langle s_z \rangle \frac{1}{\hbar} = \mu_B \left(N_e^{\uparrow} - N_e^{\downarrow}\right). \tag{1.3}$$

The Stoner model does not take into account the detailed dependence of the band energies on the electronic wave vector k, which can be very complicated as discussed, for example, by Hoffmann[30] . Indeed, in general the wave-functions of the multi-orbital systems can be expanded in terms of the momentum-dependent functions proportional to different parts: the radial $(R_{n,l}(r))$, orbital ($Y_{l.m=}|l,m\rangle$, l and m are orbital momentum and its projection) and spin ($\chi^+ =\uparrow, \chi^- =\downarrow$),

$$|\psi_i(k,r)\rangle = \left|R_{n,l}(r)\rangle\right|\varphi_i(k)\rangle = \left|R_{n,l}(r)\right\rangle \textstyle\sum_{m=-l}^{+l}[c_{i,m}(k)|lm\chi^+\rangle + e_{i,m}(k)|lm\chi^-\rangle] \tag{1.4}$$

The equation (1.4) describes a band state in the presence of both exchange and spin-orbit interaction and it is written in Slater-Koster tight binding formalism. [30] Obviously, the diagonalization of the Kohn-Sham equation with such a complex basis wave functions may lead to a rather nontrivial dependence of the energies on momenta.

One most widely used band theoretical approach to study the ground state and the bandstructure of the materials is DFT, which we will discuss in detail later. The success of this theory is based in an approximate but efficient treatment of the interaction and other many-electron effects in terms of an effective one-electron exchange-correlation potential that depends on the total charge density. In the spin version of DFT, one deals with the spin dependent charge densities, which allow studying the magnetic properties of the materials. In many cases, the spin and charge DOS obtained from the DFT bandstructrure calculation is comparable to the experimental data, obtained for example by means of the angle-resolved photoemission spectroscopy (ARPES).[25]

Unfortunately, as it was mentioned in the previous Subsection that, simple DFT-based (i.e. weakly-interacting electron) band theory is not capable to describe the electronic and magnetic properties of a large number of materials. Already in 1937 it was discussed by de Boer and Verwey[31] that the standard band theory cannot explain the insulating nature of many oxides. The same year Mott[32] suggested that strong electron-electron correlations are responsible for insulating nature of these systems, which started a new branch of solid state theory called physics of strongly correlated electrons. In this theory the central parameter is the value of the local electron-electron repulsion U. In the cases in which U is comparable or larger than the electron kinetic energy (proportional to the bandwidth W) local interaction effects are dominating in defining properties of the systems.

For typical metals with W~10-20eV, one can neglect effects of U (which is ~5eV) or less, while for correlated materials with narrow d- (~5eV) or f- (<5eV) bands one cannot avoid U in analyzing the properties of the system, and has to treat U and W on equal footing. Naturally, local interaction effects in these materials affect also their magnetism, in particular through the modification of the bandstructure.

1.3 Magnetism at the nanoscale

Similar to the bulk, in the case of nanosystems role of itinerant (“band”) and localized (“atomic”) electronic states in magnetism can be very nontrivial, and often the interplay between these two types of states define the magnetism in nanomaterials. The analysis is even more complicated in the case of small structures, due to different properties of surface and “bulk” parts of the systems. To build a simplified phenomenological models for nanomagnetism one needs to distinguish contributions of these two types of states as well. Before proceeding with a summary on theoretical developments in the field of nanomagnetism, we start with some characteristic experimental results for these systems.

The magnetic moments of clusters or nanoparticles can be determined, for example, in Stern-Gerlach experiments, in which clusters produced from a molecular beam, are allowed to travel through an inhomogeneous magnetic field. A typical Stern-Gerlach apparatus is shown in Fig. 4.

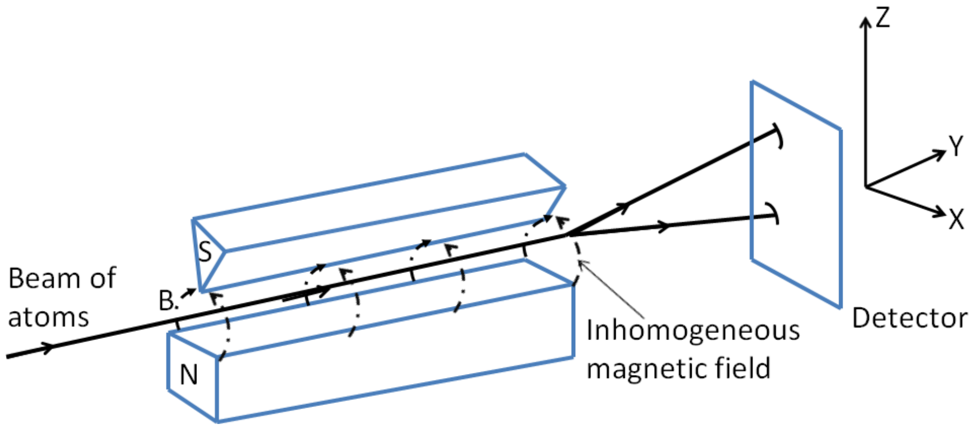

Figure 4: Schematics of Stern-Gerlach experiments. Inhomogeneous magnetic field is created between two uneven bar magnets.

By measuring the deflection of the cluster trajectory in the field one can determine the magnetization of the cluster, M(B), along with the cluster mass by using the time-of-fly mass spectrometer. The deflection of a cluster from its original trajectory due to the magnetic field is given by [8,33]

$$d = K\frac{M(B)}{mv^2}\frac{\partial B}{\partial Z}, \tag{1.5}$$

where v is the velocity of the cluster that moves transverse to the field gradient $\frac{\partial B}{\partial Z}$ direction, m is the mass of the cluster, and K is the apparatus constant, defined by the device geometry. In the case of N-atom cluster approximated by a single ferromagnetic domain its total magnetic moment μ_N defines the cluster magnetization in the presence of the external field B in the following way (at $B/k_BT<<1$):

$$M(B) = \frac{\mu_N^2 B}{3K_B T}. \qquad (1.6)$$

Equations (1.5) and (1.6) determine the total magnetic moment of a cluster μ_N as function of d, m and other experimentally measured parameters .

The experimental results for the magnetic moments of Fe, Ni and Co clusters as function of their size[8,33-35] are presented in Fig.5. As it follows from this Figure, the average magnetic moment per atom $\bar{\mu}$ of the clusters descreases to the bulk value[36] as the system size increases. It appear that the system approaches the bulk limit with about 600-700 atoms in the cluster. In general, however, the size- dependence of the magnetization of the clusters is not easy to understand. Since the surface atoms of the cluster have smaller coordination number compared to the “bulk” atoms, one cannot conclude that all atoms have the same magnetic moment$\overline{\mu} = \frac{\mu_N}{N}$. One also needs to consider the cluster symmetry, inter-atomic distances, electron correlation effects, etc., in order to properly describe the cluster magnetization.

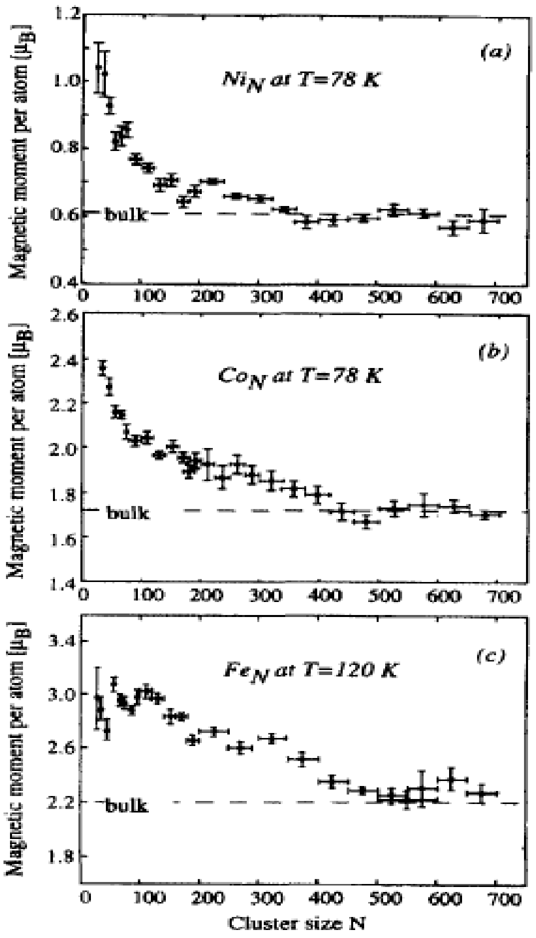

Figure 5: Stern-Gerlach-type experiment data for the magnetic moment per atom for Fe, Co and Ni clusters of different sizes (From Ref. [34]).

Below, we briefly mention some of the popular models to describe results in Fig.5 and other experimental data for nanomagnets.

To explain the decreasing of magnetic moment of the systems with cluster size increasing, Zhao *et al*.[37] proposed to use a tight-binding approximation. In their analysis, they neglected the s- and p-orbital magnetic moments due to their mall values (less than 10% on total magnetization[38]). They have used the Friedel's model[39] approximation for the rectangular d-band spin DOS for the electron at site i with spin σ. [40]:

$$N_i^\sigma(E) = {}^{5}\!/_{W_i} \text{ for } -\tfrac{1}{2}W_i < E - E_d^\sigma < \tfrac{1}{2}W_i \tag{1.7}$$

where E_d^σ represents the center of energy of the corresponding band W_i, which is the same for spin-up and spin-down electrons. In their theory, the authors assumed that the d-band splitting in the cluster, defined by values of E_d^σ for both spins, is same as that of the bulk. In the second-moment approximation, the tight-binding bandwidth is proportional to the square root of the effective coordination number Z_i [40]:

$$W_i = W_b \left({}^{Z_i}\!/_{Z_b} \right)^{1/2}, \tag{1.8}$$

where W_b and Z_b are the bandwidth and the coordination number of the corresponding bulk material. The local magnetic moment $\mu = \int_{-\infty}^{E_F} \left[N_i^\uparrow(E) - N_i^\downarrow(E) \right] dE$ can be written with the help of equation (1.8) as

$$\mu_i = \begin{cases} \left(\frac{Z_b}{Z_i}\right)^{1/2} \mu_{bulk}, & if\ Z_i \geq Z_c \\ \mu_{dimer}, & if\ Z_i < Z_c \end{cases} \tag{1.9}$$

where μ_{bulk} and μ_{dimer} $(> \mu_{bulk})$ are the bulk and the dimer magnetizations and Z_c is the critical coordination number. In general, increasing the particle size leads to an increase of Z_i, which on its turn leads to a decrease of the magnetic moment. Since in the case of very large particles $Z_i = Z_b$, one obtains the bulk magnetic moment for such structures. The average per atom magnetization $\bar{\mu} = \frac{\mu_N}{N}$ depends on the ratio of the numbers of surface and bulk atoms. Indeed, as it follows from equation (1.9) for the surface atoms Z_i is smaller, which reduces the average magnetization of the cluster in the case of many surface atoms.

Jensen and Bennemann have developed several other phenomenological models to explain the size-dependence of magnetization in nanostructures. In Ref.[41] they proposed that the value of the magnetic moment of the cluster can be approximated by the following formula:

$$\bar{\mu} = \mu_b + (\mu_s - \mu_b)N^{-1/3} \tag{1.10}$$

where μ_b and μ_s are the magnetic moment of bulk and surface atoms, and N is the number of atoms in the cluster. This equation gives a decrease of the magnetization with cluster size towards bulk value μ_b, but it cannot explain oscillations of the $\bar{\mu}\,(N)$ curve seen in experiments.[8,33-35] In order to explain these oscillations, one needs to take into account the magnetic properties of individual atoms and the geometry of clusters in more details.

One of the examples of the theory that includes these details is given in works [8,33,34] by Billas *et al*. To explain their experimental data, they assumed that the clusters were formed by several concentric atomic shells and the magnetic moment of the atoms in each shell depends on the distance from the shell to the center of the cluster. According to this model, the atoms in different shells 1, 2, 3, … were assigned different empirical values of magnetic moments $\mu_1, \mu_2, \mu_3, \ldots$. The last values for the magnetization were assumed to be different for different chemical elements. . For example, for Ni the values are: $\mu_1 = 1.2$, μ_2=-0.4, μ_3=0.8… and for Fe: these values are μ_1=3, μ_2=3.2, $\mu_3 = 0$, … (in units of μ_B).[36]. According to the assumptions of the model, the atoms in the outermost shell has larger magnetization compared to the atoms in the inner shells. Unfortunately, this model also cannot reproduce the oscillation in the magnetization as found in the experiments.

Jensen and Bennemann[41] proposed a different type of model that includes atomically-resolved magnetization. According to their model, atoms in the cluster are arranged shell by shell, occupying sites with local fcc or bcc structure and assuming that the clusters can only have cubic, octahedral, cuboctahedral and spherical geometry. In addition to the assumption that different shells have different values of magnetization, they allowed the individual atoms in the outer most shell to have different values of magnetization. The magnetic moments obtained by using this model roughly reproduced the experimental minima for Fe cluster with the bcc structure, which suggests, that the oscillation of the magnetization might be related to the “crystal” structure of the shells. For the outermost shell, it was assumed by Jensen *et al*. that the average magnetization is

$$\bar{\mu}_0 = X_0(1 - X_0)\mu_{at} + {X_0}^2\mu_s \tag{1.11}$$

where X_0 is the concentration of occupied sites (in the bcc, fcc,… configurations), μ_{at} is the free-atom magnetic moment, and μ_s is surface magnetic moment. The magnetic moment bellow the top shell was approximated by

$$\bar{\mu}_1 = (1 - X_0)\mu_s + X_0\mu_{bulk}. \tag{1.12}$$

From equation (1.12) it follows means that the magnetic moment of this shell is equal the surface moment if its atoms have no nearest neighboring atoms in the top shell. On the other hand, it has the bulk magnetic moment if it is completely covered by the top shell atoms. The magnetic moments of the 3rd shell and other shells inside the cluster were assumed to have the bulk value. From equation (1.10) - (1.12), one can obtain the following expression for value of the magnetic moment per atom:

$$\mu(N) = \frac{N_0\bar{\mu}_0 + N_1\bar{\mu}_1 + N_{bulk}\mu_{bulk}}{X_0N_0 + N_1 + N_{bulk}} \tag{1.13}$$

where N_0 is the number of sites in the topmost shell, N_1 is number of sites in the 2nd shell and N_{bulk} is the total number of atoms in the inner shells. The magnetic moment produced from equation (1.12) has minima near closed shell clusters and maxima near the half-filled shell clusters, i.e. the model allows one to describe the oscillation of magnetization to some degree of accuracy.

The phenomenological models based on the “itinerant” and localized electron scenario can explain to a rather limited extent the dependence of the cluster magnetization on number of atoms. Along with these studies numerous ab initio DFT investigations of the magnetic properties of nanostructures [36,42-44] were performed. In particular, some of the results demonstrated ability of DFT to reproduce the oscillations of the magnetic moments with increase of the cluster size.[45] On the other hand, in general the agreement of the DFT results with the experimental data on the absolute values of the magnetization is far from perfect. Similar to bulk, U correction (DFT+U) improves the results in some cases, though one is very far from the conclusion that the DFT+U is sufficient to describe magnetic nanosystems. One possible reason for the failure, one more time similar to the bulk, is neglect of dynamical fluctuation effects in the system.

It has already been suggested by Florens[46] that DMFT, which takes dynamical fluctuations into account, can be used for the nanosystems when the average atomic coordination number in the cluster is large. His justification was based on the fact that in bulk materials with large coordination number DMFT was rather successful in most cases. It is important to note that in DMFT spatial fluctuations are neglected, which might be too crude approximation for small clusters. On the other hand, but since in majority of (not very small) clusters the number of bulk atoms is comparable to the number of surface atoms, one can expect DMFT to be valid in these case as well. Another argument in favor of validity of DMFT in nanocase is applicability of the theory to two dimensions, where the coordination number can be as low as four. [46] This fact and the fact that in nanosystems one can barely have atoms with less than four neighbors (except a few atom-wide chains) suggest that DMFT should be a rather accurate approximation in the nanocase as well.

In this thesis we perform a systematic study of the role of these effects in the magnetic properties of nanostructures. We developed a nanoDFT+DMFT approach and applied it first to small (2-5-atom) Fe [47] and FePt [48] clusters by modifying available codes. We formulated a test of the combined DFT+DMFT approach to study the physical properties of real finite system, in which electron-electron correlation effect has to be taken into account. As already mentioned correlation effects play an important role in the magnetism of transition metal particles. For example, it was shown that inclusion of U into DFT for the Fe dimer leads to significant changes of the values of the Kohn-Sham energies, and hence to a change of the system magnetic moment[49]. The magnetism of small clusters is also very sensitive to the structure geometry. It was shown experimentally[50] that Fe_3 cluster undergoes Jahn-Teller distortion. Rollmann *et al.*[51] applied DFT to analyze possible Jahn-Teller distorted configurations of the Fe_3 clusters. In our analysis, we used some of these distorted cluster structures in our nanoDFT+DMFT calculations in order to understand the interplay between the correlation and distortion effects and their role in the magnetism of Fe clusters. We found that in most clusters DMFT correction leads to a decrease of the magnetic moments obtained by using the DFT or DFT+U approaches, and that the obtained results for the magnetization are in reasonable agreement with available experimental data [52]. Thus, dynamical fluctuation effects (time-resolved on-site electron-electron interaction) result in softening of the magnetic state.

Inspired by this result which suggest that DMFT is able to produce meaningful results even for extremely small clusters, we applied the approach to study the magnetic properties of small bimetallic FePt clusters of 2 to 5 atoms with different chemical compositions[48]. Small bimetallic clusters are excellent systems to understand fundamental interactions and their variation with particle size and compositions (interplay of 3d- and 5d-states in the magnetism), as they are large enough to show the complex behavior and small enough to be treated with accurate theories. FePt clusters are of special interest, because of their high magnetic anisotropy [43,53-56]. The interplay of the Fe and Pt states in the magnetism maybe highly nontrivial. For example, DFT calculations by Boufala *et al*.[53] showed that both Fe and Pt atoms experience enhancement of the magnetic moments when coupled together (in dimer and larger clusters). Similar to the Fe case, we have found that DFT+DMFT significantly reduced the cluster magnetization compared to DFT or DFT+U. Increase of the number of Pt atoms in the 5-atom FePt clusters lead to a decrease of the magnetization. However, contrary to the case of bulk we have found pure Pt_5 clusters to be magnetic.

We extended the nanoDFT+DMFT approach, developed our own code, and applied it to the case of larger (up to 147-atom) Fe clusters.[57] The calculations performed with our code showed that contrary to DFT and DFT+U, DFT+DMFT is able to reproduce important oscillations in magnetization for several regions of cluster sizes. Overall, the

DFT+DMFT results for the magnetic moments were found to be in much better agreement with experiment [36,58] as compared to other two approaches. One of the reasons for this is strong modification of the electronic spectrum after inclusion of the dynamical effects, in particular presence of new peaks in the DOS.

We also extended the nanoDFT+DMFT approach to another type of nanosystem - hematite Fe_2O_3 thin film with (001) surface. Bulk Fe_2O_3 is a narrow band-gap insulator (gap ~$2eV$). The system is anti-ferromagnetic below temperature 995 K. This oxide is considered as an efficient support for catalytic applications, corrosion, lubrication [59,60] and magnetic properties of materials, catalysis and geochemical process.[61,62] In general the thin-film structures, being finite in one and extended in two directions, combine properties of both finite and extended systems. The electronic and magnetic states on the surface is another interesting question in this case. In particular, it is very important to understand how dynamical effects modify the surface properties of this antiferromagnet. The structure of the surface of the Fe_2O_3 surface were studied both experimentally [63-65] and theoretically [64,66-68]. Most of this studies result in the conclusion that the lowest surface of the system has (001) structure with Fe-atom termination. In particular, the DFT+U calculations by Kiejna *et al*.[66] show that at low oxygen pressure the Fe-terminated structure (with Fe-O_3-Fe-ordering) is more stable than the other structures. In the case of the bulk system, spin DFT strongly underestimated values for the bandgap and the magnetic moments.[68] On the other hand, the DFT+U calculations improve the result for the magnetization, but fail to describe the metal-insulator transition (MIT)[69-71] The LDA+DMFT is able to reproduce the MIT in bulk Fe_2O_3,[72] [73] which suggest this approach to be also appropriate for films and nanoparticles. Our DFT+DMFT results show that dynamical effects lead to several interesting properties of the system, including surface states and nontrivial magnetism.

Finally, we performed a theoretical investigation of the Magneto-Crystalline Anisotropy (MCA) of L1_0 FePt bulk system and nanoparticles that consist of alternating layers of Fe and Pt atoms, by using the direct and torque DFT approaches. L1_0 thin films and nanoparticles are promising candidates for ultra-high density magnetic storage media due to their high corrosion resistance and excellent intrinsic magnetic properties.[10] Since FePt alloys shows large perpendicular MCA(on the order of 1 meV/atom[74]) as compared to various ferromagnetic metals and it can suppress superparamagnetism in nanoscale particle[75], it is a good candidate for anotechnological applications mentioned above. It has other advantages as compared to other rare earth transition metal compounds with high MCA, such as $Nd_2Fe_{14}B$ and $SmCo_5$ [76], being much less ductile and chemically inert.[9] In this work we perform a theoretical investigation of MCA of L1_0 FePt clusters of size 20 to 484 atoms. The clusters studied have 4(5), 3(4), 2(3) and 1(2) layers of $Fe(Pt)$ atoms and vice versa. Our results obtained with both direct and torque methods show that in this type of layered magnetic system the MCA is caused mainly by the large SOC of the 5d-electrons in the Pt atoms. On the other hand the role of the 3d-electrons in the Fe atoms is mainly in the exchange splitting of the Pt sub-lattice (see also Refs. [77-79]). We demonstrated that in the case of systems with large central layer of Pt atoms one can expect rather large (5meV/atom) anisotropy. The advantage of particles with such “encapsulated” anisotropy is that one does not need to cover them in order to protect the magnetic properties. We also performed detailed studies of the electronic structures of different atoms in the clusters in order to quantify a complex contribution of both 3d- and 5d-electronic states from both types of atoms to high MCA of the system. These results confirm one more time that one can expect very rich physics by tuning the chemical composition, size and geometry of the system.

In the next Chapter, we discuss the main *ab initio* approaches to study the electronic and magnetic properties of materials, including their successes and limitations.

CHAPTER 2 AB-INITIO APPROACHES TO STUDY THE ELECTRONIC AND MAGNETIC PROPERTIES OF MATERIALS

2.1 Density Functional Theory (DFT)

To understand different properties of materials one needs to know their electronic structure. DFT approach has been used for a long time for this purpose.

To derive the basic DFT equations, let us begin with the Schrodinger's equation for system of many electrons and nuclei:

$$\hat{H}\Psi(\mathrm{r}) = E\Psi(\mathrm{r}), \tag{2.1}$$

where $\hat{H}$ is the Hamiltonian operator:

$$\hat{H} = \hat{T}_e + \hat{T}_N + \hat{V}_{e-e} + \hat{V}_{N-N} + \hat{V}_{e-N}. \tag{2.2}$$

In Eq. (2.2), $\hat{T}_e$ and $\hat{T}_N$ are is the kinetic energy operators of electrons and ions, $\hat{V}_{e-e}$ is the electron-electron interaction operator, $\hat{V}_{N-N}$ is the corresponding nucleus-nucleus repulsion interaction term, and $\hat{V}_{e-N}$ is the electrostatic electron-nucleus attraction operator. In terms of the electron and nucleus coordinates these parts of the Hamiltonian can be written as:

$$\hat{T}_e = -\frac{1}{2}\sum_i \nabla_i^2,\ \hat{V}_{e-N} = \sum_i[\sum_I V(R_I - r_i)],\text{ and } \hat{V}_{e-e} = \sum_i \sum_{j>i} \frac{1}{r_i - r_j}, \tag{2.3}$$

and similar for the remaining two terms.

In Eq. (2.1), Ψ is the wave function and E is the eigen-energy of the system. In the case of a system with N-nuclei, and n-electrons, the wave function Ψ is a function of both electronic and nuclei coordinate:

$$\Psi = \Psi(r_1, r_2, \dots \dots \dots \dots r_n;\ R_1, R_2, \dots \dots \dots . R_N),$$

i.e. it depends on 3n+3N variables, which makes obtaining the solution very complicated. Thus in order to describe the system properties one needs to make some approximations.

2.1.1 The Born-Oppenheimer approximation

Due to smaller mass, electrons move much faster than the nuclei. Thus, electrons rapidly adjust themselves to the change in nucleus coordinates and one can decouple the electronic and nucleus degrees of freedom in solving Eq. (2.1):

$$\Psi(r_1, r_2, \dots \dots \dots \dots r_n;\ R_1, R_2, \dots \dots \dots . R_N) = \sum_\nu \Lambda_\nu(R)\, \Phi_{\nu,}(r_1, r_2, \dots \dots \dots \dots r_n) \quad (2.4)$$

where, Φ is the wave function of electrons for a fixed set of nucleus coordinates R. In this case, the Schrodinger equation for the electronic part of the system can be written as:

$$H^e \Phi(r_1, r_2, \dots \dots \dots \dots r_n) = E_\nu^e\, \Phi(r_1, r_2, \dots \dots \dots \dots r_n) \quad (2.5)$$

where

$$H^e = \hat{T}_e + \hat{T}_N + \hat{V}_{e-e} + \hat{V}_{e-N} \quad (2.6)$$

and

$$\hat{V}_{N-N} = \frac{1}{2}\sum_{I\neq J}\frac{Z_I Z_J}{R_{IJ}} \tag{2.7}$$

(Z_I is the nucleus (ion) charge).

After one obtains the solution of Eq. (2.6), one can calculate new positions of the ions by finding the minimum for energy of the system:

$$E^{BO} = \frac{1}{2}\sum_{I\neq J}\frac{Z_I Z_J}{R_{IJ}} + E_e(R) \tag{2.8}$$

The procedure is repeated until the converged solution for the electronic and ionic system is obtained. This algorithm forms the basis of the Born-Oppenheimer approximation (BOA). Despite the great simplification of the BOA, one still needs to take care of a huge number of electronic degrees of freedom in the Schrödinger equation, i.e. one need to properly take into account many-electron effects.

2.1.2 Hartree and Hartree-Fock approximation

In the simplest approximation, proposed by Hartree [80], it is assumed that the electrons don't interact with each other, so the many-electron wave function can be approximated by a product of single-electron orbitals:

$$\psi(\vec{r}_1, \vec{r}_2, \dots\dots\dots\dots \vec{r}_n) = \varphi_1(\vec{r}_1)\varphi_2(\vec{r}_2)\dots\dots\dots\varphi_n(\vec{r}_n). \tag{2.9}$$

In this case, Eq. (2.6) reduces to the following equation:

$$\left[-\frac{1}{2}\nabla_i^2 + \sum_I V(\vec{R}_I - \vec{r}_i) + \sum_{j\neq i}\int \left|\varphi_j(\vec{r}_j)\right|^2 \frac{1}{|\vec{r}_j - \vec{r}_i|} d\vec{r}_j\right]\varphi_i(\vec{r}_i) = \varepsilon\varphi_i(\vec{r}_i), \tag{2.10}$$

which can be rather easily solved numerically.

The third term in the square brackets in Equation (2.10) is an electrostatic potential experienced by the electron in the i^{th} state due to the other electrons. Thus, the problem reduces to one-electron equations, which can be solved self-consistently, for example by using an iterative procedure.

In the Hartree approximation, Equation (2.10), the electrons are interacting with each other only via the effective field; direct interactions between electrons are missing. Also, due to fermionic nature of electrons, their wave function must satisfy certain properties, missing in the Hartree approximation. Namely, the fermion wave function must be anti-symmetric with respect to interchanging each-pair of electrons:

$$\psi\left(\vec{r}_1, \vec{r}_2, \dots, \dots, \vec{r}_j, \dots, \vec{r}_k, \dots, \vec{r}_n\right) = -\psi\left(\vec{r}_1, \vec{r}_2, \dots, \dots, \vec{r}_k, \dots, \vec{r}_j, \dots, \vec{r}_n\right). \tag{2.11}$$

The property can be satisfied if one writes the electron wave function in the form of Slater determinant:

$$\psi(\overrightarrow{r_1}, \overrightarrow{r_2}, \dots., \overrightarrow{r_n}) = \frac{1}{\sqrt{n!}} \left\| \begin{matrix} \varphi_\alpha(\overrightarrow{r_1})\varphi_\beta(\overrightarrow{r_1}) \dots . \varphi_\upsilon(\overrightarrow{r_1}) \\ \varphi_\alpha(\overrightarrow{r_2})\varphi_\beta(\overrightarrow{r_2}) \dots . \varphi_\upsilon(\overrightarrow{r_2}) \\ \dots \dots \dots \dots \dots \dots \dots \dots \dots \dots .. \\ \dots \dots \dots \dots \dots \dots \dots \dots \dots \dots \dots \\ \varphi_\alpha(\overrightarrow{r_N})\varphi_\beta(\overrightarrow{r_N}) \dots . \varphi_\upsilon(\overrightarrow{r_N}) \end{matrix} \right\|. \tag{2.12}$$

Indeed, changing two electrons is equivalent to change of two columns in the Slater matrix, which correspond to change of the sign of the determinant. Also, such a wave function satisfies the Pauli exclusion principle, according to which one cannot have two electrons in the same state: determinant of the matrix with two or more equal columns is zero. This approximation is called the Hartree-Fock (HF) approximation. In the HF approximation the one-electron equation is:

$$\left[-\frac{1}{2}\nabla_i^2+\sum_I V\left(\vec{R}_I-r_i\right)\right]\varphi_\lambda(\vec{r}_i)+\left[\sum_\mu\int\varphi_\mu^*\left(\vec{r}_j\right)\frac{1}{|\vec{r}_j-\vec{r}_i|}\varphi_\mu\left(\vec{r}_j\right)d\,\vec{r}_j\right]\varphi_\lambda(\vec{r}_i)-$$

$$\left[\sum_\mu\int\varphi_\mu^*\left(\vec{r}_j\right)\frac{1}{|\vec{r}_j-\vec{r}_i|}\varphi_\lambda\left(\vec{r}_j\right)d\,\vec{r}_j\right]\varphi_\mu(\vec{r}_i)=\varepsilon\varphi_\lambda(\vec{r}_i) \qquad (2.13)$$

The last term on the left hand side of the equation describes the exchange interaction effects. As according to Pauli exclusion principle same-spin electrons cannot occupy the same state, it leads to a constraint in the electron motion, or an effective electron-electron interaction. In most cases, the HF approximation is much more accurate than the Hartree approximation. Exchange interaction deals with same-spin electrons, forbidding them to be in the same state (site, momentum and so on). However, different spin electrons can occupy the same state, which in particular is the case of two electrons occupying the same orbital, which in the case of localized orbitals may lead to large increase of their (Coulomb interaction) energy. The part of the electron energy beyond the HF approximation is called correlation energy. While in typical metallic and semiconductor systems the latter is rather small, in strongly correlated materials it can be very large, and one needs to make further approximations to include this part of the interaction in the effective Hamiltonian. In any event, the solution of the HF equation is rather expensive, because of their many-particle character. Therefore, it would be desirable to reduce the many-electron problem to a single-electron one.

2.1.3 LDA Approximation

Such an effective theory, called DFT, was constructed by Kohn, Hohenberg and Sham[81]. In this theory, all effects of electron-electron interaction are described by an effective potential that depends on the local electron charge density. Solution of the corresponding one-electron equation with the interaction term described by this potential has made possible the description of a large number of ground-state properties of many materials in a rather accurate way. Let us summarize here the main ideas that led to the development of DFT.

One can begin with writing the equation for the total energy of the system:

$$E = \int_{-\infty}^{\infty} \Psi^*(r_1, r_2, \dots, r_n) \widehat{H} \Psi(r_1, r_2, \dots, r_n) dr_1 dr_2 \dots dr_n. \tag{2.14}$$

The last equation suggests that the energy is functional of the many-electron wave function. Since kinetic and potential parts of the electron energies are also defined by this wave function, one can say that the wave function determines all physical properties of the multi-electron system. Thus, for given external (ion) potential and number of electrons in the system, one can obtain in principle the many-electron wave function, which determines the ground-state properties of the system. Thus, one can come to the idea that knowledge of the electron density in the system is sufficient to complete the description of its properties. In particular, all electron-electron interaction effects can be incorporated in an effective density-dependent exchange-correlation (XC) potential. This potential together with kinetic energy operator and the ion potential can be used in the effective one-electron equation, and the solution of this equation can be used to describe the ground-state properties of the system. In 1964 Honeberg and Kohn showed how that this external potential can be obtained from the local electron density by formulating two theorems.[81] In the first theorem, they stated that “The external potential $v(r)$ is determined, within a trivial additive constant, by the electron density $n(r)$ ”. Namely, the total ground state energy of the system can be written in terms of the density only,

$$E[n(r)] = T[n] + V_{ext}[n] + V_{e-e}[n] = F_{HK}[n] + V_{ext}[n], \tag{2.15}$$

where $F_{HK}[n]$ is the Hohenberg-Kohn functional. The second Hohenberg Kohn theorem states that ”For any trial electron density $\tilde{n}(r)$ such that $\int \tilde{n}(r)dr = N$ *(total number of electrons)*, gives energy always higher than the ground state energy of the system,” i. e. $E_0[n] \leq E_{v_{ext}}[\tilde{n}]$. The part of the potential in equation (2.15) can now be written as

$$V_{ext}[n] = \int n(r)v_{ext}(r)dr \tag{2.16}$$

and

$$V_{e-e}[n] = \int \frac{n(r)n(r')}{|\vec{r}-\vec{r}'|}drdr' + \tilde{E}_{xc}[n] \tag{2.17}$$

The first integral term in equation (2.17) is the classical electrostatic (Hartree) interaction, and $\widetilde{E}_{xc}[n]$ is the XC energy of the system. Comparing Eqs. (2.16) and (2.17), one can come to the conclusion that the effective potential for the one-electron problem has the following form:

$$v_{eff}(r) = v_{ext}(r) + v_H(r) + \frac{\delta \tilde{E}_{xc}}{\delta n(r)}. \qquad (2.18)$$

Next, since the kinetic energies of the non-interacting T_s and interacting T systems electron are not the same, one can include the correction due to this difference into the expression for the XC energy of the interacting system (see Eq. (2.15)): $E_{xc}[n] = \tilde{E}_{xc}[n] + (T[n] - T_s[n])$. Mapping the many-body and single-electron problems one can finally arrive at the following effective one-electron equation:

$$\left[-\frac{1}{2}\nabla^2 + V_{eff}(r)\right]\varphi_i = \varepsilon_i \varphi_i, \qquad (2.19)$$

where the effective potential depends self-consistently on the charge density:

$$n(r) = \sum_i |\varphi_i(r)|^2. \qquad (2.20)$$

Equation (2.19) and (2.20) are the key of DFT, and are known as Kohn-Sham equations[82]. The solution of these equations allows one to obtain a physical quantity – electron charge density, which defines the many-electron wave function and ground state properties of the system. It must be stressed that the physically meaningful quantity is only the charge density. The single-electron Kohn-Sham orbitals can be interpreted as electron wave functions only to a very limited extent, though one can use them for the Slater determinant to construct an approximate many-electron wave function. In order to use these equations one needs to know the expressions for the exchange and correlation parts of the XC potential.

The exchange part of the potential can be obtained from the HF exchange part of the energy in Eq. (2.13), by using the free-electron wave functions ($\varphi_k(r) = \frac{1}{\sqrt{V}} e^{ikr}$), and performing the momentum integration (momentum representation) up to the Fermi value.

Since the Fermi momentum is uniquely connected with the electron density, one can obtain the following expression for the exchange part of the energy:

$$\varepsilon_X^{hom} = -\left(\frac{81}{64}\right)^{1/3} n^{1/3}(r). \tag{2.21}$$

The correlation part of the interaction is very difficult to calculate exactly, even for the homogeneous electron gas. The only accurate results available so far are the cases of very high and low electron densities. For intermediate densities one needs to make approximations. One of the approximations for the correlation part of the energy proposed by Perdew & Zunger[83] (still in the homogeneous gas approximation) is:

$$\varepsilon_C^{hom} = \begin{cases} -0.1423\left(1 + 1.0529\sqrt{r_s} + 0.3334 r_s\right)^{-1}; r_s \geq 1 \\ -0.0480 + 0.0311 ln r_s + 0.002 r_s ln r_s;\ r_s < 1 \end{cases} \tag{2.22}$$

where $r_s = \left(\frac{4\pi n(r)}{3}\right)^{-1/3}$.

In general the above expressions for the energy form the Local Density Approximation (LDA), in which all exchange and correlation effects in the system are described by the local charge density:

$$E_{XC}[n(r)] = \int \varepsilon_{xc}^{hom}[n(r)]n(r)\,dr. \qquad (2.23)$$

This approximation, being in many cases more accurate than the HF one[84], give often results in a good agreement with experiment. For example the results for the bulk crystal lattice parameters are often differ only by 1~2% from the experimental data. On the other hand, the LDA XC functional being a smooth function of density fails to describe systems with charge distributions that significantly deviate from the homogeneous one. In this case naturally, one may try to include charge gradient corrections into the functional.

2.1.4 Generalized Gradient Approximation (GGA)

The corresponding approach is called GGA. In this approximation, the expression for the XC energy can be written as:

$$E_{XC}[n] = \int n(r)\varepsilon_{XC}^{hom}[n(r)]F_{XC}[n(r), \nabla n(r), \nabla^2 n(r) \dots \dots \dots]dr, \qquad (2.24)$$

where F_{XC} is the XC factor that depends on the charge density and its derivatives. For example in the fourth-order approximation by Gross and Dreizler[85] the exchange part of this function reads as:

$$F_X(p, q) = 1 + \frac{10}{81}p + \frac{146}{2025}q^2 - \frac{73}{405}qp + \mathcal{O}(\nabla n^6), \qquad (2.25)$$

where $p = \frac{|\nabla n|^2}{4(3\pi^2)^{2/3}n^{8/3}}$ is the square of the reduced density gradient, and

$q = \frac{\nabla^2 n}{4(3\pi^2)^{2/3}n^{5/3}}$ is the reduced Laplacian of the density.

In the case of slowly-varying densities, the second-order gradient expansion of the XC energy has the following general form:

$$E_{XC}[n] = \int A_{XC}[n]n(r)^{4/3}dr + C_{XC}[n]\,|\nabla n(r)|^2/n(r)^{4/3}\,dr \qquad (2.26)$$

The last expression has to satisfy some exact conditions, such as normalization, negativity of the exchange hole density and the cancellation of the self-interaction of the hole. It was shown by Perdew in 1985 [86] that imposing the above conditions on the form of the XC energy leads to a significant improvement of the results. Following this work, a number of different modifications of the expression for the XC potential were proposed. PBE [87] and PW91[88] are among the most successful GGA approximations, which in many cases significantly improve the LDA results.

2.1.5 Spin Density Functional Theory

To study a magnetic system with different densities of the spin-up and spin-down electrons, one needs to formulate a spin DFT with the XC that depends on both spin densities, and which is often referred as Local Spin-Density Approximation (LSDA). The total electron charge density in the systems in this case is the sum of spin up and spin down densities: $n(r) = n_{\uparrow}(r) + n_{\downarrow}(r)$, and one needs to solve a system of Kohn-Sham equations for each spin component:

$$\left[-\frac{1}{2}\nabla^2 + V_{eff}{}^{\sigma}(r)\right]\varphi_i{}^{\sigma}(r) = \varepsilon_i{}^{\sigma}\varphi_i{}^{\sigma}(r), \qquad (2.27)$$

where the index σ represents spin ($\uparrow\ or\ \downarrow$) and

$$V_{eff}{}^{\sigma}(r) = V_{ext}(r) + V_H(r) + \frac{\delta \tilde{E}_{xc}[n^{\uparrow}, n^{\downarrow}]}{\delta n(r)}. \tag{2.28}$$

Since the XC functional depends on spin-up and spin-down densities separately, it is equivalent to dependence on two linear combinations of these functions: the total charge density $n(r) = n_{\uparrow}(r) + n_{\downarrow}(r)$ and magnetization

$$m(r) = \mu_B \left(n^{\uparrow}(r) - n^{\downarrow}(r)\right) \tag{2.29}$$

Equation for exchange and correlation parts of the XC energy in the spin DFT are generally chosen in the form of non-spin polarized functional with substitution of total density by the spin density: $n(r) \rightarrow n_{\sigma}(r)$:

$$E_X^{\sigma-GGA} = \frac{1}{2}\sum_{\sigma=1}^{2} \int F_X(2n_{\sigma}, |2\nabla n_{\sigma}|) dr, \tag{2.30}$$

and

$$E_C^{\sigma-GGA} = \int F_c(n, \xi, |\nabla n|) dr. \tag{2.31}$$

2.1.6 Limitation of DFT for Strongly Correlated Systems

DFT is a successful approximation for the study of ground state electronic structures, but for many materials with narrow bands the homogeneous electron gas expression for XC energy is not sufficient, and often leads to wrong results. For example, the Mott insulator phase in many transition metal oxides[31] with partially filled d-orbitals, for example NiO [89], cannot be explained by standard DFT. DFT often predicts these materials to be metallic.[90] The reason for the failure is lack of proper expression for the correlation part of the XC potential for systems with strong local Coulomb repulsion.[31,47,91,92]

Another reason for failure of the L(S)DA potentials and their extensions in the strongly correlated regimes is strong self-interaction energy. Indeed each electron experiences an artificial potential created by itself and described by charge- (spin-) dependent XC potential. Since this potential strongly depends on the charge- (spin-) density, the effect will be significant in the case of strongly localized orbitals that create such large 'self-interaction' potentials. One of the results of this "residual self-interaction" is systematical underestimation of the energy gap in insulators and semiconductors[93].

Another effect of this self-interaction is the inability of *LSDA* to produce correct charge orderings. Inhomogeneous charge distribution corresponding to a charge ordered state is unstable in *LSDA, due to increased self-interaction on sites with large charge densities.* For example, for magnetite Fe_3O_4, *LSDA* calculations give metallic state without charge ordering in contrast to the experimentally observed charge- ordered insulating ground state[94,95].

2.2 DFT+U method

In strongly correlated materials electrons spend a significant amount of time in regions where the presence of other particles makes them experience strong Coulomb repulsion, thus making their motion correlated. The local correlation effects are especially important in the case of narrow-band materials, in which the kinetic energy of electrons is of the order of or smaller than the local repulsion energy U. The most straightforward way to include these correlation effects in DFT is through the DFT+U approximation. In this approach, one uses DFT results for the bandstructure as input for the “non-interacting” electron part of the phenomenological Hubbard lattice Hamiltonian that takes into account effects of local electron-electron repulsions.[19] The solution of the lattice problem results in corrected expression for the energy of the system:

$$E_{LDA+U}[n(r)] = E_{LDA}[n(r)] + E_{Hub}[n^{I\sigma}_{mm'}] - E_{LDAc}[n^{I\sigma}], \qquad (2.32)$$

where $E_{Hub}[n^{I\sigma}_{mm'}]$ is the Hubbard (electron interaction) part of the energy, and $E_{LDAc}[n^{I\sigma}]$ is the LDA part of the correlation energy part which is subtracted in order to avoid double counting of the correlation effects already (rather poorly) incorporated in the $E_{LDA}[n(r)]$; $n^{I\sigma}_{m\acute{m}} = c^{\sigma+}_{m} c^{\sigma}_{m'}$ are the two-electron operators on the Hubbard site I with the total local spin densities $n^{I\sigma} = \sum_m n^{I\sigma}_{mm}$. Eq. (2.32) can be easily transformed to:

$$E_{LDA+U} = E_{LDA} + \sum_I \left[\frac{U}{2}\sum_{m,\sigma\neq\acute{m},\acute{\sigma}} n^{I\sigma}_{m} n^{I\acute{\sigma}}_{\acute{m}} - \frac{U}{2} n^I(n^I - 1)\right]. \qquad (2.33)$$

Minimization of the functional (2.33) leads to new atomic charge distribution and to new orbital energies:

$$\epsilon^I_{m\sigma} = \frac{\partial E_{LDA+U}}{\partial n^{I\sigma}_m} = \epsilon^{0I}_{m\sigma} + U\left(\frac{1}{2} - n^{I\sigma}_m\right), \qquad (2.34)$$

where ϵ^0 is the orbital energy obtained from LDA calculations. From the expression on the right hand side of Equation (2.34) one can immediately see that in the case of non-zero U, there is a gap ~U between occupied and unoccupied states in the system, which is the essence of the LDA+U approximation.

In the case of magnetic systems, one also needs to include the exchange coupling J in Equation (2.33). Another limitation for the values of U of the approximation above is that U is not rotationally invariant of the magnetic quantum number m. To remove these deficiencies, Anisimov *et al*.[96,97] proposed an effective Hamiltonian:

$$E_{Hub}\left[\{n^{I}_{m\acute{m}}\}\right] = \frac{1}{2}\sum_{\{m\},\sigma,I}\{\langle m,m''|V_{ee}|m',m'''\rangle n^{I\sigma}_{mm'}n^{I-\sigma}_{m''m'''} + (\langle m,m''|V_{ee}|m',m'''\rangle - \langle m,m''|V_{ee}|m''',m'\rangle)n^{I\sigma}_{mm'}n^{I\sigma}_{m''m'''}\}, \tag{2.35}$$

$$E_{LDAc}[\{n^{I}\}] = \sum_{I}\left\{\frac{U}{2}n^{I}(n^{I}-1) - \frac{J}{2}\left[n^{I\uparrow}\left(n^{I\uparrow}-1\right) + n^{I\downarrow}\left(n^{I\downarrow}-1\right)\right]\right\} \tag{2.36}$$

where J is exchange energy parameter and V_{ee} is the Coulomb interaction between two d electrons occupying on the same site. The corresponding matrix elements can be expanded in spherical basis:

$$\langle m,m''|V_{ee}|m',m'''\rangle = \sum_{k} a_{k}(m,m',m'',m''')F^{k}, \tag{2.37}$$

where $0 \leq k \leq 2l$, l being the angular momentum number of electron (*l*=2 in the d-orbital case), and

$$a_{k}(m,m',m'',m''') = \frac{4\pi}{2k+1}\sum_{q=-k}^{k}\langle lm|Y_{kq}|lm'\rangle\langle lm''|Y^{*}_{kq}|lm'''\rangle \tag{2.38}$$

are the Clebsch-Gordon coefficients. Parameters F^{k} describe the strength of the interaction between electrons. In particular,

$$U = \frac{1}{(2l+1)^{2}}\sum_{m,m'}\langle m,m'|V_{ee}|m,m'\rangle = F^{0} \tag{2.39}$$

and

$$J = \frac{1}{2l(2l+1)} \sum_{m \neq m', m'} \langle m, m' | V_{ee} | m', m \rangle = \frac{F^2 + F^4}{14}. \qquad (2.40)$$

The values of U and J can be determined empirically, by fitting it to experimental data, or by LDA calculation.[98] For example, Cococcioni and Gironcoli[90] computed U by using constrained-density-functional theory as

$$U = \frac{\partial^2 E[\{q^I\}]}{\partial (q^I)^2} - \frac{\partial^2 E^{KS}[\{q^I\}]}{\partial (q^I)^2}, \qquad (2.41)$$

where $E[\{q^I\}]$ is the energy functional for the localized orbital level that depends on the orbital charge q^I in the case of the Hubbard model, and $E^{KS}[\{q^I\}]$ is the same quantity in the case of the Kohn-Sham system. Once the values of U and J are obtained, parameters F^0, F^2 and F^4 can be calculated by using equations (2.39) and (2.40). Another equation needed to calculate this coefficient is relation between F^2 and F^4, which in the case of d-electrons is $\frac{F^4}{F^2} = 0.625$.

In many cases, DFT+U lead to a dramatic improvement of the DFT solution, especially in reproducing their energy gaps. On the other hand, it also fails in many cases. For example, the fact that NiO is an insulator both above and below the Neel temperature cannot be explained by DFT+U. The multiplicity of 4f- and 5f-orbitals in actinide series elements also cannot be reproduced by this approach. One of the reasons for this is the static (HF) nature of the DFT+U approximation, which neglects fluctuations, including dynamical effects. Before proceeding with the summary of the main features of DMFT, which takes these effects into account, we briefly describe another alternative to the

DFT+U approach to include the correlation effects into the analysis of the properties of the systems – the GW approximation.

2.3 GW approximation

In this approach the effects of long-range Coulomb interaction between electrons are included in a perturbative manner. GW, originally applied to calculate the excited state properties of bulk materials gives in many cases superior results for the band structure than DFT.[99] In this approach one calculates the one-electron Green's function (propagator) $G(r,r';t,t')$, [100] which corresponds to the probability of having an electron at site r at a time t assuming that was one at r' at an initial time t'. The total energy, electronic density, density of states, electronic excitations and other properties of the material can be obtained from the solution for this Green's function.[98] The presence of other electrons significantly modifies the spectrum of properties of the electron under consideration. In particular they lead to a screening of the electron-electron interaction and shift the electron energy levels, described by the electron self-energy function Σ . The Green's function and the self-energy are related via a Schrödinger-like equation, which has the following form in the energy domain:

$$[\epsilon - h(r) - V(r)]G(r,r';\epsilon) - \int \Sigma(r,r'';\epsilon)\, G(r'',r';\epsilon)dr'' = \delta(r-r'). \tag{2.42}$$

In eq. (2.42) $h(r) = -\left(\hbar^2/_{2m}\right)\nabla^2 - \sum_{\mathrm{n}} \mathrm{Z_n v(r, R_n)}$ is the "free"-electron part of the Hamiltonian ($\mathrm{Z_n}$ and $\mathrm{R_n}$ is the charge and positions of the nth nucleus),

$V(r) = \int v(r,r')n(r')\,dr'$ with $v(r,r') = {e^2}/{|r - r'|}$ is the Hartree interaction part that depends on the charge density $n(r) = \langle \psi^{\dagger}(r)\psi(r)\rangle = -i\hbar G(r,t;r,t+\Delta)$ ($\Delta \rightarrow 0^{+}$).

The Green's function can be derived from an exact Green's function of a reference system via Dyson's equation

$$G(r,r';\epsilon) = G_0(r,r';\epsilon) + \iint G_0(r,r_1;\epsilon)\Delta\Sigma\,(r_1,r_2;\epsilon)G(r_2,r';\epsilon)dr_1 dr_2 \tag{2.43}$$

where $\Delta\Sigma(r_1,r_2;\epsilon) = \Sigma(r_1,r_2;\epsilon) - v_2(r_1,r_2)$ with $v_2(r_1,r_2)$ is the interaction potential of the reference system, $v_2 = 0$ if the reference system is non-interacting. The expression for the non-interacting Green's function

$$G_0(r,r';\epsilon) = \sum_n \frac{\varphi_n(r)\varphi_n^*(r)}{\epsilon - \varepsilon_n}, \tag{2.44}$$

where $\varphi_n(r)$ and ε_n are single particle wave-functions and eigen-energies, can be obtained from DFT calculations. In order to calculate the electron self-energy, a complex function that includes the static and dynamical interactions in the system, Hedin[101] suggested in 1965 the use of an approximation which became known latter as GW. In this approximation, one only includes the first-order term in the expansion of the self-energy of screened Coulomb interaction W:

$$\Sigma_{GW}(r,r';t) = iG(r,r';t)W(r,r';t), \tag{2.45}$$

or in energy domain:

$$\Sigma_{GW}(r,r';E) = i\int G(r,r';E+E')W(r,r';E)dE'. \tag{2.46}$$

One can derive the corresponding equation for $W(r,r';E)$ in terms of the one-loop polarization:

$$P(r,r';E) = -i\, G(r,r';E)G(r',r;E). \tag{2.47}$$

The equation for the screened interaction has the following form:

$$W(r,r';E) = v_2(r,r') + \iint W(r,r_1;E)P(r_1,r_2;E)v_2(r_2,r')dr_1\, dr_2, \tag{2.48}$$

where $v_2(r_1,r_2)$ is the interaction potential of the reference system (equal zero in the case of non-interacting reference system).The set of equations (2.45), (2.46), (2.47) and (2.48) known as Hedin's equations[101], can be solved iteratively.

Assuming the "non-interacting" system to be the Hartree one ($\Sigma = 0$), the lowest-order in W expansion of the equations above gives:

$$P^0(1,2) = -iG(1,2)G(2,1) \tag{2.49}$$

$$W(1,2) = v(1,2) + \int W(1,3)P^0(3,4)v(4,2)d(3,4) \tag{2.50}$$

$$\Sigma(1,2) = iG(1,2)W(1^+,2) \tag{2.51}$$

where P^0 is the non-interacting polarization function. These equations form the basis of the approach known as the GW approximation. Despite its successes, especially in describing the material bandstructure, [99,102] GW is still either unfeasible or incapable of describing many properties of correlated materials, including magnetism. It is for these reasons that the DMFT approximation is often used. Below we begin with a description of the main features of this better theory.

CHAPTER 3: DFT+DMFT APPROACH

3.1 Introduction

In recent years, DMFT has become a widely-used technique to study strongly correlated materials. As it was mentioned above, it succeeded the DFT+U approach,[19,97] which being a static mean field approximation neglected many important processes in systems, such as time-resolved local interactions (Fig. 6).

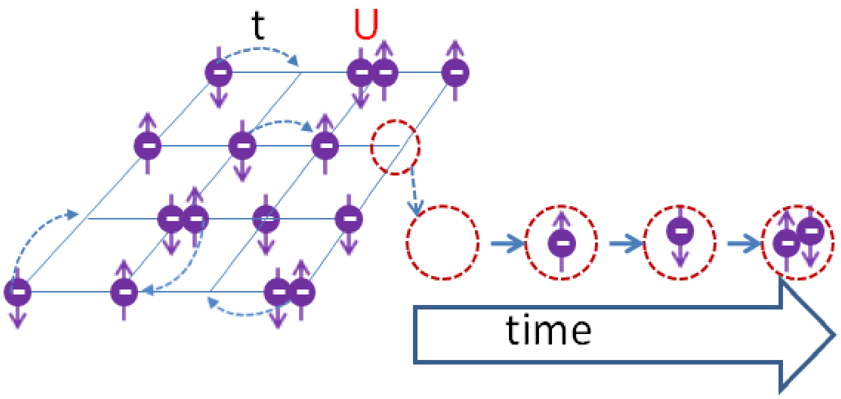

Figure 6: Schematics of electrons in a lattice. Over time a lattice sites can be unoccupied, occupied or doubly occupied by electrons. These dynamical processes which results in time-resolved electron-electron interactions are taken into account in DMFT.

In the DMFT approximation, the temporal fluctuation of electrons is taken into account through the frequency-dependence of the electron self-energy, while the spatial-dependence of self-energy is neglected. Thus the exact solution can be obtained only for infinite dimensional system or systems with infinite coordination number.[22] However, this approximation appears to be very good for many 2D and 3D materials.[23] DMFT was successfully extended to incorporate electron-phonon interaction[103], multilayered systems[104,105], non-equilibrium[106,107] phenomena, etc. Most importantly, the DMFT method was combined with DFT. [21],[20,108] In DFT+DMFT, the structure of the system and non-correlated band of electron subsystem are obtained from DFT calculations[21,109] and correlation effects are taken into account as the next step by solving the effective Hubbard model problem.

Dynamical effects are responsible for many unusual properties in many bulk Transition Metal (TM) systems. When correlations are not extremely large (kinetic energy and U are of the same order), as in the case of many bulk TMs, DFT+U can lead to wrong results. For example, it predict a non-existing magnetic phase in plutonium,[110] while DMFT calculations give the non-magnetic ordering in agreement with experiment.[111]

In general, one can identify three different regimes of correlation effects in which a particular theoretical approach is appropriate: weakly-correlated systems (DFT), strongly correlated systems (DFT+DMFT), and very strongly correlated systems (DFT+U), as shown in Fig. 7. The regime with intermediate values of the Coulomb repulsion is the most challenging and interesting, particularly for nanosystems as the competition between the kinetic and potential (Coulomb repulsion) energies may lead to a variety of exotic novel phenomena both in the ground and excited states. Since temporal fluctuations are expected to play a role here, DMFT seems to be the most promising.

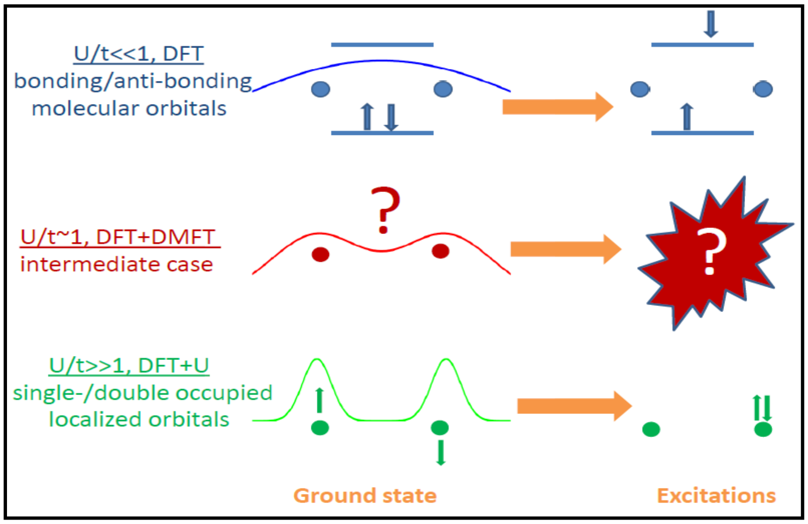

Figure: 7 A Schematics representation for three different electron correlation regimes and the methodology appropriate for their theoretical description: weakly correlated (top, DFT), strongly correlated (bottom, DFT+U), intermediate correlation in which Coulomb repulsion and the onsite hopping are at the same range in energy (DFT+DMFT). The smooth curves represent typical charge distributions for these cases.

3.2 Basics of DMFT

In the DMFT approximation, one solves an effective Hubbard model problem of strongly correlated electrons. The Hubbard model is a simple model of interacting electrons in a solid. It was introduced by Hubbard, Gutzwilller and Kanamori in 1963.[112-114] The model Hamiltonian can be written as:

$$H = -\sum_{i,j,\sigma,l,m} t_{il;jm} c_{i\sigma l}^{\dagger} c_{j\sigma m} + \sum_{i,j,\sigma,\sigma',m} U_{\sigma,\sigma'}^{lm} n_{i\sigma l} n_{j\sigma' m}, \qquad (3.1)$$

where $c_{i\sigma l}^{\dagger}$ is the creation operator of an electron at site i with spin σ; l are other quantum numbers (orbital momentum, band number etc), and $c_{j\sigma m}$ is the annihilation operator of an electron at site j. $n_{i\sigma l} = c_{i\sigma l}^{\dagger} c_{i\sigma l}$ is the number operator at site i, $t_{il;jm}$ is the electron hopping matrix elements, describing hopping of electrons from a site i (state l) to a site j (state m). The first term describes the kinetic processes in the system. $U_{\sigma,\sigma'}^{lm}$ is the local Coulomb repulsion matrix, that describes the Coulomb repulsion energies for electrons with different quantum numbers. The hopping parameters are usually obtained by fitting with the experimental band structure with typically only nearest-neighbor and next nearest-neighbor elements taken into account. The Coulomb repulsion parameters U can be obtained from DFT calculations self-consistently for each site and each orbital as discussed is chapter 2 or can be parameterized. At $\frac{U}{t} = 0$ the Hubbard model describes the system of Bloch electrons with the dispersion $\epsilon_k = \sum_{i,j} e^{ik(R_i - R_j)} t_{ij}$. Similar properties of the system will take place in the case of weakly-interacting electrons at U/t<<1. When $\frac{U}{t} \gg 1$ the Hubbard model describes the Mott insulator states, and can be reduced to a simplified Heisenberg spin model. For $\frac{U}{t} \sim 1$ no simplification can be made and one needs to solve the Hubbard model numerically with DMFT.

We now present the system of DMFT equations and describe how it can be solved self-consistently. More details can be found in Ref. [23]. The main idea of DMFT is in mapping the many-site problem on to a single-site one (since the self-energy is site-independent all sites are equivalent). The singled-out site is treated as an impurity in the bath of all other lattice electrons (Fig. 8).

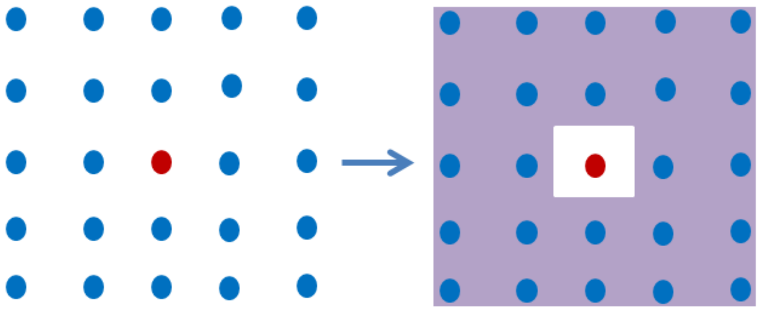

Figure 8: One site (the red) is singled out and all the other site is represented as bath by the shaded line. The red site is represented as an impurity on the lattice.

The hopping parameter for each site of the lattice is usually obtained by fitting with the experimental band structure, and only the nearest neighboring and next nearest neighboring hopping are consider for simplicity. Properties of the system described by the Hamiltonian in equation (3.1) can be studied by finding the time-ordered single-electron Green's function

$$G_{i\sigma l;j\sigma' m}(t,t') = -i\,\langle T c_{i\sigma l}(t) c^{\dagger}_{j\sigma' m}(t')\rangle, \tag{3.2}$$

where $T c_{i\sigma l}(t) c^{\dagger}_{j\sigma' m}(t') = \theta(t-t') c_{i\sigma l}(t) c^{\dagger}_{j\sigma' m}(t') - \theta(t'-t) c^{\dagger}_{j\sigma' m}(t') c_{i\sigma l}(t)$. This

Green's function is connected with the electron self-energy that defines the spectrum of interacting electrons, via the Dyson equation in frequency representation:

$$G_{i\sigma l;j\sigma' m}(\omega,\omega') = G^0{}_{i\sigma l;j\sigma' m}(\omega) + \sum_{i_1 i_2} G^0_{i\sigma l;i_1\sigma' m}(\omega)\Sigma_{i_1\sigma l;i_2\sigma' m}(\omega)G_{i_2\sigma l;j\sigma' m}(\omega) \qquad (3.3)$$

where $G^0{}_{i\sigma l;j\sigma' m}(\omega)$ is the Green's function of non-interacting electrons (at U=0). In the DMFT approximation the self-energy is local in space and site-independent, which is equivalent to $\Sigma_{\sigma l}(\mathrm{k},\omega) = \Sigma_{\sigma l}(\omega)$. Indeed, k-independent self-energy corresponds to the case when only local matrix elements are nonzero, and all other non-diagonal part vanishes in real space, for homogeneous case,

$$\Sigma_{i\sigma l;j\sigma' m}(\omega) = \delta_{i\sigma l;j\sigma' m}\Sigma(\omega). \qquad (3.4)$$

In the non-homogeneous case (atoms are nonequivalent), the self-energy bears the site index:

$$\Sigma_{i\sigma l;j\sigma' m}(\omega) = \delta_{i\sigma l;j\sigma' m}\Sigma_{i\sigma l}(\omega). \qquad (3.5)$$

In the reduced single-site problem, one is interested only in the local (one-site) Green's function (still corresponding to the many-body problem):

$$G_{\sigma l}(\omega) = \int \frac{d\mathrm{k}}{(2\pi)^d}\left(\frac{1}{\omega-\varepsilon(\mathrm{k})+\mu-\Sigma(\omega)}\right)_{\sigma l;\sigma l} \equiv G_{loc\ \sigma l}(\omega), \qquad (3.6)$$

where μ is the chemical potential of the system and $\varepsilon(\mathrm{k})$ is the band-energy matrix obtained usually from DFT or DFT+U calculation.

To find the expression for the effective bath field, we use the path integral approach. To begin, we write the partition function in terms of one the fermionic Grassmann variables ψ^*, ψ [23,115]:

$$Z = \int \prod_{i\sigma} d\psi^* d\psi e^{-A[\psi^*,\psi]} \tag{3.7}$$

where

$$A[\psi, \psi^*] = \int_0^\beta d\tau \big(\sum_{i,\sigma} \psi_{i\sigma}^* \partial\tau \psi_{i\sigma} - \sum_{i.j.\sigma} t_{i,j} \psi_{i\sigma}^* \psi_{j\sigma} - \mu \sum_{i,\sigma} \psi_{i\sigma}^* \psi_{i\sigma} + U \sum_i n_{i\uparrow} n_{i\downarrow} \big) \tag{3.8}$$

is the action functional of the Hubbard system. For the singe (impurity) site q, the action can be calculated as:

$$\frac{1}{Z_{eff}} e^{-A_q} = \frac{1}{Z} \int \prod_{i\neq q,\sigma} d\psi^* d\psi e^{-A[\psi^*,\psi]} . \tag{3.9}$$

The total partition function in equation (3.7) can now be rewritten in terms of the impurity action A^0 that comes from the rest of the system and the interaction part that connects the impurity with rest of the lattice ΔA:

$$Z = \prod_\sigma \int d\psi_{q\sigma}^\dagger d\psi_{q\sigma} e^{-A_q} \int \prod_{i\neq\sigma} d\psi_{i\sigma}^\dagger d\psi_{i\sigma} e^{-(A^0+\Delta A)}. \tag{3.10}$$

To find Z, one can expand the exponents in power series, using:

$$Z = \prod_\sigma \int d\psi_{q\sigma}^\dagger d\psi_{q\sigma} e^{-A_q[1-\langle\Delta A\rangle^0+\frac{1}{2!}\langle\Delta A^2\rangle^0- \ldots\ldots]}. \tag{3.11}$$

Only even power of ΔA terms contribute to Z. In particular, one can use:

$$\langle\Delta A^2\rangle^0 = \int_0^\beta \int_0^\beta d\tau_1 d\tau_2 \sum_{i,j\neq q,\sigma} t_{iq}\, t_{qj} \psi_{q\sigma}^\dagger(\tau_1) \langle T\psi_{i\sigma}(\tau_1) \psi_{i'\sigma}^\dagger(\tau_2)\rangle \psi_{q\sigma}(\tau_2)$$

$$= \int_0^\beta \int_0^\beta d\tau_1 d\tau_2 \sum_{i,j\neq q,\sigma} t_{iq}\, t_{qj} \psi_{q\sigma}^\dagger(\tau_1) G_{ij}^0(\tau_1 - \tau_2)\psi_{q\sigma}(\tau_2) \tag{3.12}$$

The higher-order terms can be written as a power of single particle Green's function, so from equation (3.9) one can write the effective action as

$$A_{eff} =$$

$$A_q + \sum_{n=1}^{\infty} \sum_{i_1 \dots i_n} \sum_{j_1 \dots j_n} \int d\tau_{i_1} \dots \dots d\tau_{j_n} t_{i_1 q} \dots \dots .\, t_{i_n q} t_{q j_1} \dots \dots .\, t_{q j_n} \times$$

$$\psi_{q\sigma}^\dagger(\tau_{i_1}) \dots \psi_{q\sigma}^\dagger(\tau_{i_n}) \psi_{q\sigma}(\tau_{j_1}) \dots \psi_{q\sigma}(\tau_{j_n}) \times G_{i_1 \dots} j_n(\tau_{i_1} \dots \tau_{j_n}). \tag{3.13}$$

By setting $t_{ij} = \frac{t_{ij}}{\sqrt{d}}$, to use the same scale for thee kinetic and potential energies, one can write the effective action in the DMFT approximation, at $d \to \infty$, as:

$$A_{eff}[\psi, \psi^*, \mathcal{G}^{-1}] = -\int_0^\beta d\tau \int_0^\beta d\tau' \sum_\sigma \psi_{0\sigma}^*(\tau) \mathcal{G}^{-1}(\tau - \tau') \psi_{0\sigma}(\tau') + U \int_0^\beta d\tau n_{0\uparrow}(\tau)\, n_{0\downarrow}(\tau) \tag{3.14}$$

where $\mathcal{G}^{-1}(\tau_1 - \tau_2) = -\left(\frac{\partial}{\partial\tau} - \mu\right) \delta_{\tau_1,\tau_2} - \sum_{ij} t_{iq}\, t_{qj} G_{ij}^0(\tau_1 - \tau_2)$ is the dynamical mean-field, which takes into account all the effects of the rest of the system with sites $\neq 0$ on the impurity site. The local Green's function can now be written as

$$G_{loc}(\omega) = \int d\psi d\psi^* \psi_{\sigma l} \psi_{\sigma' m}^* e^{-A_{eff}[\psi, \psi^*, \mathcal{G}^{-1}]}. \tag{3.15}$$

This problem is equivalent to the problem of the single site coupled to the bath described by the mean field $\mathcal{G}_{\sigma l; \sigma' m}(\omega)$. Since the impurity and many-particle problems are equivalent, one assumes that the local Green's functions (3.6) and (3.15) are equal to each other. This allows one to write the Dyson equation that connects the lattice local Green's function, electron-self energy and the bath field:

$$G^{-1}(\omega) = \mathcal{G}^{-1}(\omega) - \Sigma(\omega) \tag{3.16}$$

The set of DMFT equations (3.6), (3.15) and (3.16) can be to solved self-consistently.

Before describing a possible iterative algorithm, let us briefly discuss the physical meaning of the mapping of the many-body problem on the impurity one. This mapping corresponds to mapping the Hubbard model on the Anderson Impurity Model (AIM) with the Hamiltonian:

$$H_A = \sum_{\sigma}(\epsilon_0 - \mu)c_{0\sigma}^{\dagger}c_{0\sigma} + U\, n_{0\uparrow}n_{0\downarrow} + \sum_{\mathrm{k},\sigma} V_{\mathrm{k}}(c_{\mathrm{k}\sigma}^{\dagger}c_{0\sigma} + c_{0\sigma}^{\dagger}c_{\mathrm{k}\sigma}) + \sum_{\mathrm{k},\sigma} \epsilon_{\mathrm{k}}^{b}\, c_{\mathrm{k}\sigma}^{\dagger}c_{\mathrm{k}\sigma} \tag{3.17}$$

where ϵ_0 and $\epsilon_{\mathrm{k}}^{b}$ are the energy levels of the impurity (one level) and bath electrons (many levels), and V_{k} is the hybridization between the bath and impurity electrons. [23] In the AIM at U=0 one can find the impurity Green's function exactly:

$$G_{imp}(\omega) = \frac{1}{\omega - \epsilon_0 + \mu - \Delta\omega}, \tag{3.18}$$

where

$$\Delta\omega = \sum_{\mathrm{k},\sigma} \frac{|V_{\mathrm{k}}|^2}{\omega - \epsilon_{\mathrm{k}}^{b}}, \tag{3.19}$$

is the hybridization function which is equivalent to the effective bath field $\mathcal{G}^{-1}$ in action (3.14) (both functions represents the local impurity Green's function at U=0).

The steps of iterative solution of the DMFT equations (3.6), (3.15) and (3.16) can be as follows:

- Choose and initial self-energy $\Sigma(\omega)$;

- Calculate the local Green’s function from equation (3.6) with adjusted value of the chemical potential so that the total numbers of electrons in the system remain conserved;
- Calculate the dynamical mean-field $\mathcal{G}(\omega)$ from equation (3.16);
- Use the dynamical mean-field to solve the impurity problem (3.15) to find the new local Green’s function;
- Find the new self-energy from equation (3.16) by using the new Green’s function and the dynamical mean-field;
- Continue iteration until the self-energy is converged.

Once the Green’s function is found, one can calculate different physical quantities, such as the density of electrons for each orbital and spin:

$$n_{\sigma l} = -\int \frac{d\omega}{2\pi} \int \frac{d\mathrm{k}}{(2\pi)^d} ImG_{\sigma l;\sigma l}(\omega). \tag{3.20}$$

The most difficult part in the above is the impurity problem (3.15). There are several different types of approaches (solvers) available, for example, one based on the exact Quantum Monte Carlo (QMC). The Hirsh-Fye version of QMC solver[116] can be used with rather modest computational resources, but it works well only at high enough temperatures.[17] Another version of QMC algorithm is Projective QMC, in which the zero- temperature limit is considered analytically to get the exact ground state of the system.[117] The most promising QMC approach, however, is the Continuous-Time QMC (CT-QMC) which does not use discretization of time. It can work with expansion series of U[118], or perturbative hybridization of V[119], and allows one to avoid several problems related to other QMC methods, while at the same time being computationally faster. The Numerical Renormalization Group (NRG), Exact Diagonalization Method (ED) and Iterative Perturbation Theory (IPT) are some other approaches to solve the impurity problem beyond QMC. In our study, we used the Hirsch-Fye QMC approach (as implemented in the LISA code) for small clusters, and the IPT approximation (in our own code) for larger systems. The details of the IPT approximation will be given in Section 3.4.

3.3 Application of DMFT to nanosystems

It was suggested by Florens[46] that when the average coordination number in the system is large, DMFT should be a good approximation even for finite systems. In majority of nanostructures and large molecules the average coordination number is close to the bulk value (except, probably, chains), therefore one can expect DMFT to work well for transition metal nanoparticles as well. In finite systems, one needs to use a generalized nonhomogeneous DMFT approach, since different sites are non-equivalent. In this case, the electron self-energy can be approximated by local, but site-dependent function (equation (3.5)). The nonhomogeneous DMFT approach was proposed in Refs. [104,105]. Some of the sites might be equivalent, as in the case of the dimer, an equilateral triangle, etc. In general, though, one can have many non-equivalent sites which make the solution rather slow. Example of a system with several nonequivalent sites is shown in Fig. 9.

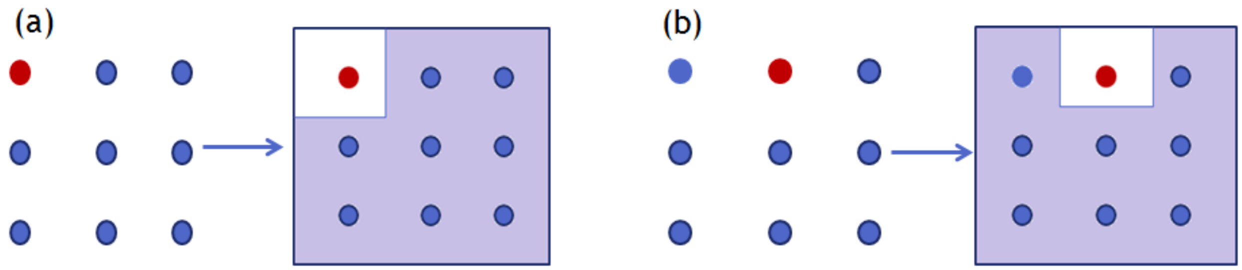

Figure 9: Mapping the many-body to impurity problem in a non-homogeneous case. Two non-equivalent impurity sites in the case of 9-atom structure. One needs to solve the impurity problem separately for each of them (central atom is another non-equivalent site).

One can justify the DMFT approximation in the nanocase following Florens' suggestion[46] as follows. The properties of a given site can be obtained from the solutions for the rest of sites. For simplicity, we consider here a core-shell type of nanoparticle in Fig. 10. Sites 0 and 1 form an impurity with respect to sites 2. One can solve the problem for sites 2 with missed sites 0 and 1 (cavity). Then one can calculate the effect of sites 2 (bath) on sites 1. Next, knowing the solution for sites 1 one can use it as the bath for site 0. Similarly, one can proceed in the case of larger particles.

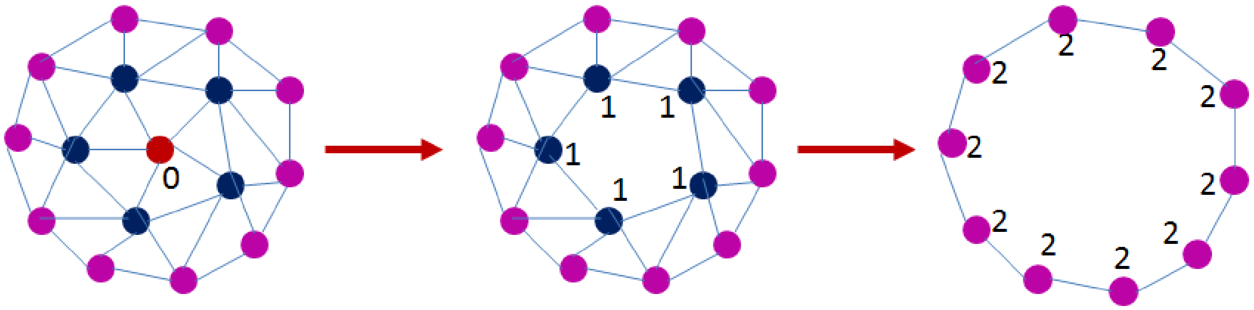

Figure 10: Different shells of atoms used for cavity solution of the DMFT problem.

To derive the DMFT equations for non-homogeneous case we followed Nolting and Potthoff [104,105]. In this case the electron Green's function has size $2 \times N \times M$ (2-spin, N-sites and M-orbital variables). Equation (3.4) now becomes:

$$G^{-1}_{i\sigma,l;i\sigma,l} = \begin{pmatrix} \omega + \mu - \Sigma_1(\omega) & t_{12} & t_{13} & \dots & \dots & t_{1N} \\ t_{21} & \omega + \mu - \Sigma_2(\omega) & t_{23} & \dots & \dots & t_{2N} \\ t_{31} & t_{32} & \omega + \mu - \Sigma_3(\omega) & \dots & \dots & t_{3N} \\ \dots\dots\dots\dots & \dots\dots\dots & \dots\dots\dots\dots & \dots\dots & & \dots \\ t_{N1} & t_{N2} & t_{N3} & \dots & \dots & \omega + \mu - \Sigma_N(\omega) \end{pmatrix} \tag{3.21}$$

where we have assumed that for a nonhomogeneous system the self-energy is local in space, but it is site-dependent $\Sigma_{i\sigma l;j\sigma' m}(\omega) = \delta_{\sigma;\sigma'}\delta_{i;j}\delta_{l;m}\Sigma_{i\sigma l}(\omega)$ .The matrix in equation (3.21) corresponds to the case of one orbital per site. In the case of multi-orbital system, the self-energy depends on orbital and spin indexes. The problem can be mapped on the impurity problem, similar to periodic systems, which gives in general $2 \times N \times M$ impurity problems with the dynamical mean-fields $\mathcal{G}_{i\sigma l;i\sigma l}(\omega)$. The other two equations (3.15) and (3.16) remain the same as in the homogeneous case:

$$G^{-1}_{i\sigma,l;i\sigma,l}(\omega) = \mathcal{G}^{-1}_{i\sigma,l;i\sigma,l}(\omega) - \Sigma_{i\sigma,l}(\omega) \tag{3.22}$$

and

$$G_{i\sigma,l;i\sigma,l}(\omega) = \int d\psi d\psi^* \psi_{i\sigma l}\psi^*_{i\sigma l} \exp(-\int_0^\beta d\tau \int_0^\beta d\tau' \sum_\sigma \psi^*_{i\sigma,l}(\tau)\mathcal{G}^{-1}_{i\sigma,l;i\sigma,l}(\tau-\tau')\,\psi_{i\sigma,l}(\tau') +$$

$$U_{i,l}\int_0^\beta d\tau n_{i\uparrow l}(\tau) n_{i\downarrow l}(\tau)). \tag{3.23}$$

Similar, to the periodic case, one can solve the set of DMFT equations for nonhomogeneous systems (3.21)-(3.23) by using the following iterative procedure:

- Choose the initial self-energies $\Sigma_{i\sigma,l}(\omega)$ for each site, orbital and spin;
- Find the corresponding local Green's function $G_{i\sigma,l;i\sigma,l}(\omega)$ by inverting the matrix in equation (3.21) and extracting the diagonal elements $G_{ii}(\omega)$;
- Calculate the dynamical mean-field $\mathcal{G}_{i\sigma,l;i\sigma,l(\omega)}$for each site, orbital and spin by using equation (3.22)
- Use $\mathcal{G}_{i\sigma,l;i\sigma,l(\omega)}$ to solve the impurity problems in Equation (3.23);
- Find new self-energies by using equation (3.22);
- Continue iterations until $\Sigma_{i\sigma,l}(\omega)$ converged with desired accuracy.

The flow chart of the nonhomogeneous-DFT+DMFT code is presented in Fig. 11. In both the homogeneous and non-homogeneous cases, the problem can be solved for each frequency which makes it easy to parallelize. In the case of large nanoparticles, one needs to invert rather large matrices Eq. (3.21) which makes the calculation challenging, though as our studies show one can analyze 100-atom systems in a rather short time scale.

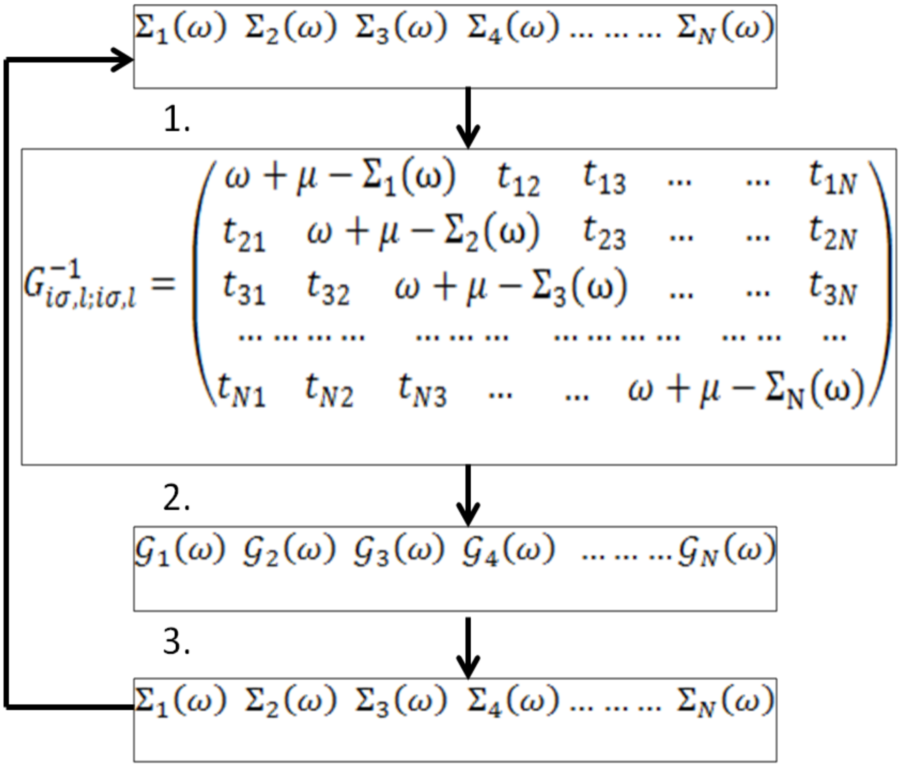

Figure 11: Flow chart of nonhomogeneous nanoDFT+DMFT formalism.

3.4 Iterated Perturbation Theory (IPT) Approximation

In this Subsection, we give details of the multi-orbital IPT (MO-IPT) approximation for the single-impurity problem which we used in our nanoDFT+FMFT code. To be more precise, the MO-IPT approximation is related to the expression for the self-energy, not impurity Green's function. The final result for the impurity Green's function can be obtained by using this self-energy and the bath mean-field in the Dyson equation (3.22). The advantage of the IPT solution is its speed, which is very important in the nanocase where one needs to solve many $2 \times N \times M$ impurity problems. In this case, the QMC, CT-QMC and other Monte-Carlo calculations are very slow, especially at low temperatures.[120] The Exact Diagonalization solver works well at low temperature, but it cannot be used when one has more than ~12 bath site.[121]

The IPT solver is based on the second order-perturbation theory (in U) solution of the impurity problem. It is physically transparent, computationally non-expensive, and found to give satisfactory solutions for a range of correlations from weak to strong.[17] As it follows from the results displayed in Fig.12, the IPT solution of the one-band problem includes, metallic, insulating and intermediate phases at different values of U, in agreement with more accurate solutions.

Let us present the expressions for the IPT self-energy in different cases.

<u>Half-filled case (n=1/2):</u> The IPT self-energy is expressed in terms of 2nd order expansion of Coulomb parameter U for a given bath field $\mathcal{G}$:

$$\Sigma(i\omega_n) = Un + U^2 \int_0^{\beta} d\tau e^{i\omega_n \tau} \mathcal{G}(\tau)^3 + \mathcal{O}(U^3), \tag{3.24}$$

or in the Matsubara frequency representation (with frequencies $\omega_n = \pi \mathrm{T}(2\mathrm{n}+1), \mathrm{n} - \mathrm{integer}$ [122])

$$\Sigma(i\omega_n) = Un - U^2 T^2 \sum_{\Omega_1, \Omega_2} \mathcal{G}(i\Omega_1)\, \mathcal{G}(i\Omega_2) \mathcal{G}(i\Omega_1 + i\Omega_2 - i\omega_n). \tag{3.25}$$

After the solution (3.25) found, one can obtain the real-frequency self-energy by performing analytical continuation $i\omega_n \to \omega + i\delta$ (we used Pade approximation[123] for this, see Appendix B). The Matsubara-frequency calculations are much faster as compared to the real-frequency ones.

As was mentioned above, Metal-Insulator Transition (MIT) can be successfully described correctly by this approach as shown in Fig.12, in which the spectral function $A(\omega) = -\frac{1}{\pi} ImG(\omega)$ is plotted for various values of U for a half-filled Hubbard system.[23] For small U's, the spectral function is similar to the bare lattice density of states. As the values of U increase, a narrow quasi-particle peak appears at the Fermi level, called Abrikosov-Suhl resonance. The two additional peaks as we see in Fig. 12 at values of $\pm U$ frequency correspond to lower and upper Hubbard bands. It is worth mentioning here that IPT not only reproduces MIT, but it also can reproduces exactly the atomic limit U$\rightarrow \infty$. Thus both limiting cases U$\rightarrow 0$ and U$\rightarrow \infty$ can be obtained from IPT.[23]

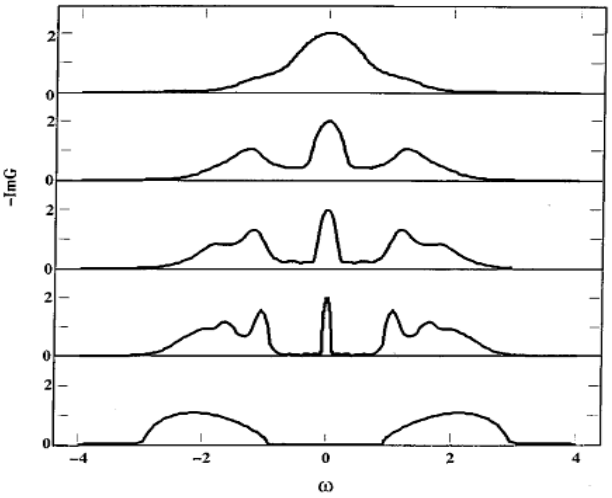

Figure 12: Spectral density of the infinite-dimensional one-band Hubbard model obtained using the IPT approximation for values of U=t, 2t, 2.5t, 3t and 4t (from top to bottom). Picture taken from [23].

Arbitrary filling: The generalized the IPT expression for the self-energy at arbitrary filling[124] is:

$$\Sigma(\omega) = Un + \frac{A\Sigma_0^{(2)}(\omega)}{1-B\Sigma_0^{(2)}(\omega)} \tag{3.26}$$

where $\Sigma_0^{(2)}(\omega)$ is the second-order self-energy Equation (3.23). This approximation was proposed to satisfy some exact properties of the self-energy, including the large-frequency

$$\Sigma(\omega) = Un + U^2 n(1-n)\frac{1}{\omega} + \mathcal{O}\left(\left(\frac{1}{\omega}\right)^2\right). \tag{3.27}$$

and large-U limits: [124]

$$\Sigma_{atomic}(\omega) = Un + \frac{n(1-n)U^2}{\omega-\epsilon_f-(1-n)U-i\eta} \tag{3.28}$$

where $n = \int_{-\infty}^{0} d\omega Im G_{loc}(\omega)$ is the physical particle number.

This leads to the following expressions for the A and B

$$A = \frac{n(1-n)}{n_0(1-n_0)} \tag{3.29}$$

$$B = \frac{(1-2n)U-\mu+\tilde{\mu}}{n_0(1-n_0)U^2}, \tag{3.30}$$

$\tilde{\mu}$ is the chemical potential of the bath problem and $n_0 = -\frac{1}{\pi}\int d\omega Im\mathcal{G}(\omega + i0)$ is the fictitious density for the particle in the bath.

There are different possibilities for the choices of $\tilde{\mu}$ as suggested by Potthoff et. al.[125] In this thesis we put $\tilde{\mu} = \mu$.

For the nonhomogeneous systems, the expression for the self-energy is very similar to Eq. (3.23), except the self-energy depends on each site, orbital and spin:

$$\Sigma_{i\sigma l}(\omega) = Un_{i\sigma l} + \frac{A_{i\sigma l}\Sigma^{(2)}_{i\sigma l}(\omega)}{1-B_{i\sigma l}\Sigma^{(2)}_{i\sigma l}(\omega)}, \tag{3.31}$$

where $\Sigma^{(2)}_{i\sigma l}(\omega) = U^2 \int_0^{\beta} d\tau \exp(i\omega_n\tau)\, \mathcal{G}^3_{i\sigma l}(\tau)$ in the Matsubara frequency representation, and

$$A_{i\sigma l} = \frac{n_{i\sigma l}(1-n_{i\sigma l})}{n_{i\sigma l0}(1-n_{i\sigma l0})}, \tag{3.32}$$

$$B_{i\sigma l} = \frac{(1-2n_{i\sigma l})U_{i\sigma l}-\mu+\widetilde{\mu}}{n_{i\sigma l0}(1-n_{i\sigma l0}){U_{i\sigma l}}^2}, \tag{3.33}$$

where $n_{i\sigma l} = \int_{-\infty}^{0} d\omega Im G_{i\sigma l;i\sigma l}(\omega)$ is the number of real physical particles with site, orbital and spin indexes and $n_{i\sigma l0} = -\frac{1}{\pi}\int d\omega Im \mathcal{G}_{i\sigma l;i\sigma l}(\omega + i0)$ is the fictitious particle density of the impurity bath.

3.5 DFT+DMFT code for nanosystems

The first step of the combined DFT+DMFT approach, as suggested by Anisimov *et al*. [21] (see also Refs.[20,108] and the references therein), is to calculate the electronic structure using DFT. The "non-correlated" quasi-particle characteristics such as band structure, density of states, projected density of states, and position of d-band center are all obtained from DFT. In the second step, one finds the parameters for the Hubbard Hamiltonian Eq. (3.1): the hopping parameters $t_{il;jm}$ and the onsite Coulomb repulsion parameters U.

The hopping parameters are equal to the matrix elements of the non-interaction Kohn-Sham Hamiltonian with respect to the localized atomic-orbital wave functions:

$$t_{ij\alpha\beta} = \int d\mathrm{r}\psi_\alpha^*(\mathrm{r}+\mathrm{R_i})\left(-\frac{\nabla^2}{2m} + V_{atomic}(r)\right)\psi_\beta(\mathrm{r}+\mathrm{R_j}) \tag{3.34}$$

where $\mathrm{R_i}$ and $\mathrm{R_j}$ represent site index and α, β represents orbital and other quantum numbers index. To determine the hopping between different orbitals on different atoms we used the Slater-Koster approximation[126] (for details, see Appendix A). The values of U were used as parameters, though as it was discussed in the DFT+U part, the values of U can be in principle obtained from DFT calculations.

In the third step, the set of DMFT equations is solved to find the electron Green's function and different properties of the correlated system. To take into account correlation effects from the first stage in some case, we performed DFT+U calculations instead of DFT (to obtain the relaxed nanoparticles).

In case of finite systems the formalism of DFT+DMFT is basically same as for the extended system, but in the nanocase it is more convenient to solve the problem in real space representation. The schematic of DFT+DMFT approach is presented in Fig. 13.

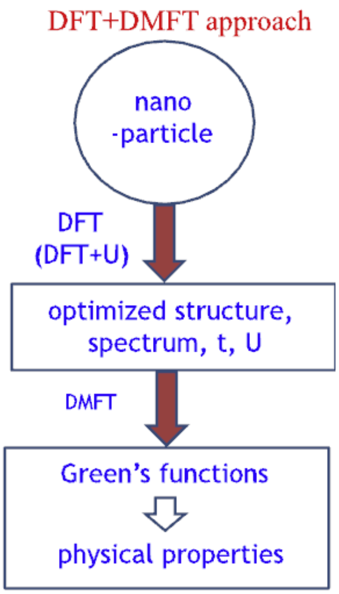

Figure 13: The steps of nanoDFT+DMFT approach are shown schematically here. Figure taken from ref [127].

In the next Chapter, we present our results of application of the nanoDFT+DMFT formalism on the cases of small (2-5-atom) Fe and FePt clusters and Fe (10-147-atoms) nanosystems.

CHAPTER 4 APPLICATION OF NANO-DFT+DMFT TO NANOMAGNETISM

In this chapter, we present our nanoDFT+DMFT results for the magnetic properties of small (2-5-atom) Fe and FePt clusters as well as larger Fe particles of nanosize (up to 147 atoms). We begin with the Computational details for the DFT part of the simulations and with the results for the bulk bcc Fe and proceed with the case of clusters and nanosystems.

4.1 Details of preliminary DFT calculations

To obtain the lattice parameter of bcc bulk iron and structural relaxation of small Fe and FePt clusters we used the spin-polarized DFT approach as implemented in the VASP code.[128] In describing the electronic exchange and correlation effects, we used the spin-polarized GGA with the PW91 functional[88] and the spin interpolation proposed by Vosko *et al.*[129] For the ionic relaxations, we employed the conjugate-gradient algorithm. To describing the electron-ion interactions, we used the projector augmented-wave (PAW)[130] formalism. To take the correlation effects into account in a more consistent way we relaxed the structures for every value of U used in the consequent DMFT calculations. For bulk calculations we used 12x12x12 k-points sampling in the Brillouin zone. The configurations of small clusters were obtained by relaxing random initial configurations with bulk interatomic distances.

In the case of Fe_{10}-Fe_{147} particles, the spin polarized-DFT methods as implanted in the Quantum Espresso Code[131] was used for relaxation with the PBE [87] version of the XC potential. For all cluster relaxation cutoff-energy for the plane-wave expansion was

450 eV and structures were relaxed until the atomic forces converged to less than 0.01eV/Å. A cubic simulation box was used during relaxation to isolate the freestanding clusters in such a way that the minimum distance between each cluster and its periodic images in all three directions be larger than 12Å. This is done to minimize the possibility of electric field interaction between a cluster and its images. Calculations were performed at only one (Γ) point in the Brillouin zone. To choose the initial structure of larger Fe nanoparticles we proceeded as follows: the initial Fe_{19}-Fe_{147} cluster structures were chosen from the Cambridge Cluster Database[132] with the global minimum energy obtained by using Finnis-Sinclair pair-potentials[133] with bulk inter-atomic distances. For smaller clusters we proceeded as follows. The initial structures of the Fe_{18} cluster were obtained by removing one of the 19 atoms from the relaxed Fe_{19} cluster, relaxing the corresponding structure, and choosing the minimum energy configuration. Similarly, we proceeded with smaller clusters, $Fe_n \rightarrow Fe_{n-1}$, down to Fe_{10} system.

4.2 Warm-up: Magnetism in bulk iron

To test the accuracy of the IPT approximation to solve the DMFT impurity problem, we first applied our code to calculate the DOS of the bcc bulk Fe. The spin-DFT with LDA or GGA XC is able to describe the lattice structure and the magnetism in the bulk Fe, but it fails in the case of electronic spectrum of the system.[134] In particular, the experimentally-observed Hubbard satellite peak at -7eV below the Fermi energy[135,136] cannot be reproduced with LDA or GGA.[134] The results of our DFT, DFT+U and DFT+DMFT calculations of the DOS of bulk Fe are shown in figure 14.

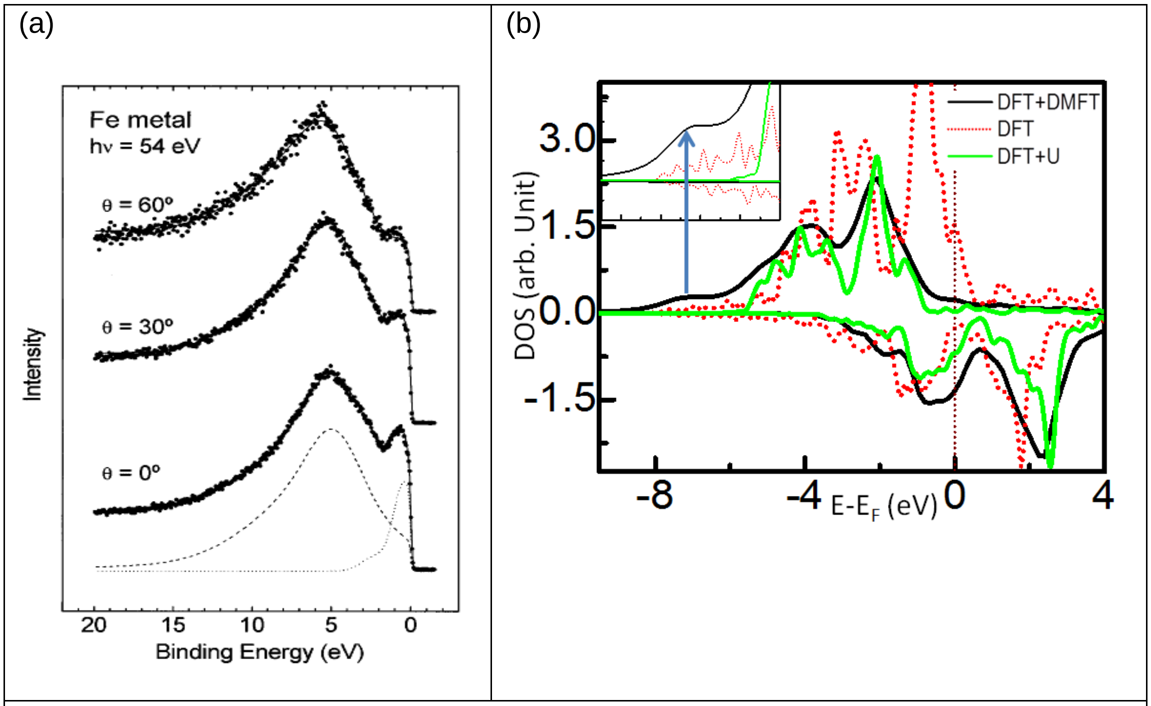

Figure 14: (a) Photoelectron spectra of bulk Fe taken at a photon energy of 54 eV on resonance for three different angles, shows a satellite peak at ~-7 eV.(figure taken from [136]),(b) Calculated DOS of bulk Fe obtained with different method: spin-DFT (red dotted line), DFT+U (green solid line) and DFT+DMFT (black line). DFT+DMFT curve clearly reveals a satellite peak at ~-7 eV (inset is showing the satellite peak with high resolution).

Other DFT+DMFT calculations with more computationally expensive impurity solvers, for example the spin-polarized T-matrix fluctuation exchange solver (SPTF),[134] is also capable of reproducing this peak. Here, taking the example of bulk Fe, we demonstrated that much computationally-cheaper IPT solver is also capable of correctly describing the properties of transition metal systems. Since in the case of nanoparticles the computational cost is an issue, we use the IPT solver in most cases of our analysis.

4.3 Small transition metal clusters

Theoretical study of small clusters is very important due to several reasons. One of them is in getting a useful insight about the quantum confinement in systems, which are difficult to study in experiments. Another reason is necessity to understand the growth dynamics of large nanoparticles and thin films. Such an understanding can be also obtained from the properties of small clusters. Magnetism of these systems is another hot area of research. It was found experimentally that the magnetic moment per atom in Fe, Co and Ni clusters has an oscillatory dependence on the number of atoms in the cluster.[33] Understanding of the electronic and other properties of small transition clusters may also help to resolve the mystery of this oscillatory behavior. Deep understanding of the properties of small clusters will also help to predict the effects of their interaction with substrates (such small clusters are highly reactive). Indeed, most of the experimental studies on small magnetic clusters are performed in the case of particles on a substrate [137-139], and the role of the substrate in the system magnetism needs to be taken into account. The accuracy of standard (DFT) approaches used to study TM clusters may be questionable in many cases, due to their over-simplified treating of the electron-electron correlation effects. In the systems with reduced dimensionality, the effects of local electron-electron interaction on the d- and f-orbitals, are even more important than in the bulk due to confinement effects (electrons 'meet more often' in small systems). In this chapter, we use a reliable nanoDFT+DMFT approach to study the role of the correlation effects in the magnetic properties of Fe and FePt clusters.

The DFT and DFT+U (relaxation) part of the calculations were performed by using VASP code (details are given in section 4.1). The DMFT calculations in the case of small particles were performed by using the LISA code[20] with the Hirsch–Fye QMC impurity solver.[116] Since this code is applicable to periodic systems, we assumed that every cluster occupies a site on a two-dimensional lattice. In this case, the (2-5-atom) system may be regarded as one large multi-orbital "superatom" with the number of orbitals equal to the product of the number of atoms and the number of orbitals in the atom. We used a large lattice constant 20Å, in order to minimize the effects of images on the cluster magnetization. The hopping parameters for the for the *s*- and *d*-electrons in the Hubbard Hamiltonian were obtained from the relaxed structure (inter-atomic distances) by using the Slater–Koster matrix approximation.[126,140] (for details, see Appendix A). In Slater-Koster approximation, the hopping parameters are defined by the interatomic distances, orbital orientations and their charge radii (except s-orbital). In particular, the values for the *d*-orbital radius r_d were approximated by the Muffin–Tin-orbital values 0.864 Å (Fe) and 1.116 Å (Pt) atoms.[140]. The values for the Coulomb repulsion U were chosen as parameters, and the calculations were performed for Us from 0eV to 5eV (with the bulk Fe value U=2.3eV as a reference number). In the case of iron clusters, we rescaled the hopping parameters by a factor of 0.367 in order to reproduce the average experimental value for the spin-up and spin-down bandwidth in the bulk material. One may regard rescale of hopping as a change in the value of the Coulomb repulsion U, since the physical properties of the systems are mainly defined by the ratio between the hopping parameters and U. To make the calculations consistent, we have used the same renormalization also for the FePt clusters. In the DMFT calculations for such a periodic system of clusters, we allowed a weak (0.1eV) inter-cluster ("inter-site") hopping to achieve faster convergence. To generate ferromagnetic spin ordering, a weak staggered external magnetic field was also used. The DMFT calculations appear to become slower value of U (T) increases (decreases). However, the magnetic properties of the system are practically temperature-independent at temperatures much lower than values of kinetic energy (hopping) and Coulomb repulsion U, that define the other energy scales in the system. Therefore, in our DMFT calculations, we used such temperatures, as an approximation for the $T \to 0$ case.

4.3.1 Iron clusters

The problem of magnetism in small Fe clusters has been widely studied by using DFT (see, e.g.,[36]) and more recently DFT + U approaches[42,44,49]. Though rather limited, the available experimental data on such systems [52,141,142] allows one to test the accuracy of different numerical approaches. In general, it appears that DFT and

DFT+U often give over-estimated values for the cluster magnetic moments, which might be a result of over-simplified treatment of the effects of electron correlations.

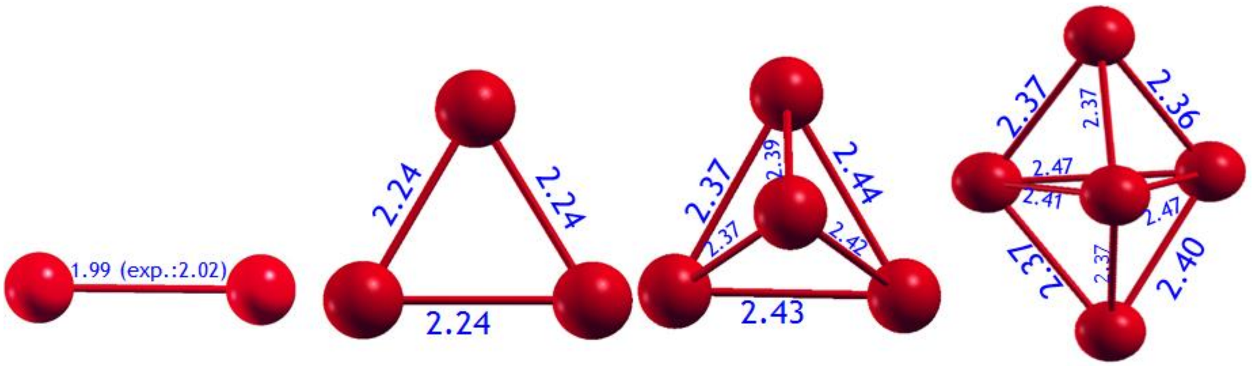

Figure 15: The DFT+U (U=2.3eV) optimized structure of Fe 2-5 atoms clusters (The corresponding bond lengths (in Å) are shown in blue).

As mentioned above, the relaxation of the systems was performed by including the correlation effects through the DFT+U approximation. For this purpose, we used the bulk Fe value of Coulomb repulsion parameter U = 2.3 eV. The obtained relaxed structures have the geometry shown in Fig. 15. In the dimer case, we obtained the bond length 1.99 Å, which is in good agreement with the experimental estimations 1.87 Å [141] and 2.02 Å [142]. The average bondlengths for larger clusters are larger than these values but smaller than the nearest-neighbor inter-atomic distance in bulk Fe, 2.49 Å. In the trimer case, the lowest-energy configuration is an equilateral triangle with 2.24 Å sides, and in the Fe_4 and Fe_5 clusters cases we find a single-sided pyramid (two sides 2.37 Å and others 2.39 Å, 2.42 Å, 2.43 Å and 2.44 Å) and a bi-pyramid (four sides

2.37 Å, two sides 2.47 Å, and others 2.36 Å, 2.40 Å and 2.41 Å) to be the ground-state configurations.

Our DFT+U calculations resulted in values of the magnetization per atom much larger than the bulk value 2.2$\mu_{B,}$ even in the U=0eV (DFT) case. As can be seen from the results plotted in Fig. 16, the magnetization grows with increasing U, reaching a saturated value at some critical value of the Coulomb repulsion U_{cr}~$1-3\ eV$. The value of U_{cr} depend on the cluster size in a non-trivial way.

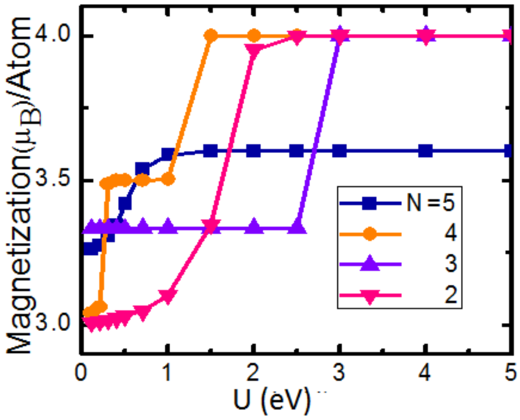

Figure 16: DFT+U results for the magnetization of the clusters at different values of U.

Indeed, since the average inter-atomic distance d_{av} increases as N increases, one might expect decreasing U_{cr} with increasing N (due to the decrease in hopping amplitude). On the other hand, growth of the average coordination number with increase of N should lead to an increase of U_{cr}. Therefore, there is no simple quantitative explanation of how U_{cr} depends on N.

The DFT+DMFT calculations give rather different results for the magnetization of small Fe clusters. In particular, in the case of Fe_3 and Fe_4 clusters, one gets a significant reduction of the magnetic moment with respect to the DFT+U values. The results of our DFT+U and DFT+DMFT calculations are also presented in the figure 17. One can get similar results for other clusters as well. As it follows from this figure, dynamical effects play an important role even at rather small values of U, leading to a significant reduction of the cluster magnetization.

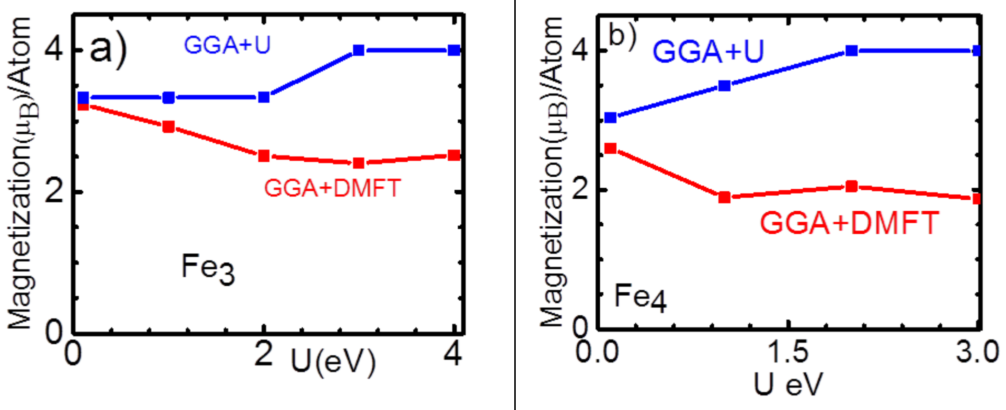

Figure 17: DFT(GGA)+U (blue line) and DFT+DMFT (red line) results for the magnetic moment per atom in the Fe_3 and Fe_4 cluster as function of U.

The conclusions above are confirmed also by the results summarized in Table 1. In this Table, we present results for cluster magnetization as a function of the number of atoms at U = 2.3 eV (for more details see Ref.[47,48]). Once again, the DFT+U calculations tend to overestimate cluster magnetic moments and dynamical effects in general lead to a reduction of the magnetization. Both methods are not able to reproduce accurately the experimental values of the magnetization, which is overestimated by DFT+U and somewhat underestimated by DFT+DMFT. The experimental values of magnetization for the selected small clusters were used here to test the DFT+DMFT approach in the limiting case. Several others, including DFT [43,143-145], approaches also give the magnetization values within (quite large) experimental error bars, which are quite large.[52] However, while the DFT+DMFT is not expected to accurately describe magnetism in such small clusters, our results clearly demonstrate that the approach gives reasonable results even in such limiting case (with small inter-atomic coordination number – the case where applicability of DMFT was under question for a long time). One may expect the accuracy of DMFT approximation to dramatically increase in the case of larger clusters which will make it superior over DFT and DFT+U, what was confirmed by our further studies.

Table 1: The magnetization per atom as function of the number of atoms in the case of small Fe clusters at U = 2.3 eV. Theoretical DFT+U and DFT+DMFT results and the experimental data[52] are shown.

N	DFT+U (in μ_B)	DFT+DMFT (in μ_B)	Experiment (in μ_B)
2	4.00	2.03	3.25 ± 0.50
3	3.33	2.22	2.70 ± 0.33
4	4.00	1.84	2.70 ± 0.80
5	3.60	1.98	3.16 ± 0.33

The results in Table 1 are compared to the results obtained by different approaches by other authors in Fig.18. As follows from our calculations, in general the DFT + *U* approach overestimates the value of the magnetization for most of the clusters in comparison with many other calculations and available experimental estimations. This overestimation is especially pronounced in the case U=4eV.

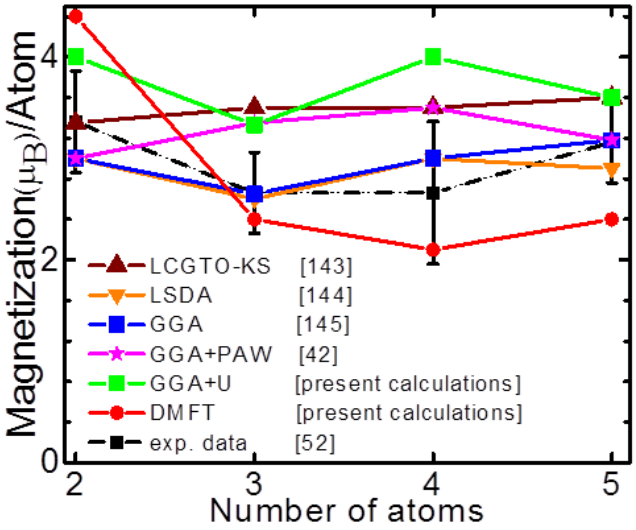

Figure 18: The DFT+*U* and DFT+DMFT results for the magnetization of iron clusters of different sizes with different numbers of atoms at U=4eV. The experimental data and theoretical results obtained within other approaches are also presented. Here LCGTO-KS stand for Linear Combination of Gaussian Type Kohn Sham Orbital.

Except for the case of the dimer, DFT+DMFT results are in a good agreement with experimental data, much better than the DFT+U and some of the DFT calculations.

We complete our analysis on the small iron clusters by studying the role of dynamical effects in cluster magnetization by considering the case of Jahn–Teller distorted iron trimers under the GGA +*U* and GGA + DMFT approaches. The used structures were obtained by GGA + *U* in[42]. As it was shown in this work, the trimer with Jahn–Teller distortion has lower energy as compared to clusters with higher symmetry, and the distortion often leads to a reduction of the cluster magnetic moment.

Table 2: The cluster geometry and the magnetization of Fe_3 clusters for different values of *U.* The results for both symmetric and the Jahn–Teller-distorted clusters, obtained within the GGA + *U* [42], are presented. The magnetization was calculated within GGA+U and GGA + DMFT approximations. $d_1 - d_3$ are inter-atomic distances (in Å). In the last column, the relative energies of different structures are shown.[42]

U (eV)	d_1	d_2	d_3	Magnetization (in μ_B)		E (meV)
				DFT+U	DFT+DMFT	
1.0	2.151	2.253	2.316	3.33	1.44	0
	2.264	2.264	2.412	4.00	1.52	14
1.5	2.266	2.266	2.431	4.00	1.57	0
	2.152	2.257	2.327	3.33	1.51	27

The DFT+U and DFT+DMFT results for the trimer magnetization in cases of different values of U *(*1.0 and 1.5 eV) are presented in Table 2. As it follows from the Table 2, inclusion of the dynamical effects does not change qualitatively the geometric dependence of the DFT+U magnetization of the distorted clusters, but the magnitude of the magnetic moments is much smaller in the DFT+DMFT case. Inclusion of the local charge interactions through DFT+U leads to a soft of the orbital energy levels [42], which on its turn leads to a change of the cluster magnetic moment. Significantly lower values of the DFT+DMFT magnetization suggest that the orbital position and/or occupancy may be dramatically changed (through the electron self-energy) when the dynamical effects are taken into account.

4.3.2 FePt clusters

Magnetic properties of small FePt clusters are also an important theoretical problem especially because of a high MCA of the FePt systems. Though, the number of theoretical works dealing with small FePt systems is more limited compared to the Fe case.[53,56] One of the reasons for this is lack of experimental data for these systems. Thus, a systematic *ab initio* analysis of these systems, including the evolution of their properties with size, is very important from both theoretical and practical points of view. In general, the magnetic bimetallic clusters are of special interests for several reasons. In particular, it is important to understand how the addition of localized (5d-) states of the nonmagnetic metal element affects the magnetic properties of the “magnetic” atoms with different (3*d-) localized orbitals*. As we mentioned above, the choice of FePt was motivated not only from the point of view of fundamental physics, but from several practical reasons.

We considered two types of the FePt clusters: the dimer and the tetramer, with different chemical compositions. The analysis of dimer allows one to perform a deep qualitative analysis (due to simplicity of the structure) of the role of the 3*d* and 5*d* orbitals in magnetism of the system. The tetramers were chosen mostly to analyze the dependence of magnetism on the chemical composition of the TM clusters.

Contrary to the Fe clusters, it was found that the geometry of the FePt clusters strongly depends on the value of U. In our studies we chose the relaxed structures obtained with DFT+U approach with characteristic value of U=4eV. The optimized cluster geometry in this case is presented in Fig. 19.

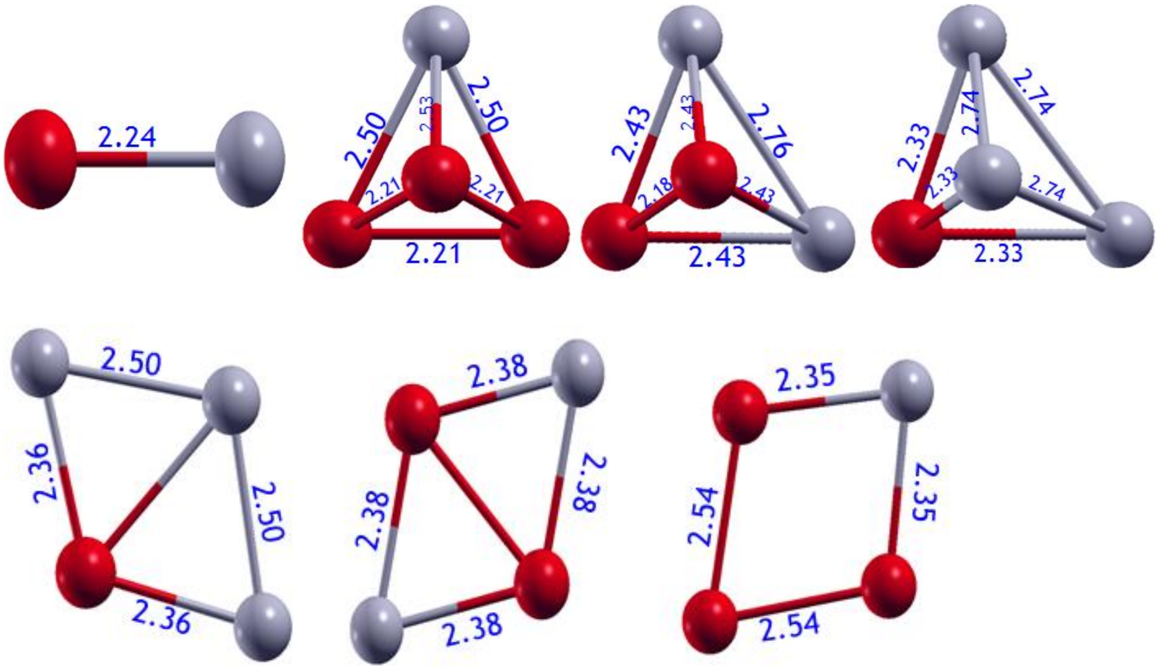

Figure 19: Optimized cluster geometry for FePt obtained with DFT+U at U=4eV. Red sphere corresponds to Fe atom and brown sphere corresponds to Pt atom. Bondlength (in Å) for each for each pair of atoms are also shown (blue numbers). Top panel (except dimer) shows 3D structures and the planer structures are shown in the bottom.

For majority of the tetramer structures, the planar configurations have lower energy. Namely, the relative energies for the planar and 3D tetramers are: Fe_1Pt_3 – planar: −0.13 eV, 3D: 0 eV; Fe_2Pt_2 – planar: −0.63 eV, 3D: 0 eV; Fe_3Pt_1 – planar: 0 eV, 3D: −0.13 eV. This is a surprising result, especially including the fact that the average bond length is longer in the planar systems, as compared to the 3D ones. On the other hand, longer bondlength result in stronger electron localizations, which increase the role of the correlation effects.

The DFT+U results for the magnetization of Fe and FePt dimers at different values of U are presented in Fig. 20. This Figure shows that the magnetization is almost U-independent in the FePt case (the value of the magnetization $2\mu_B$ per atom is in agreement with other DFT calculations [53]), but it experiences a sharp increase at $U \sim 3$ eV in the case of the Fe_2 system.

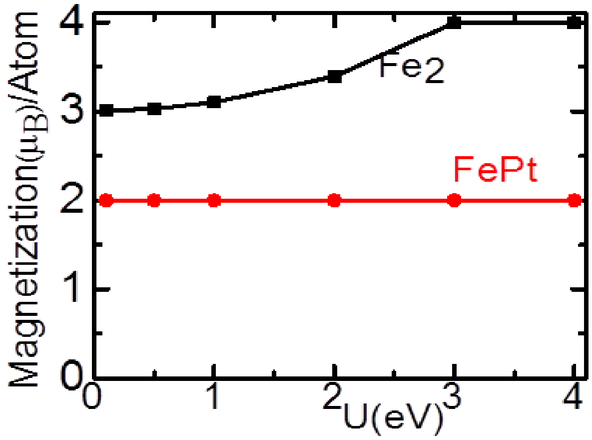

Figure 20: DFT+U results for the magnetization at different values of U for the Fe and FePt dimer.

This result can be explained in the following way. The bondlength increases with increasing U. Since the value of U~3 eV is a typical critical value for the Mott transition in bulk TM systems and the change of the cluster magnetization is rather sharp at this point, one may speculate the presence of some kind of transition at this U in the case of clusters as well. Weak dependence of the magnetization on U in the FePt cluster can be explained by a weaker hybridization of the Fe and Pt *d*-orbitals, as compared to the hybridization of the Fe atom orbitals in the Fe_2 case due to a larger energy mismatch in the FePt system even at U=0eV. Therefore, increasing U which leads to an increase of the bond length does not lead to significant charge redistribution (localization) in the FePt system. The DFT+U calculations give much larger bondlength for the FePt dimer: 2.29 Å vs. 1.99Å in the Fe_2 system. These results were obtained at U = 2.3 eV, and with U increasing the bondlength increases for both systems. For instance, at U=4eV the FePt bondlength is 2.34 Å (one can also get the value 2.2 Å in the case U = 0 eV[53]). The role of the correlation effects in the spectral properties of the dimers was analyzed also by calculating the positions of the *s*- *d*-state peaks as functions of U for Fe_2 and FePt systems (Fig. 21). The distance between the spin-down peaks (two red lines) and spin-up *d*-orbital peaks (top blue solid line) significantly increases when U changes from 2 eV to 3 eV for iron dimer, which suggests that the probability of migration of electron between different spin-orbitals, which decreases the average magnetization, is low at large Us.

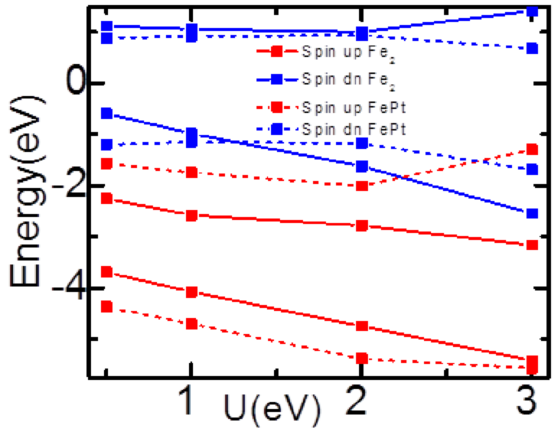

Figure 21: DFT+U results for the positions of the *s*- and *d*-energy peaks in the DOS of the Fe_2 and FePt clusters at different values of U.

This may explain the magnetization jump in Fig. 20. In the case of FePt cluster, there is no such sharp change between the energy differences for these states (the corresponding dashed lines in Fig.21), and therefore, the magnetization does not change significantly as U increases. Another notable effect of U in the case of FePt cluster is change of the positions of the d-orbital spin-up and spin-down energies when U increases from 2 eV to 3 eV.

For the case of tetramers, we have performed DFT+U and DFT+DMFT studies of the U-dependence of the magnetization for two types of systems with bulk and planar configurations on the example of Fe_3Pt (Fig. 22). Our DFT+U results show an increase of the magnetization at large values of U in the 3D structures. This is an expected result, since the correlation effects in the 3D structures are more sensitive to the distance between the atoms as compared to the planar ones (where the correlation effects are significant even at small U's due to large inter-atomic distances).

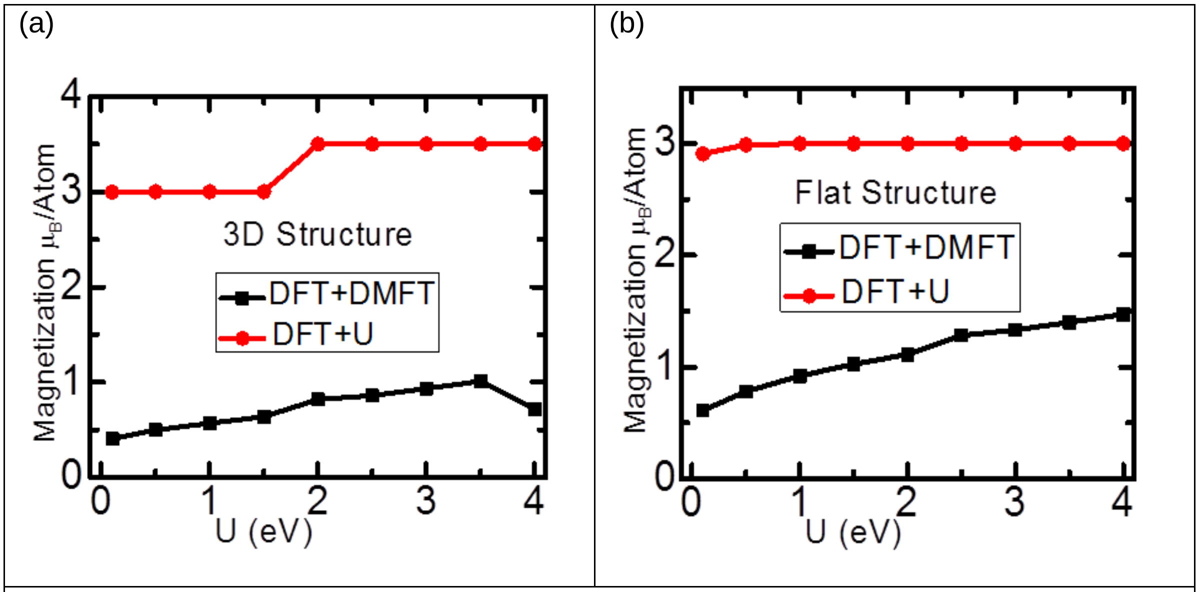

Figure 22: DFT+U vs DMFT results for the magnetization of the Fe_3Pt clusters (shown in Fig. 18) as a function of U in the case of 3D (a) and planar (b) geometries

The reduction of magnetization due to dynamical effects, taken into account in the DMFT in Fe_3Pt is much larger than in the case of pure iron four-atom cluster (Fig. 15(b)). Indeed, substitution of an iron atom by a platinum one, leads to an increase (decrease) of the corresponding bondlength (hopping parameter). This happens because of a larger spatial extension of the 5d-orbitals. As a result, the average time of the orbital occupancy decreases, which leads to a decrease of the magnetization.

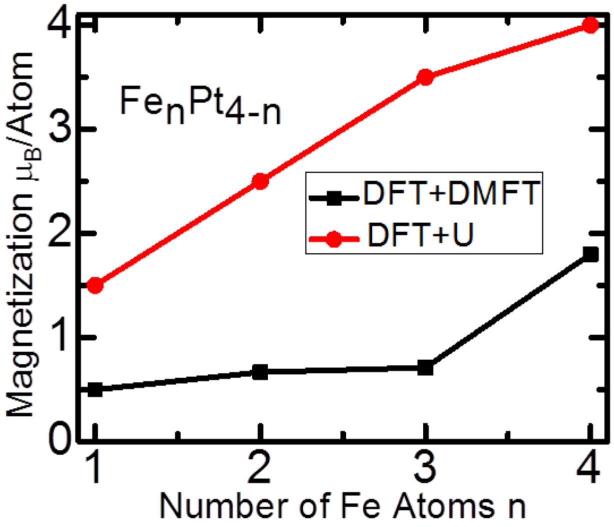

Figure 23: DFT+U vs DMFT results for the magnetization of the four atom iron–platinum clusters as function of the number of iron atoms at U = 4 eV

The dependence of DFT+U and DFT+DMFT magnetization on the chemical composition of the FePt tetramers is presented in Fig. 23. Naturally, the “staggered” mean-field DFT+U calculations show a fast increase of the magnetization with increasing of the number of “more magnetic” Fe atoms. On the other hand, the DFT+DMFT calculations show that the magnetization of the bimetallic clusters is rather small and almost composition-independent, suggesting that the hybridization effects are dominant even in the case of large U’s. Interestingly, the DFT magnetization of the Fe_2Pt_2 cluster [53], ~$2\mu_B$, is much closer to our DFT+U result than to the DFT+DMFT one. This suggests that the DFT energy levels in the system are well separated, and inclusion of U does not affect significantly the orbital hybridization (U typically leads even to a larger separation between the atoms). On the other hand, the dynamical effects may lead to a significant change of the system spectrum, and hence its magnetization, even in the case of strongly localized orbitals.

4.4 Fe nanoparticles

After we have successfully applied DFT+DMFT approach to small Fe and FePt clusters, we proceeded with the case of larger, 10-147-atoms, Fe nanoparticles. The DFT-relaxed geometries of the studied cluster and the atomic magnetic moments for different clusters are presented in the Fig. 24

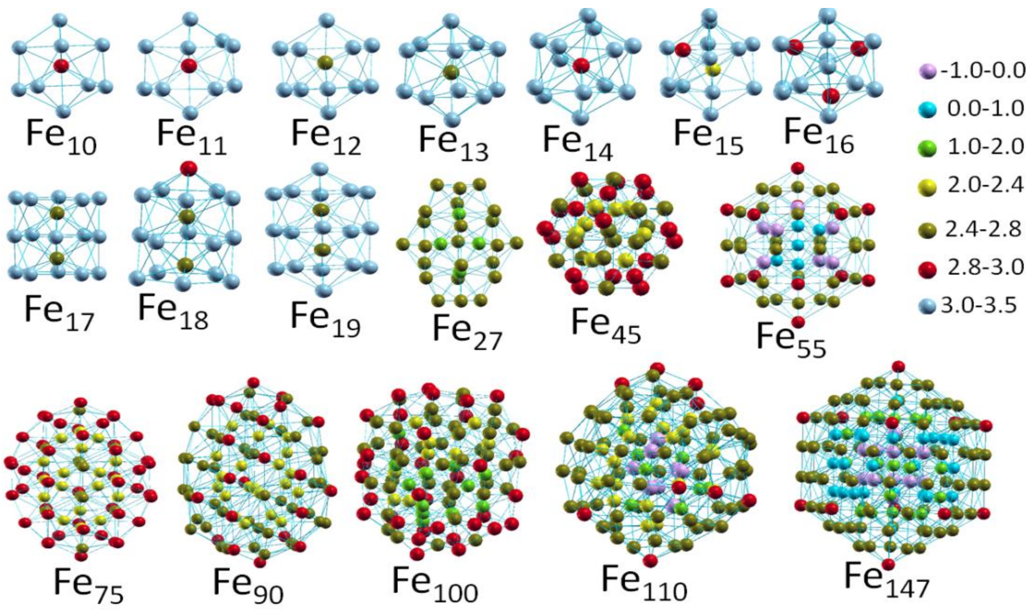

Figure 24: Relaxed structures of the Fe$_{10}$-Fe$_{147}$ clusters. Different colors correspond the values of the atom magnetization shown on the right (in μ_B).

In general, the surface atoms have much higher magnetization, which increases with decreasing cluster size. Smaller magnetic moments of inside atoms can be explained by their larger coordination number. High coordination assumes the ferromagnetism of more itinerant-like type, similar to the bulk. Indeed, the values of magnetic moments of the inside atoms are of order of the bulk value (~2.2muB). In some cases (Fe_{55}, Fe_{110} and Fe_{147}), we found a local anti-ferromagnetic order inside the clusters (shown in pink). The antiferromagnetic ordering disappears with including U correction in DFT+U. This again suggests that the magnetic properties of the central part of the system is basically of the itinerant type (with U making the system more of atomic type, suppressing the kinetic processes). In order to better understand the nature of the magnetic ordering in the clusters we also analyzed the bondlength distribution in different systems. The results are presented in figure 25.

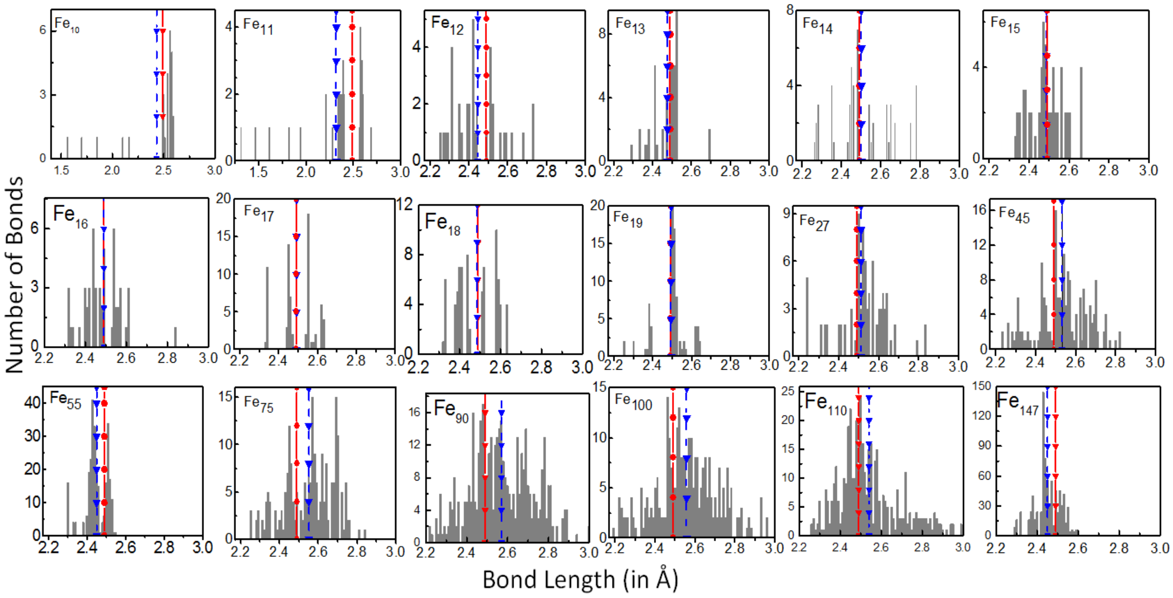

Figure 25: The bondlength distribution in the Fe_{10}-Fe_{147} clusters. The red line indicates the bulk Fe lattice constant and the blue dashed line is the average bondlength of each cluster.

As it follows from Fig.25, the average bondlength changes non-monotonously with the cluster size. Surprisingly, the average bond length is the most different from the bulk value in the case of large 55- and 75- and 100-atom clusters. The bondlength value is closest to that for bulk systems in icosahedral Fe_{55} and Fe_{147} structures. Though the corresponding bondlengths are a little bit smaller than that for the bulk, opposite to the case of Fe_{45}, Fe_{75}, Fe_{90}, Fe_{100} and Fe_{110}. Very short, below 2 Å, values of some of the bondlengths in the 10 and 11-atom clusters might be the reason why DFT and other approaches fail to describe correct magnetic moment in this cluster. Since there is no simple correlation between the magnetization and the average bondlength in different clusters, it is quite possible that the simple Heisenberg exchange picture is not sufficient to describe the magnetism in these particles.

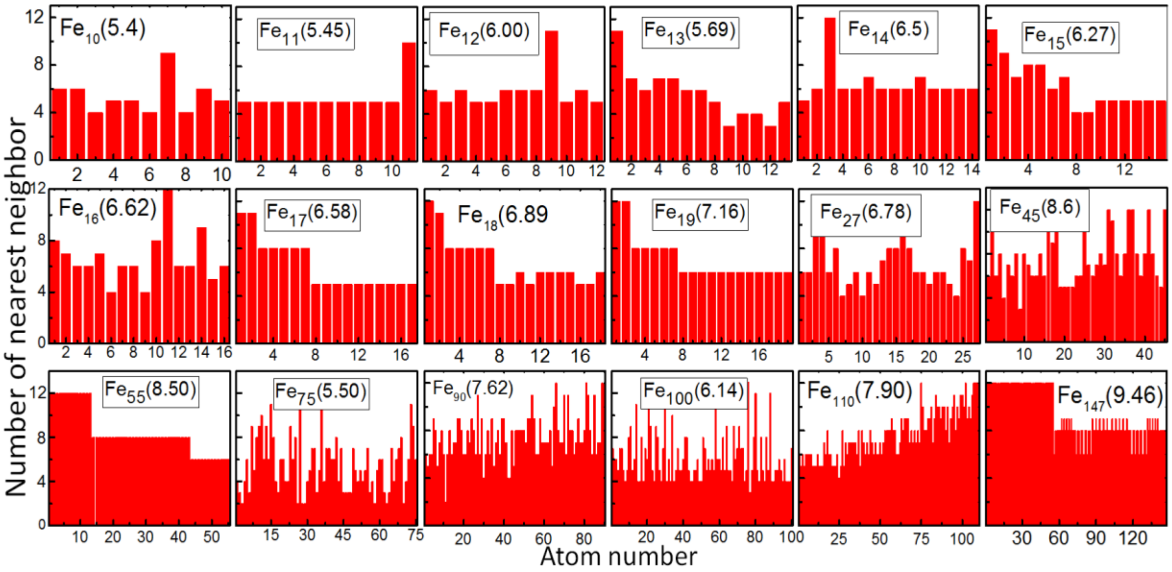

Figure 26: The number of nearest neighbor atom distribution for different clusters (at the cut-off radius 3.0 Å). In the brackets we show the average number of nearest neighbors per atom.

There is also no one-to-one correspondence between the number of nearest neighbors and magnetization, as it follows From Fig. 26. This suggests that the simple itinerant (Stoner) picture of the ferromagnetism is also not sufficient to describe the magnetic properties of the Fe particles. In fact, one would expect the increase of the number of nearest neighbors would lead to an enhancement of band-type effects (with the "band" splitting more pronounced in clusters with higher atomic coordination), and hence larger magnetic moments, which is not the case.

After structural relaxation, we have obtained the parameters for the effective Hubbard model solved in DFT+U and DFT+DMFT. Namely, the energies for s- and d- orbitals for spin-up and spin down-states $\varepsilon_{l,\uparrow}$ and $\varepsilon_{l,\downarrow}$ and also the inter-atomic and the inter-orbital hopping parameters $t_{ij}^{l_i,l_j}$ were obtained using the Slater-Koster approximation (for details, see Appendix A). We complemented these values with the value of the local Coulomb repulsion energy U=2.3eV, appropriate for the bulk iron system.

To solve the problem of correlated electrons, we turned to DFT+DMFT using our nano-DMFT code (particulars described in chapter 3). One virtue of the code is that it works for several hundred atoms with modest computational resources. The results for the magnetic moment per atom obtained using the three theoretical approaches and the experimental data are presented Fig. 27. Several conclusions can be made from these results. The first is that DFT+DMFT gives overall the best agreement with experimental data.

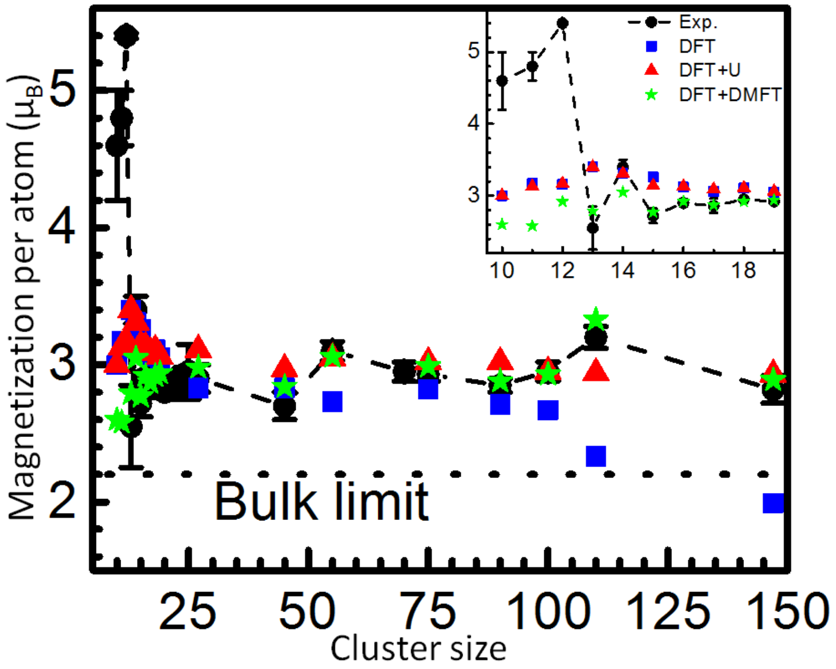

Figure 27: The DFT, DFT+U, and DFT+DMFT and the experimental data [34,58] for the magnetization per atom in the Fe clusters. More detailed results for smaller clusters are showing in the inset.

Next, only DFT+DMFT displays the peak in the magnetization observed in experiments for Fe_{14}. Although the numerical value of the magnetic moment (~3.3μ_B) obtained by DFT and DFT+U for this cluster is in better agreement with the experimental result (~3.4 μ_B), these two techniques find Fe_{13} to have higher magnetic moment (~3.4 μ_B) than Fe_{14}, in disagreement with experiments (~2.55 μ_B). In the Fe_{15} case, DFT and DFT+U also overestimate the magnetization, while DFT+DMFT result is in a good agreement with experimental data. Here again DFT+DMFT does better to describe large oscillations in the magnetization for Fe_{45} and Fe_{55} particles. In particular, DFT predicts the magnetization to be larger for Fe_{45}, while DFT+U find a smaller change (increase) in magnetization between Fe_{45} and Fe_{55}. For the clusters larger than 55 atoms both DFT+DMFT and DFT+U give similar results. In general, DFT+DMFT results are in better agreement with experiments, particularly in depicting the oscillatory dependence of the moments on the particle size. DFT results deviate the most from the experimental values, especially in the case of large 110- and 147-atom clusters, which in part can be explained by artificial core anti-ferromagnetism obtained in only with DFT. DFT+U tend to overestimate the magnetic moments for small clusters. For small, $Fe_{10,}$ Fe_{11} and Fe_{12}, clusters none of the approaches reproduces the high value for the magnetization, though the DFT+DMFT reproduces a local magnetization peak for Fe_{12}.

For a deeper understanding of the oscillation of magnetization, including the origin of the peaks at some values of *N*, we compared the DFT, DFT+U and DFT+DMFT spectral functions for Fe_{14}, Fe_{55}, Fe_{13} and Fe_{45} clusters (Fig. 28). The spectral function for spin-up electrons obtained with the DFT+U was found to be essentially the same as the DFT one but shifted to lower energies. The spectral density for the spin-down curves was found to be very similar in both DFT and DFT+U cases. Since the spin-up orbitals are typically fully occupied, the change of the magnetization with U is basically defined by the change of the spin-down density of states.

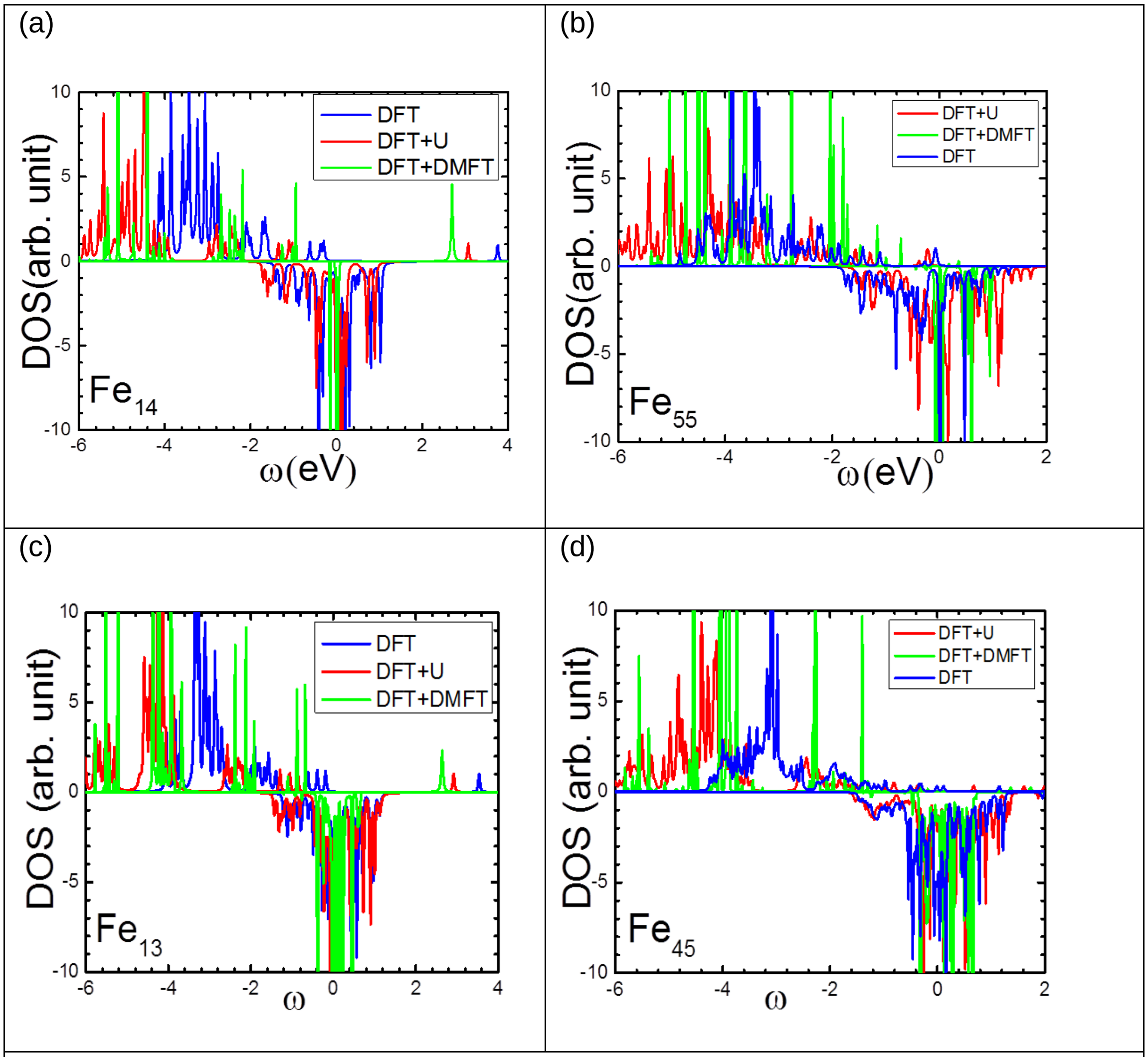

Figure 28: The DFT, DFT+U and DFT+DMFT spin-up (positive) and spin-down (negative) densities of states (arbitrary units) of the (a) Fe$_{14}$, (b) Fe$_{55,}$ (c) Fe$_{13}$ and (d) Fe$_{45}$ clusters. The Fermi energy corresponds to $\omega = 0$.

We found that the dynamical fluctuations taken into account in DFT+DMFT lead to a modification of the DFT+U density of states, in a way that recovers the DFT results. Reduction of the clusters magnetization obtained with DFT+DMFT may indicate that the orbital position (through static shift of energy levels resulting from the self-energy correction) and/or their occupancy (due to the frequency dependence of the self-energy) may significantly change when dynamical effects are taken into account. What is even more important that the DFT+DMFT give new orbitals (due to the frequency-dependence of the self-energy), as it follows from Fig. 28, that can significantly affect the value of the magnetization. Importantly, in the 14- and 55-atom clusters with the local peak for the magnetization, the DFT+DMFT spin-down density of states is strongly localized around the zero-level for all orbitals (Fig.28 (a) and (b)), distinctly from other clusters. For example, in the case of 13- and 45-atom clusters the spin-down DOS (Fig.28 (c) and (d)) is significantly more spread then the DOS of the corresponding “neighbor” 14- and 55-atom clusters. This ‘universal-localization’ of DOS might be responsible for the large magnetization for these clusters. One can explain the increased magnetization by a smearing effect, when d-orbitals become magnetically equivalent, which might be a result of higher cluster symmetry. In fact, the DFT and DFT+U peaks in magnetization in the 55-atom case are often ascribed to symmetry effects.

For a more quantitative picture on the results on the cluster magnetization obtained by three different approximations (DFT, DFT+U and DFT+DMFT) together with the corresponding experimental data we summarize them in Table 3.

Table 3: The DFT, DFT+U, and DFT+DMFT and the experimental results [34,58] for the magnetization (in μ_B) per atom in the Fe clusters.

N	DFT	DFT+U	DFT+DMFT	Experiment
10	3.00	3.00	2.60	4.62±0.4
11	3.17	3.13	2.58	4.80±0.2
12	3.16	3.17	2.92	5.12±0.0
13	3.40	3.40	2.79	2.55±0.3
14	3.30	3.31	3.05	3.40±0.1
15	3.26	3.14	2.77	2.72±0.1
16	3.12	3.13	2.92	2.90±0.05
17	3.06	3.09	2.87	2.86±0.1
18	3.11	3.11	2.92	2.95 ± .00
19	3.05	3.06	2.94	2.92±0.01
27	2.83	3.11	2.98	2.90±0.1
45	2.83	2.97	2.84	2.70±0.1
55	2.73	3.05	3.06	3.10±0.07
75	2.82	3.02	2.99	2.93±0.05
90	2.71	3.02	2.88	2.85 ± 0.05
100	2.67	2.95	2.93	2.95±0.07
110	2.33	2.94	3.33	3.2±0.08
147	1.99	2.93	2.89	2.82±0.1

From Fig. 28 and Table 3 one can find the following general trends in magnetization of different size clusters obtained with the different approximations:

(1) Small clusters (10–19 atoms)

DFT+DMFT give smaller magnetization than in DFT and DFT+U, and the magnetization produced by DFT and DFT+U are very similar. In this small clusters the spin-up (fully-occupied) and spin-down DOS are already have large separation in DFT approximation. In the DFT+U approximation the spin DOS separation increases by very small amount which does not lead to any change of magnetization.

(2) Large clusters (55–147 atoms)

DFT+DMFT results for the magnetization are closer to the experimental data comparing to the DFT results. DFT+U results for magnetization are also pretty similar to the DFT+DMFT ones, except the Fe_{110} case. In this case, DFT+DMFT slightly overestimate the magnetization and the DFT+U give an underestimated result with respect to the experimental data. Similarity of DFT+U and DFT+DMFT results for the 55-147 clusters may be explained by large average bondlength in the clusters (see Fig. 25) that leads to strong electron localization, making the dynamical effects suppressed. This suggests that fluctuation effects are less dramatic for this particular size of particles. For Fe_{110} and Fe_{147} the averaged magnetization obtained from the DFT approximation are much smaller than that the DFT+U, DFT+DMFT and experimental results because as was mentioned above, as it follows from the DFT calculations some of the central atoms are in anti-ferromagnetically ordered with respect to the surface atoms (see Fig. 24).

(3) The ‘intermediate size’ particles (27–45 atoms)

> The DFT+DMFT gives better agreement with experiments compared to DFT and DFT+U, and the values of the magnetization obtained by all three approaches are rather different.

The success of DFT+DMFT approach for reproducing oscillation of magnetization with cluster size suggest that the delicate balance of local repulsion and hopping processes taken into account by DMFT is important for obtaining the correct values of the magnetic moments. It must also be mentioned that simple pictures based on the relation between the magnetization and the bondlength and number of nearest neighbor distributions in the clusters (the Heisenberg exchange and itinerant-(Stoner-) pictures of the ferromagnetism, respectively) have limited application when one tries to deal with understanding of the size-dependence of nanoparticle magnetization. To get a more complete understanding of this complex phenomenon, one need to take into account the local and itinerant effects more accurately, this is done by the DFT+DMFT approach. Indeed, similar to DFT this approach is capable to describe itinerant phenomena (through the hopping and dynamical fluctuation processes) and similar to DFT+U it takes into account the effects of strong local electron-electron interactions, which lead to behavior closer to an atomic type.

It is also important to stress that further experimental work to clarify the geometry of the clusters considered in this work needs to be done. In order to understand how our results are structure-dependent, we used several different configurations for Fe_{11}–Fe_{19} structures in the DFT+U and DFT+DMFT calculations. The results are shown in Fig. 29.

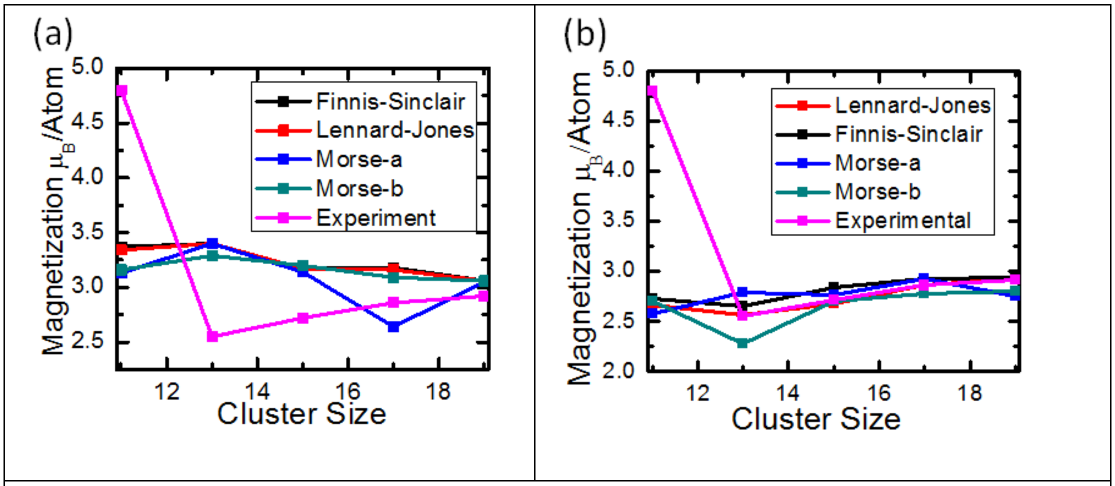

Figure 29: Magnetization per atom versus the cluster size in the case of DFT+U (a), DFT+DMFT (b) calculations for clusters with different configurations. The experimental data[58] are also presented.

In practice all cases (except very small Fe_{11} and Fe_{12} clusters), the DFT+DMFT results are very similar, and much closer to the experimental data as compared to the DFT+U results. These results suggest the reliability of the DFT+DMFT approximation in the case of magnetic nanoclusters.

4.5 Conclusions

In this Chapter, we analyzed importance of the correlation effects in the electronic and magnetic properties of TM nanostructures. We have shown that similar to the bulk systems, correlation effects in nanosystems need to be taken into account beyond DFT or DFT+U. In the case of small Fe and FePt clusters, we found that dynamical correlation effects lead to a significant decrease of the magnetization with respect to DFT+U results. There are two reasons for this: first, the time-dependence of the orbital occupancy taken into account in the DMFT approach leads to a significant decrease of the magnetization relative to “the staggered” DFT+U spins. Second, the level of occupancy of orbitals are changed with respect to the Fermi energy due to the frequency-dependence of the spin-resolved electron self-energy and hence the magnetization. The chemical composition, geometry and local Coulomb repulsion dependencies of the magnetization were also analyzed. In particular, we found that similar to the bulk, to get the same nanoparticle magnetization from DFT+U and DFT+DMFT one needs to use a larger value of U in the latter. Stronger electronic screening effects in DMFT might be one of the reasons for this. We get same level of agreement with the experimental data with DFT+DMFT as in the case of DFT+U.

We have extended DFT+DMFT formalism to study electronic and magnetic properties of larger nanoparticles and applied the approach to study magnetic properties of Fe nanoparticles of size up to 147 atoms using our own code with the generalized IPT impurity solver. The DFT+DMFT results for the magnetic moments of 10-147-atom iron nanoparticles shows that in most cases the inclusion of dynamical correlations results is in overall better agreement with experiment[34,58] comparing to other approaches. This is to our knowledge the first demonstration that DFT+DMFT applied to experimentally realizable magnetic nanoparticles can produce accurate results. The methodology should have multiple applications as it can be readily applied to larger (several-hundred atom). The computational speed of the developed code is such that the total computational time of the DFT+DMFT calculations is comparable to the corresponding time for the DFT calculations.

After successful application of the nanoDFT+DMFT approach to clusters and nanoparticles, we extended the formalism on the case of films – systems with mixed geometry (infinite/periodic in two and finite in one direction). In the next Chapter, we present the results of the nanoDFT+DMFT studies of the electronic and magnetic properties of a Fe_2O_3(001) film.

CHAPTER 5 APPLICATION OF DFT+DMFT TO Fe_2O_3 (001) FILMS

There are several types of iron oxides (FeO, Fe_3O_4, α-Fe_2O_3, β-Fe_2O_3 etc.) in nature, which are used in different applications, such as catalysis, electrochemistry, magnetization, biomedical science, ceramics and environmental applications.[146-151]. Hematite, for examples, is considered as an efficient support for catalytic applications, corrosion and lubrication.[59,60] It is also used as a natural pigment in the manufacture of red, brown, and black colors and their admixtures,[152] in magnetic devices and for suppression of greenhouse gases by oxidizing CO to form CO_2 [153]. To understand properties of the system and to control these and predict other applications one needs a very detailed knowledge about the structural and electronic properties of bulk and surfaces of Fe_2O_3. There have thus been several theoretical studies on these systems using DFT and DFT+U methods in recent years.[71,154-156]

The case of a film is more complex, since the hematite (001) surface can have five different types of termination: two Fe-terminated and three O-terminated surfaces.[63] Moreover, Wang *et al*.[64] on the basis of DFT and STM studies showed that two different surface terminations can coexist on single crystalline $\propto -Fe_2O_3$ (001) films in high (10^{-3} mbar) oxygen pressure. By interpreting the STM images within resonant tunneling theory Eggleston *et al.* concluded that the O-terminated surface must be the lowest-energy surface under oxygen pressure conditions.[65] A possibility of the surface reconstruction of Fe_2O_3 was analyzed in Ref. [157], where it was found that the surface can consist of coexisting islands of Fe and FeO.

The first principle DFT studies by Kiejna *et al*.[66] suggest that a Fe-terminated structure in the form of Fe-O3-Fe- is more stable than the other terminations. In another recent DFT+U study these authors demonstrated a possibility of coexistence of the Fe and O termination in one surface super-lattice.[67] All the above results suggest that one needs more studies to come to a definite conclusion for the structure of the lowest-energy hematite surface. In this work we analyze the case of (001) Fe-terminated surface, as the most often studied system.

It is known that DFT with simple XC potentials cannot be used to study hematite systems, because this oxides system is strongly correlated.[158] Indeed, the spin LDA or GGA fail to reproduce the correct ground state properties of many TM oxides, including high magnetic moments of Fe atoms and the spectral gap in bulk hematite.[68] The DFT+U improve the value of the magnetization in bulk Fe_2O_3, but cannot explain the MIT (with volume/temperature change) in this system.[69-71] The LDA+DMFT approach was used to describe the MIT, accompanied by the high- to low-spin transition, and succeeded in this.[72,73] Thus, to obtain the most complete understanding of physics of hematite films one needs to use a DFT+DMFT approach.

5.1 Computational Details

The optimized initial structures for bulk and surface Fe_2O_3 were provided by Adam Kiejna group (U. Wroclaw, Poland).[66,67] To calculate the magnetic moments, we performed self-consistent force (SCF) calculation by spin-polarized DFT as implemented in the VASP package [128]. The XC potential was approximated by the

GGA functional by Vosko *et al.* [129] The DFT+U calculations were performed by using the method implemented in VASP by Dudarev *et al*[159] with values of U=3 and 6 eV for the d-orbitals of the Fe atoms. The DMFT part of the calculations was performed by using our nanoDFT+DMFT code with the IPT impurity solver.

5.2 Bulk Fe_2O_3

To test the validity of the DMFT approximation, we performed simulations bulk Fe_2O_3 for which a large amount of experimental data available. Bulk hematite is thermodynamically the most stable structure among all iron oxides and is the most common form of crystalline iron oxide.[160] The crystal structure of hematite is of the corundum type with space group $R3c$ (each hexagonal unit cell contain six formula units). Fig. 30 shows two unit cell of bulk Fe_2O_3. There are two sub-layer of Fe atoms which are spaced approximately by one-third and two-thirds the distance between oxygen layers. The oxygen anions form a hexagonal close-packed sub-lattice with two-thirds of the total number of six-fold coordinated sites occupied by ferric cations. Fe_2O_3 has hexagonal unit cell with lattice parameters $a = 5.034Å$, $c = 13.75Å$.[161] The top view and side view of a unit cell of bulk Fe_2O_3 is shown in the Fig. 30. We note that there are two types of pairs of Fe atoms, which are characterized by a short Fe-Fe distance (type A) and by a larger distance (type B) along the (001) direction. Hematite exhibits different magnetic properties at different temperatures. In particular, it exhibits antiferromagnetism below the Neel temperature of 950K[162] and weak ferrimagnetism below 260K.[163] The antiferromagnetic ground state of bulk hematite was found in

DFT study by Nelson *et al.* [164] They found that strong hybridization of the oxygen and iron states are responsible for the antiferromagnetism. Thus, the antiferromagnetism can be obtained already on the DFT level, which makes our analysis more consistent, where we consider DFT results as the input for DMFT calculations.

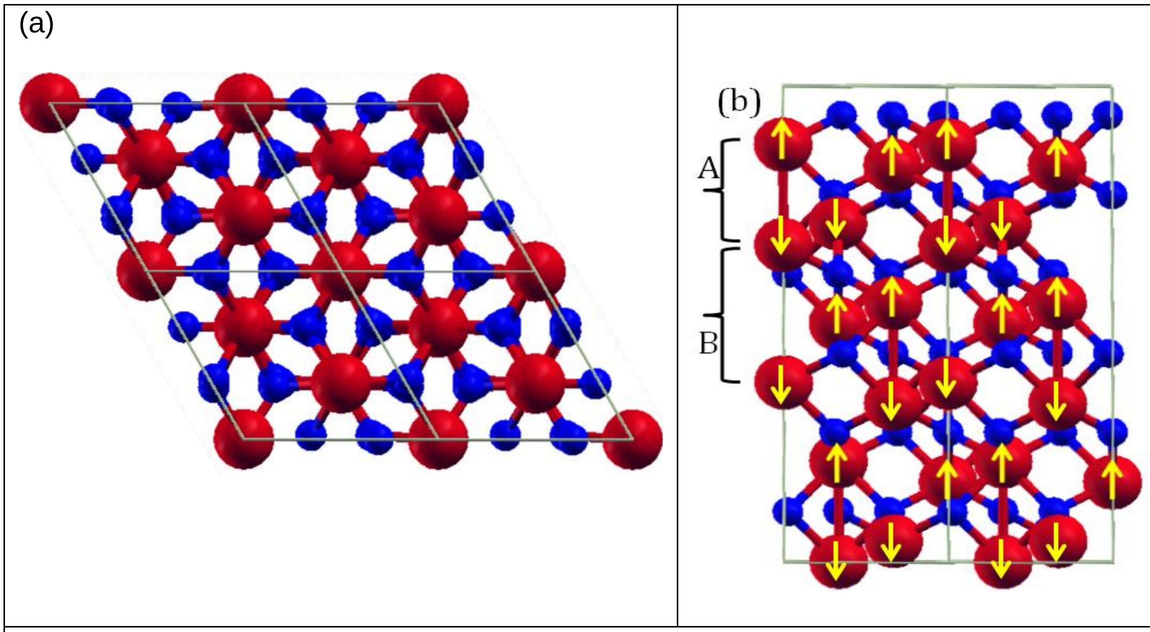

Figure 30: Schematic illustration of the (a) top view of 2x2 unit cell and (b) side view of a 2x2 unit cell of bulk Fe_2O_3. Arrows indicate directions of magnetization of individual Fe atoms (shown in red). Oxygen atoms are shown in blue. There are two sorts of pairs of Fe atoms along the (001) direction, one (denoted as type A) with a short and the other (type B) with a larger Fe-Fe distance.

Magnetic moments of Fe atoms in the unit cell of hematite can have three different types of antiferromagnetic arrangements: (i) AF++-- (++-- state means that Fe atoms belonging to short distance pairs (distance type A), have opposite magnetic moment, while Fe atoms belonging larger distance pairs (distance type B) have equal magnetic moments. Fig. 30(b)), (ii) AF+-+- and (iii) AF+--+. The magnetic structure (AF++--) shown in Fig. 30 corresponds to the lowest-energy spin arrangement with magnetic moments 3.4 μ_B obtained by GGA.[71] Other higher energy magnetic orderings, together with the summary on the lattice parameters, magnetic moment and energy differences is presented in Table 4.

Table 4: Theoretical results for the structural parameters and magnetic moments of bulk Fe_2O_3 with different magnetic configurations along with experimental data. (NM means the non-magnetic configuration)

Magnetic State	Functional	Energy (meV)	Magnetic moment μ_B	c/a ratio	Fe-Fe(A) (in Å)	Fe-Fe(B) (in Å)
AF++--	GGA[71]	0	3.44	2.77	2.941	4.006
	LSDA[165]	0	3.72			
	HF[166]	0	4.74	2.70	2.877	4.033
	This study GGA		3.47	2.73	2.915	3.981
AF +-+-	GGA[71]	211	3.38	2.76	2.959	3.958
	LSDA[165]	190	2.80			
AF+--+	GGA[71]	224	3.45	2.69	2.803	4.000
	LSDA[165]	204	3.74			
FM++++	GGA[71]	388	2.60	2.85	2.689	4.380
	LSDA[165]	489	3.73			
	HF[166]	37				
NM	GGA[71]	680		2.83	2.761	4.280
Expt. (Ref. [167])			4.12	2.73	2.896	3.977

We also performed DFT+U calculations and found that DFT+U can give the values of the magnetic moments and of the bandgap, in a better agreement with experiments than DFT results. The atomic-projected DOS for the spin up and down states for different atoms is plotted in Fig. 31.

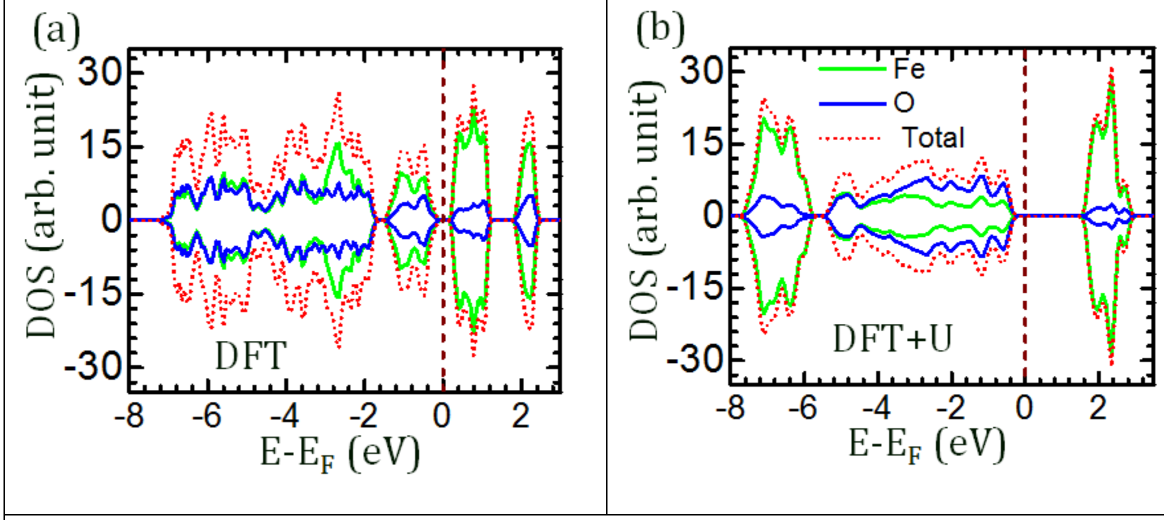

Figure 31: DOS for bulk Fe_2O_3 projected on Fe (green line), O(blue line) and total (red dotted line) in (a) DFT and (b) DFT+U (U=5 eV) approximation.

The bandgap obtained from the DFT approach is 0.35 eV and the magnetic moment is 3.47 μ_B, which is not in agreement with the experimental bandgap (1.9-2.2 eV [168] and 4.12 μ_B [169],correspondingly). DFT also gives incorrect position of Fe 3d-bands with respect to the O 2p-bands, which give a very small energy bandgap. The bandgap under DFT+U study is 1.82 eV and the magnetic moment is 4.14 μ_B in good agreement with experiments. As it was mentioned above, though DFT+U corrects the DFT bandgap for bulk Fe_2O_3 it fails to capture the MIT in the system due an overestimation of local Coulomb repulsion effects. In studies by other authors, it was shown that the bandgap in Fe_2O_3 increases almost linearly with the values of U [164] and that U=5 eV gives the experimental value for the gap. Parameterization of U values sometimes creates confusion on what values of U to choose for a system. In this study with DFT+DMFT approach, we found that at U=6 eV the exact bandgap is reproduced for the bulk Fe_2O_3. In this work we do not consider the problem of the MIT, focusing on the insulating phase. Our results for the DOS of the bulk Fe_2O_3 obtained within DFT, DFT+U and DFT+DMFT is shown in Fig. 32.

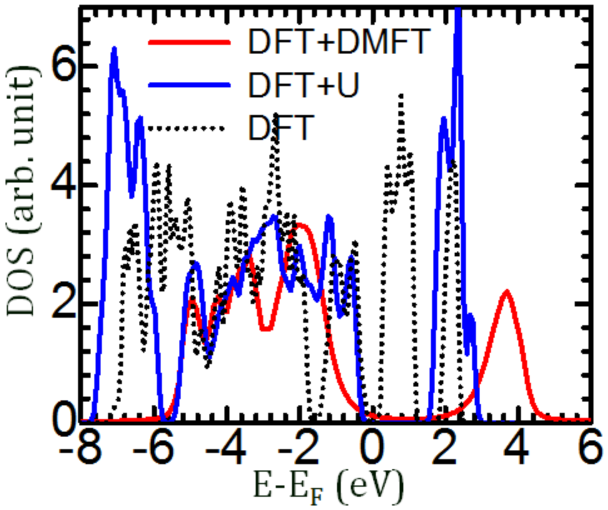

Figure 32: DOS of bulk Fe_2O_3 obtained with DFT (black dotted line), DFT+U (blue line) and DFT+DMFT (red line).

As it follows from Fig. 32 that the band-gap of bulk Fe_2O_3 in DFT+DMFT approach (2.0 eV) is in good agreement with the experimental bandgap (1.9-2.2 eV [168]). The value of bandgap and magnetic moment of bulk Fe_2O_3 in DFT, DFT+U and DFT+DMFT along with experimental data are presented in Table 5.

Table 5: Magnetic moment and bandgap of bulk Fe_2O_3 in three (DFT, DFT+U and DFT+DMFT) approaches along with experimental data.

	Magnetic moment (in µB)	Bandgap (in eV)
DFT	3.47	0.35
DFT+U	4.14	1.82
DFT+DMFT	3.98	2.0
Expt.	4.12[169]	1.9-2.2[168]

As we can see from Table 5 that DFT+DMFT with IPT solver can reproduces experimental data for bulk the bulk Fe_2O_3, this suggest that the IPT is a good approximation for the film of Fe_2O_3 as well.

5.3 Fe_2O_3 (001) film

The unit cell of the Fe_2O_3 (001) film we studied is shown in Fig.33. The interatomic distances for this structure have the following values. The surface Fe-O bond length perpendicular to the surface plane is 1.82 Å, shorter than the normal bond length in the bulk (1.940 Å), and the Fe-O distances vary from 1.82 to 2.14 Å. The short Fe-Fe distance is 2.89 Å and the bond from the top O to the top Fe located at the surface is 1.94 Å, while the long Fe-Fe distance is 3.79 Å and O-O has decreased from 2.92 Å in the bulk to 2.88 Å in the surface. These numbers are in a good agreement with results of other theoretical studies (see, for example, Ref. [164] and references therein).

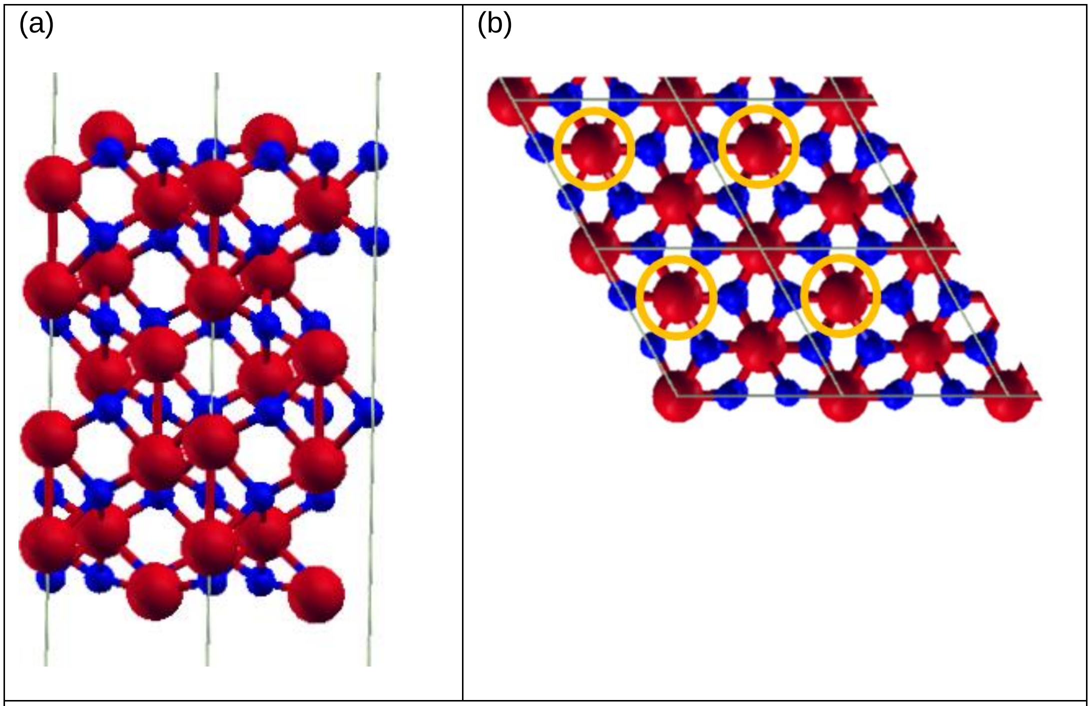

Figure 33: Schematics of a 2x2 unit cell of iron terminated Fe_2O_3 (001) surface we used in our studies: (a) side view and (b) top view. Iron and oxygen atoms and shown in red and blue colors, correspondingly. The orange circles in (b) indicate the top layer atoms.

Similar to the bulk, Fe_2O_3 (001) surface is also antiferromagnetically ordered.[164] We have used the same antiferromagnetic order of Fe atoms in the unit cell as in the bulk case. The magnetic moment of the bulk Fe atoms in the film is found to be 3.56 μ_B and for the surface atom this value is 3.38 μ_B within the DFT approximation. The DFT+U calculations give the values 3.97μ_B and 3.91μ_B, respectively. The surface atom has slightly reduced magnetic moment compared to the bulk atoms in both DFT and DFT+U approximation. This can be explained by the difference in coordination numbers between surface and bulk atoms, which leads to different orbital hybridization for these Fe-atoms (3d-) and surrounding O (2p-) electrons, which in turn affects the magnetic moments.

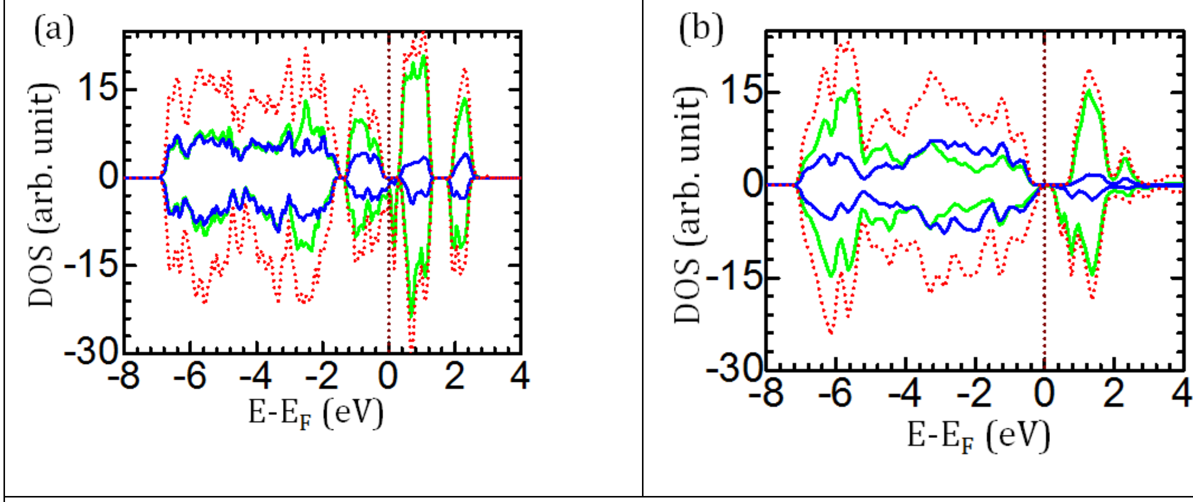

Figure 34: DFT (a) and DFT+U (b) results for the total spin DOS for different atoms in the Fe_2O_3 (001) film (at U=6 eV). Results for Fe and O atoms are shown in green and blue colors, and the total spin DOS is shown by red dotted line.

The atomic spin DOS of the hematite film obtained with DFT and DFT+U approaches are shown in Fig. 34 (d-orbitals for Fe and p-orbitals for O atoms). Similar to the bulk case, our calculations show that DFT gives a small bandgap and the bandgap increased to 1.0 eV at U=3 eV and to 1.7eV at U=6 eV (shown in the Fig. 34). There is large contribution to the total DOS near the Fermi energy from the 3d-electrons of the Fe atoms, suggesting that the correlation effects are important in the film as well.

The DFT, DFT+U and DFT+DMFT results for the DOS of the film are shown in Fig. 35. As it follows form the last two figures, DFT+U increases the DFT bandgap, similar to the bulk Fe_2O_3.[164]

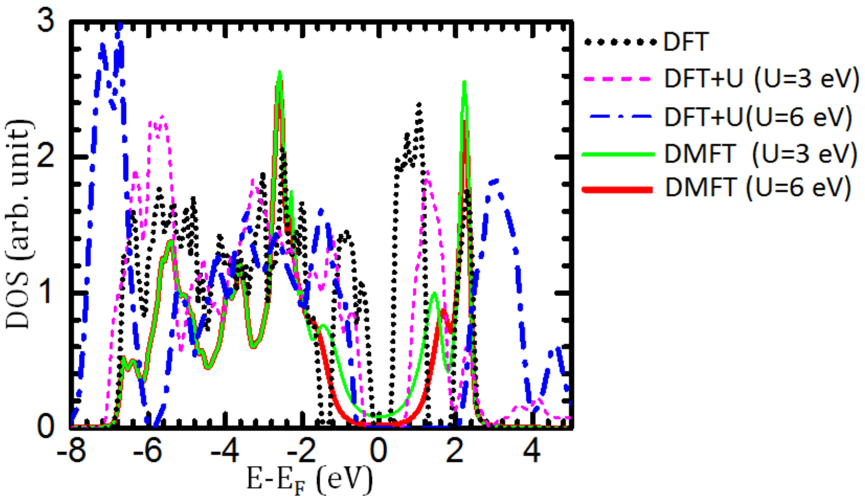

Figure 35: Total DOS of the Fe_2O_3 (001) film obtained with DFT (black dotted line), DFT+U (U=3 eV), DFT+U (U=6 eV) (blue broken line) (pink dashed line) and DMFT with U=3 eV (solid green line) and U=6 eV (solid red line).

As it follows from Fig. 35, there is no bandgap in the DFT+DMFT DOS at U= 3eV, while U=6 eV gives 1.7eV bandgap. As we mentioned above, similar result was found by Kunes *et al, in the case of bulk* Fe_2O_3 [73]

To study the properties of the hematite surface in more detail, we analyzed the projected DOS for each d-orbital of the surface and bulk Fe atoms obtained with the DFT+DMFT approach. As it follows from Fig. 36, surface atoms have an extra satellite peak for spin-down d_{xz}- and d_{yz}-electrons at 2 eV of energy (indicating by an arrow in Fig. 36(a)).

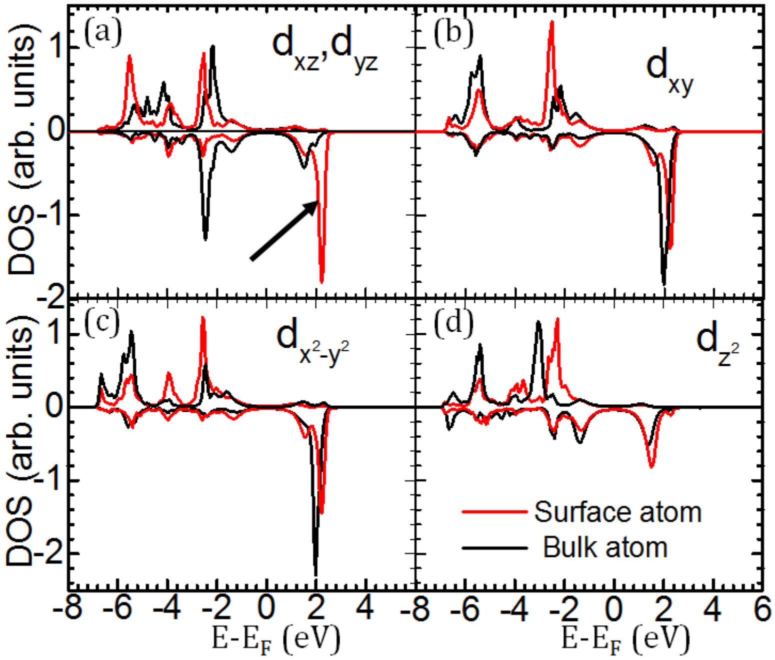

Figure 36 The spin- and orbital-projected DOS for the Fe bulk (black) and surface (red) atoms in Fe_2O_3 (001) film at U=6eV.

This satellite peak is absent for the bulk atom and also for the surface atom in DFT+U case. In addition to possible optical applications (~2eV excitations in the visible range), this state may also affect the magnetic properties of the film. Namely, it can lead to a significant change of the surface spin moments (through larger unoccupied densities of the spin-down states on the surface), which might explain smaller magnetization of surface atoms in comparison with the bulk ones (3.94 μ_B vs 3.98 μ_B). Also, due to different spin and orbital moments of the surface and bulk atoms, one can expect different MCA for these atoms. However, this question requires additional studies. Table 6 showed the value of magnetic moment (of bulk and surface atoms) and bandgap of Fe_2O_3 film in DFT, DFT+U and DFT+DMFT approaches.

Table 6: Magnetic moments and bandgap of Fe_2O_3 film system in DFT, DFT+U and DFT+DMFT approaches

Approach	Magnetic moment (in μ_B)		Bandgap (in eV)
	Bulk atom	Surface atom	
DFT	3.56	3.38	0.3
DFT+U(U=3eV)	3.90	3.85	1.0
DFT+U(U=6eV)	3.97	3.91	1.7
DFT+DMFT(U=3eV)	3.93	3.89	0.0
DFT+DMFT(U=6eV)	3.98	3.94	1.6

It is clear from Table 6 that surface Fe atom have less magnetic moments than bulk Fe atom in all three approximations, However, the absolute values of the surface atoms magnetic moments are smaller in DFT+DMFT

5.4 Conclusions

Detail investigation of electronic properties of both the bulk and (001) film of Fe_2O_3 was performed under DFT, DFT+U and DFT+DMFT approximation. Similar to bulk case, we have found a gap in the spectrum of the film. We have performed a detailed study of the surface states of the Fe atoms, and found a large satellite peak around 2eV above the Fermi level. These states lead to a difference of the magnetic moments of the surface and bulk atoms of the film, and may affect other properties of the system, like the magnetic anisotropy. More detailed experimental studies of the Fe_2O_3 films may help in better understanding of these and other magnetic properties of the system, including the role of correlation effects in hematite with different geometries.

After presenting the results on the magnetic moments of nanoparticles and films, in the next Chapter we analyze another important magnetic property of nanoparticles - magneto-crystalline anisotropy on the example of FePt systems.

CHAPTER 6 AB-INITIO STUDY OF MAGNETOCRYSTALINE ANISOTROPY OF FePt NANOSYSTEMS

It is known for a long time, that even in absence of the external magnetic field the magnetic moments of the particles tends to align themselves to the direction which minimizes the magneto-static energy of the system. This direction is called the direction of easy magnetization. The magnetic anisotropy shows the directional dependence of internal energy of magnetic material under spontaneous magnetization. Rotation of magnetization vector from the direction of easy magnetization is possible only by applied field. In other words, this magnetic energy is direction dependent and is called magnetic anisotropic energy (MAE) (see Fig. 12). Since this energy have the same symmetry as the crystal axis, MAE is also called magnetocrystaline anisotropy (MCA). MCA is an intrinsic property of the system, related to the atomic-scale interactions, and basically defined by interaction of the magnetic moments with the crystal field. There is another type of anisotropy, called shape anisotropy, which can be related to the energy of the sample in its own demagnetizing field. In this thesis we study only MCA.

The origin of MCA comes from the Spin-Orbit Coupling (SOC) in the system. The electric field from neighboring atoms restricts the orbital motion of electrons in the solid. Therefore, the electrons cannot be freely oriented by a magnetic field in the solid. The spin and orbital moments of the electron also interact strongly with each other. As a result, when an external magnetic field orients the spin of one electron, it immediately affects its orbital moment, which in its turn interacts with orbital moments of neighboring atoms, and then the spins of neighboring atoms interact with their orbital moments and so on.

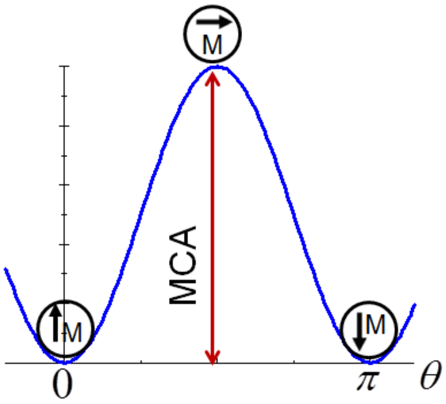

Figure 37: Schematic representation of the MCA, which is the difference between magnetic energy in two different directions.

In this way the directional character of orbits communicate with spins: the electron spin is coupled with the orbital moment which in turn is coupled with the crystal field. There are many different methods to calculate MCA of a system. For instance, Solovyev *et al*.[78] used scalar relativistic Green's function technique in real space, and showed that in lowest order perturbation theory with respect to the spin-orbit interaction (SOI) the MCA can be expressed in simplified form. Bruno[170] formulated tight-binding approach to calculate the MCA with taking SOC into account. In this thesis, we study MCA by two different approaches; the direct approach and the torque approach [171,172]. We describe these approaches in more detail below.

6.1 The direct and torque spin DFT approaches

6.1.1 The direct approach

In the direct approach the value of MCA is determined by comparing the total energy of the system for two different orientation of magnetization (Fig. 12). For 3d TM elements with weak SOC, one can apply the "force theorem"[173] and calculate MCA by comparing band energy between two magnetic orientation, as

$$MCA = E(\uparrow) - E(\rightarrow) = \sum_{occ'} \varepsilon_i(\uparrow) - \sum_{occ''} \varepsilon_i(\rightarrow) \qquad (6.1)$$

where, ε_i is the band energy of the i^{th} state and the arrow in the parentheses denote the direction of magnetization it is usually the direction parallel and perpendicular to the surface of a film, and for nanoparticles it is parallel to xy-plane and along z-axis. The band energies in Equation (6.1) can be calculated by using spin-polarized DFT with SOC taken into account, since MCA is a ground-state property of the system. The magnetization can set towards two specific directions by using non-collinearity of spin arrangement in the system. The sum in equation (6.1) gives usually a large number (on the order of hundreds of eV), whereas the MCA is on the order of few meV, i.e. MCA is a small number coming from the difference of two large numbers and one need to be very careful about the convergence of the calculation when determining the Khon-Sham energy of the system. In fact, one needs to use very fine K-point mesh in the reciprocal space to get the integration accurate. A very small convergence criterion of energy is also required in the SCF cycle, which makes the calculations more computationally demanding. The direct method may give contradictory results if one does not use sufficient number of integration points. For example, Gay and Richter[174] predicted that in the case of monolayer Fe the easy axis to be perpendicular to the plane with the anisotropy energy of -0.4 meV/atom. On the other hand, Karas et at.[175] found easy axis along the plane of the Fe layer and the value of anisotropy to be 3.4 meV/atom.

6.1.2 The Torque Method

Wang *et al*.[171] proposed a new approach of calculating MCA for systems having uniaxial symmetry, which is independent of the validity of force theorem and which does not require the magnetostatic energy of a system to be calculated in two different directions with very high accuracy.

To describe the method let us begin with the expression for the total energy of a uniaxial system, which can be written as:

$$E(\theta) = E_0 + K_2 sin^2(\theta) + K_4 sin^4(\theta), \tag{6.2}$$

where θ is the angle between the direction of magnetization and surface normal, K_2 and K_4 are anisotropy constant of the system. The torque $T(\theta)$ of the system is defined as the angular derivatives of the total energy:

$$T(\theta) \equiv \frac{dE(\theta)}{d\theta} = K_2 \sin(2\theta) + 2K_4 \sin(2\theta)\, sin^2(\theta). \tag{6.3}$$

Since the MCA is by definition,

$$MCA = E(\theta = 90^{\circ}) - E(\theta = 0^{\circ})$$

$$= K_2 + K_4 = T(\theta = 45^{\circ}), \tag{6.4}$$

one can obtain it from the result for the torque of a system at an angle of 45° between surface normal and the direction of magnetization.

The next question which one may ask is how to calculate the torque in DFT? According to spin DFT theory with SOC (separating the Kohn-Sham band energy and double counting terms) the total energy is

$$E[n_{\sigma}(\theta);\theta] = \sum_{occ} \epsilon[n_{\sigma}(\theta);\theta] + E'[n_{\sigma}(\theta)], \tag{6.5}$$

where E' is the double counting term and the total energy depends on θ both through the SOC part and angular part of the Hamiltonian. The energy deviation can be written as:

$$E[n_{\sigma}(\theta+\delta\theta);\theta+\delta\theta] - E[n_{\sigma}(\theta);\theta] = \{E[n_{\sigma}(\theta+\delta\theta);\theta+\delta\theta] - E[n_{\sigma}(\theta);\theta+\delta\theta]\}$$

$$+\{E[n_{\sigma}(\theta);\theta+\delta\theta] - E[n_{\sigma}(\theta);\theta]\} = \mathcal{O}[\delta\theta^2] + \sum_{occ} \epsilon[n_{\sigma}(\theta);\theta+\delta\theta] - \sum_{occ} \epsilon[n_{\sigma}(\theta);\theta]$$

$$= \frac{1}{\Omega_{\mathrm{BZ}}}\int \delta\epsilon(\mathrm{k})d\mathrm{k} + \frac{1}{\Omega_{\mathrm{BZ}}}\int \epsilon(\mathrm{k})d\mathrm{k} = \frac{1}{\Omega_{\mathrm{BZ}}}\int \delta\epsilon(\mathrm{k})d\mathrm{k} + \frac{\epsilon_F}{\Omega_{\mathrm{BZ}}}\int d\mathrm{k} = \frac{1}{\Omega_{\mathrm{BZ}}}\int \delta\epsilon(\mathrm{k})d\mathrm{k}, \tag{6.6}$$

where Ω_{BZ} is the volume of the Brillouin zone. Now having equation (6.6) in mind, we can write torque as,

$$T(\theta) = \sum_{occ} \left\langle \psi_{i,k}^{SO} \middle| \frac{\partial H_{SO}}{\partial\theta} \middle| \psi_{i,k}^{SO} \right\rangle, \quad H_{SO} = \sum_i \xi(r_i)\hat{\boldsymbol{l}}_{\boldsymbol{i}}.\hat{\boldsymbol{s}}_{\boldsymbol{i}} \tag{6.7}$$

where we have used the Feynman-Hellman theorem. The product of angular momentum $\hat{\boldsymbol{l}}_{\boldsymbol{i}} = -i\mathbf{r}_{\mathbf{i}} \times \nabla$ and spin operators in polar coordinates can be written as:

$$\hat{\boldsymbol{l}}_{\boldsymbol{i}}.\hat{\boldsymbol{s}}_{\boldsymbol{i}} = s_n\left(l_z cos\theta + \frac{1}{2}l_+ e^{-i\varphi} sin\theta + \frac{1}{2}l_- e^{i\varphi} sin\theta\right)$$

$$+\frac{1}{2}s_+\left(-l_z sin\theta - l_+ e^{-i\varphi} sin^2(\theta/2) + l_- e^{i\varphi} cos^2(\theta/2)\right) +$$

$$\frac{1}{2}s_-\left(-l_z sin\theta + l_+ e^{-i\varphi} cos^2(\theta/2) - l_- e^{i\varphi} sin^2(\theta/2)\right). \quad (6.8)$$

now by taking derivative of the last equation with respect to θ and substituting it into equation (6.7), one can easily find the torque of the system. Wang *et al*.[171] showed that the calculation in the torque approach does not depends on the validity of MCA force theorem[173], though if it is applicable it can makes the calculation much simpler. The advantage of torque method over the direct approach is that the calculations are very fast, because one does not need to do the self-consistent calculations that include the SOC. Also, the case of torque approach one does not need very high precision for the convergence of the SCF calculations.

We considered the cases of L1$_0$ FePt bulk alloy, FePt dimer and L1$_0$ FePt nanoparticles with different sizes and compositions. The chemically ordered L1$_0$ FePt structure can be obtained by annealing the fcc structure of FePt alloy or by depositing it on substrate above the L1$_0$ ordering temperature[176,177]. This structure has alternating Fe and Pt planes along (001) direction, which is also the easy axis of magnetization. This type of structure does not have the cubic symmetry as one of the symmetries of the system. The MCA in this FePt structures mainly comes from the contribution of the Pt ($5d$

element) atoms with a large SOC. On the other hand, the Fe ($3d$ element) atoms provide the exchange splitting of the Pt sub-lattice.[77,78,178] More precisely, the hybridization of Fe orbitals cause spin polarization of Pt atoms and as a results enhance the MCA due to strong SOC in the Pt atoms.

At high temperatures, an fcc solid solution of Fe-Pt is observed in A1 phase. Below 1573K alloys with close number of Fe and Pt atoms shows disorder-order transition with formed $L1_0$ ordered phase. The condition to create $L1_0$ phase is 35-55% of Pt concentration at temperatures 973k-1573k.[9] The $L1_0$ phase can also be produced by chemical synthesis of nanoparticles.[10] Alternating monolayer deposition of Fe and Pt can reduce the onset temperature of $L1_0$ phase.[179] Another way to obtain $L1_0$ phase experimentally is by annealing alternating multi-layers of Fe and Pt.[9]

To support theoretical studies, some experimental measurements by using X-ray Magnetic Circular Dichroism Spectroscopy (XMCD), X-ray Absorption spectra (XAS) were used to confirm the enhancement of MCA of different free and supported clusters.[137,180,181]

There are several available theoretical results on MCA of FePt nanoparticles. In particular, Cyrille *et al*.[182] studied a size and shape dependent magnetic properties of $L1_0$ FePt clusters (with central plane filled with Fe atoms) by a tight binding approach. Błonski and Hafner[183] performed *ab initio* DFT calculations of the magnetic anisotropy of supported nanostructures. Fernandez-Seivane and Ferrer[55] studied impact of the magnetic anisotropy on the geometry and magnetic ordering in small (up to 7 atom-) clusters.

Here in this thesis we perform a theoretical investigation of MCA of much larger $L1_0$ FePt clusters of size 30, 38, 71, 79, 114, 132, 140, 230, 386 and 484 atoms and also the pure Fe and Pt clusters of same size. The clusters studied have 1(2), 2(3), 3(4) and 4(5) layers of Fe (Pt) atoms. The electronic structural and magnetic properties (including the orbital moments) of each atom in each of these configurations are also examined. This allows us to get a deeper understanding of the magnetic properties of FePt nanoparticles and about the suitable size for practical applications.

6.2 Computational Details

Ab initio spin-polarized DFT approach implemented in the VASP code[128] is used for the structural relaxation of the nanoparticles. For the ionic relaxation, we employed the conjugate gradient algorithm and the electron-ion interaction was described by the projector augmented-wave (PAW)[130] formalism. The spin-polarized GGA with the PW91 functional[88] is used to describe the electronic XC effect as the spin interpolation proposed by Vosko *et al.*[129] . We used the relativistic version PW91 in the non-collinear mode of VASP [184,185] since it is essential for the calculation with SOC.

The bulk FePt $L1_0$ structure was constructed by replacing every alternating layer of fcc Fe with Pt atoms in (001) direction. This types of structure can be explained in terms of a pseudo-cell inside the primitive cell, as indicated in the Fig. 38 the lattice parameter of the primitive cell *a* is related to the parameter of pseudo-cell a^* by $a = a^*\sqrt{2}$), This L1_0 ordering induces a contraction along the (001) direction of the lattice, which reduces the ratio $c^*/_{a^*}$, from the fcc value $\sqrt{2} \approx 1.41$ to 1.363.

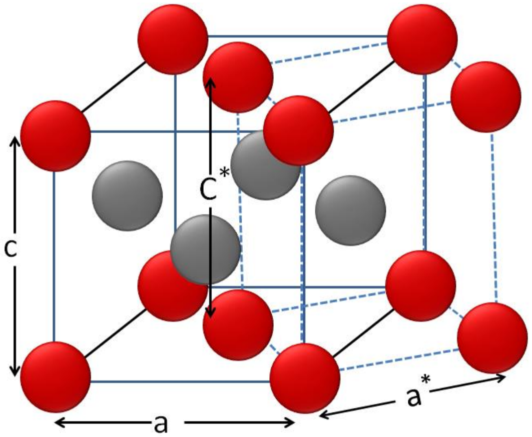

Figure 38. The crystal structure of bulk FePt L1_0 (Fe atoms in red and Pt in gray). Different parameters are related as: $\boldsymbol{c} = \boldsymbol{c}^*$ and $\boldsymbol{a} = \boldsymbol{a}^*\sqrt{\boldsymbol{2}}$, where $\boldsymbol{c}^*$ and $\boldsymbol{a}^*$ are the lattice parameters of the primitive cell and c and a are the corresponding parameters of the pseudo-cell (see the text for their values)

A chemical re-ordering in the unit cell is occurs due to the lattice distortion. For the initial structure lattice parameters, we used the experimental values for bulk powder a^*=2.72Å and $c^*/_{a^*} = 1.36$.[186] (a^*=2.72Å and $c^*/_{a^*} = 1.36$), and then relaxed the structure using the DFT approach described above.

Simulations in the cases of dimer and nanoparticles were performed by putting them inside a cubic simulation box. Size of the simulation box is chosen in such way that the distance between cluster and its periodic images is at least 12Å in all three directions to minimize the interaction between the periodic images. The calculations were performed by using only one (Γ) point in the Brillouin zone. The energy cutoff was chosen to be 450eV and we allowed the ions to relax until the force convergence reached 0.01 eV/Å. The initial geometry of each size of the cluster was obtained by cutting the relaxed bulk FePt L1_0 structure. The MCA of the relaxed FePt L1_0 nanoparticles were calculated by using the direct approach and also by the torque method [171,172] as discussed in the previous Section.

6.3 Magnetic anisotropy of the bulk FePt system

We have obtained very close values of lattice parameters for the bulk FePt L1_0 system to the reported in experiments (a^*=2.72Å and $c^*/a^* = 1.36$): the in-plane parameter a^*=2.74Å, and the ratio of parameters $c^*/a^* = 1.37$. The magnetic moment values are also in a good agreement with experimental numbers for Fe ($2.90\ \mu_B$) and (Pt (0.34 μ_B).[186] Namely, we have obtained the following values for the magnetization: $2.85\mu_B$ for the Fe atoms and $0.36\mu_B$ for the Pt atoms. Though bulk Pt is nonmagnetic, as it follows from our calculations it has a finite magnetic moment in the FePt alloy; also the magnetic moment of Fe atoms in FePt is much larger than in bulk Fe. One can explain this enhancement by the hybridization between the Fe- and Pt-atom orbitals. As can be seen in Fig. 39, the hybridization causes a broadening of the d-bands, which results in a shift of the minority spin DOS across the Fermi level. This shift leads to a finite magnetization of the Pt atoms and large value of the magnetization of Fe atoms.

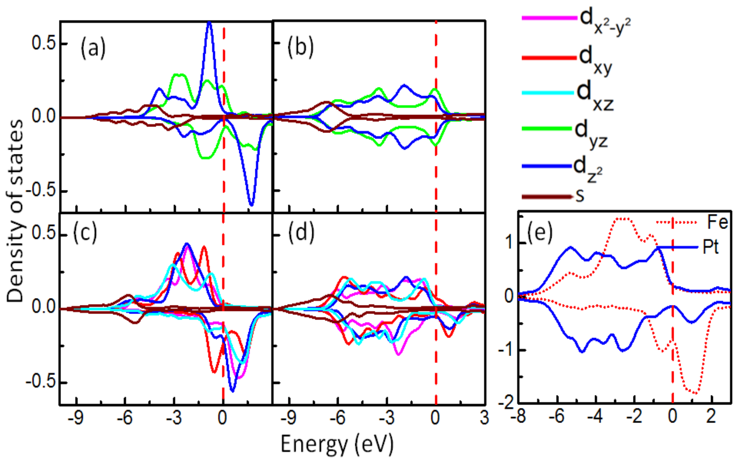

Figure 39: Spin- and orbital-projected DOS for different cases: (a) bulk Fe, (b) bulk Pt, (c) Fe atom in the L1_0 FePt and (d) Pt atom in L1_0 FePt.(e) Spin-projected DOS for bulk L1_0 FePt.

The density of states (DOS) of bulk L1_0 FePt is plotted in Fig. 39, where we also present the projected DOS for the Fe and Pt atoms, which is similar to the one reported in theoretical studies by Barreteau *et al*. [182] Our direct DFT calculations give MCA to be 2.22meV per FePt pair, in agreement with experimental data.[187] This result gives us a confidence that our results in the nanocase are reliable as well. We attribute the large MCA to the large SOC of Pt atoms and to the increase in orbital moment owing to the strong hybridization of their 5*d* orbitals with the 3*d* orbitals of Fe. The hybridization breaks the symmetry of the system in the two perpendicular directions, which results also in different values of the free energy in these directions.[77] It is important to mention that it was reported earlier that the anisotropy in the disorder phase of bulk FePt is order of magnitude smaller than that in the $L1_0$ ordered phase.[9] Thus, the $L1_0$ structure is important for the high MCA.

6.4 Magnetic anisotropy of the Fe, Pt and FePt dimers

To gain more insight into the nature of possible MCA in the nanoparticles, we also considered the case of pure Fe, pure Pt, and FePt dimers. For the latter, we obtained a dimer bondlength of 2.184Å without SOC taken into account, and 2.172 Å with SOC. Therefore, we conclude that SOC does not play an important role in determining the geometry of this system, in agreement with the results of Ref. [36]. Fe_2 turns out to exhibit very small anisotropy owing to the relatively small SOC of the Fe atom (81.6 meV) and the SOC of the Pt atom is nearly 7 times larger (544 meV)[188], and in Pt_2 the spin and orbital momenta each differ in the two directions (along the axis of the dimer and perpendicular to it), leading to the MCA of Pt_2 larger than that of FePt and Fe_2 dimers. The high SOC of Pt atom and relatively large *orbital* moment in Pt_2 together account for the fact that the MCA of the platinum dimer greatly exceeds those of the other two. The MCA of the mixed FePt dimer is |10.37| meV, between those of the two iron and platinum monometallic cases |0.07| and |55.94| meV, respectively. Table 5 in company with Fig. 40 gives details of the results of our analysis. In the FePt dimer, the total magnetic moment of the Fe atom is $3.22\mu_B$ and that of the Pt atom - $0.58\mu_B$. The large magnetic moment of Fe can be attributed to the $3d$-Fe - to the $5d$-Pt atom charge transfer, which creates a polarization and an extra “hole charge” on the Fe atom.[53] This MCA value is higher in FePt system, compared to Fe_2, because the values of both the spin and orbital momenta are larger in the FePt dimer.

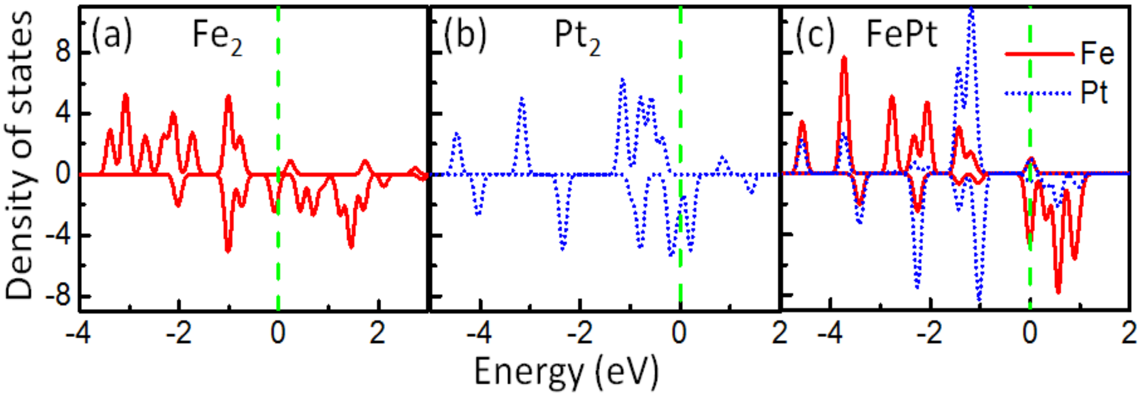

Figure 40. DOS of (a) Fe atom in the Fe_2, (b) Pt atom in the Pt_2 and (c) of the Fe and Pt atoms in the FePt dimer. The solid (red) line corresponds to DOS of Fe atoms and the doted (blue) to the DOS of the Pt atoms. The dashed green lines indicate the position of the HOMO levels of the dimers.

In all three cases, the easy axis of magnetization coincides with the direction of highest orbital momentum, in agreement with Bruno[170] (See Table 7). The negative value of MCA in FePt dimer means the easy axis of magnetization is perpendicular to the dimer axis in this case.

Table 7: MCA energy (in meV) and the spin and orbital moments of dimers (Fe, Pt and FePt) in different magnetization directions.

Dimer		Spin Moment (μ_B)		Orbital Moment (μ_B)		MCA
		(100) direction	(001) direction	(100) direction	(001) direction	E_{100}-E_{001}
Fe_2	This work	5.99	5.99	0.32	0.16	0.07
	GGA[189]	5.84	5.84	0.32	0.16	0.3
	LDA[190]	6.00	6.00	1.89	0.89	32
	GGA[53]	6.00	6.00	0.25	0.10	0.5
Pt_2	This work	1.89	1.38	2.74	0.80	55.94
	GGA[189]	1.88	1.34	2.74	0.80	46.3
	LDA[191]	1.90	1.65	2.40	1.20	220.0
	GGA[53]	1.80	1.70	2.40	0.80	75.00
FePt	This work	4.16	4.26	0.36	0.41	-10.37
	GGA[53]	4.30	4.30	0.2	0.40	

The projected DOS for the d orbitals of the Fe and Pt atoms in the dimers are shown in Fig.41. As follows from this figure, the majority spin orbitals have zero occupancy at the HOMO level, but the minority spin states are present there.

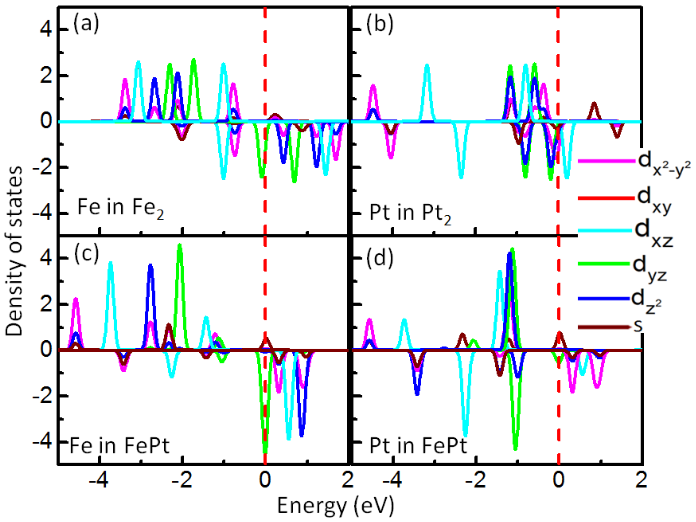

Figure 41. Projected DOS for the d orbitals for the Fe and Pt atoms in different dimers. The dashed lines highlight the HOMO level in each case.

This suggests that the hybridization-induced orbital charges are defined by the charge transfer for the spin-down electrons only. Therefore, the anisotropy and the magnetization of the dimers are generated by the minority spins as well.

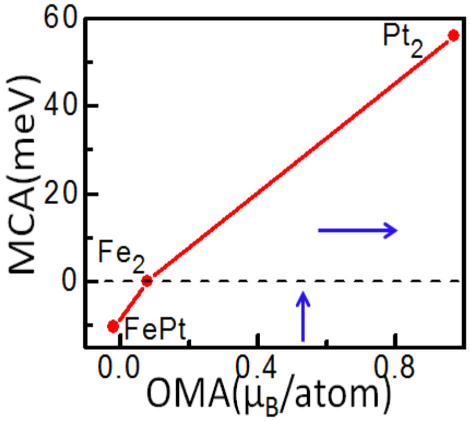

Figure 42. Orbital moment anisotropy (OMA) vs MCA of three dimers. The arrows indicate the direction of the easy axes for magnetization – perpendicular to the dimer axis for FePt and parallel for Fe_2 and Pt_2.

As it shown in Fig. 42, the MCA is proportional to the change of orbital momentum in two different directions; the comparatively small value of MCA for Fe_2 is due to its small SOC constant. Large SOC constant and relatively large orbital moment of Pt_2 results in a large MCA in this system. On the other hand, the intermediate value of MCA in the FePt dimer is caused by mutual tempering of each atom of the other's SOC and by intermediate value of the orbital moment (between those of Fe_2 and of Pt_2).

6.5 Magnetic anisotropy of $L1_0$ nanoparticles

The high MCA of bulk $L1_0$ FePt alloy has raised an interest in the magnetic properties of FePt nanoparticles, and several important results have been obtained. For instance, Muller *et al*. predicted theoretically that the $L1_0$ phase is not thermodynamically stable[192], and another study, by Jarvi *et al*.[193] showed that the structure may alter, disrupting the original atomic order. Moreover, several experimental studies support the existence of a minimum size below which the $L1_0$ order can no longer be achieved.[194,195] Other studies have shown the migration of Pt atoms towards the surface in smaller particles.[196,197] However, concerning feasibility of applications of the FePt nanoparticles more detailed and systematic studies are necessary to get more definitive answers.

Some experimental results are very encouraging. Namely, it is known in general that the magnetic properties of nanoparticles depend on the size, shape and the way of synthesizing.[9] Gas-phase particles can in fact exhibit *lower* MCA than perfectly-ordered bulk $L1_0$ alloys, because (i) their internal structure may not be perfect $L1_0$, and individual particles can become multiply-intertwined, (ii) the Pt atoms may tend to migrate towards the surface,[196,197] or (iii) an inhomogeneous alloying may be present from the beginning, as indicated by the EXAFS measurements by Antoniak *et al*.[198] The enhancement of surface-to-volume ratio (and hence the size) of a nanoparticle plays a significant role in its MCA. For example, the crystal symmetry-dependent quenching of the orbital magnetic moments disappears for all surface atoms of nanoparticles, thereby enhancing their orbital moments relative to those of bulk or core atoms[199] (Antioniak's XMCD measurements have confirmed this for surface Fe atoms in $L1_0$ FePt nanoparticles[200]).

The structures of the clusters considered in our analysis are shown in Fig. 43.

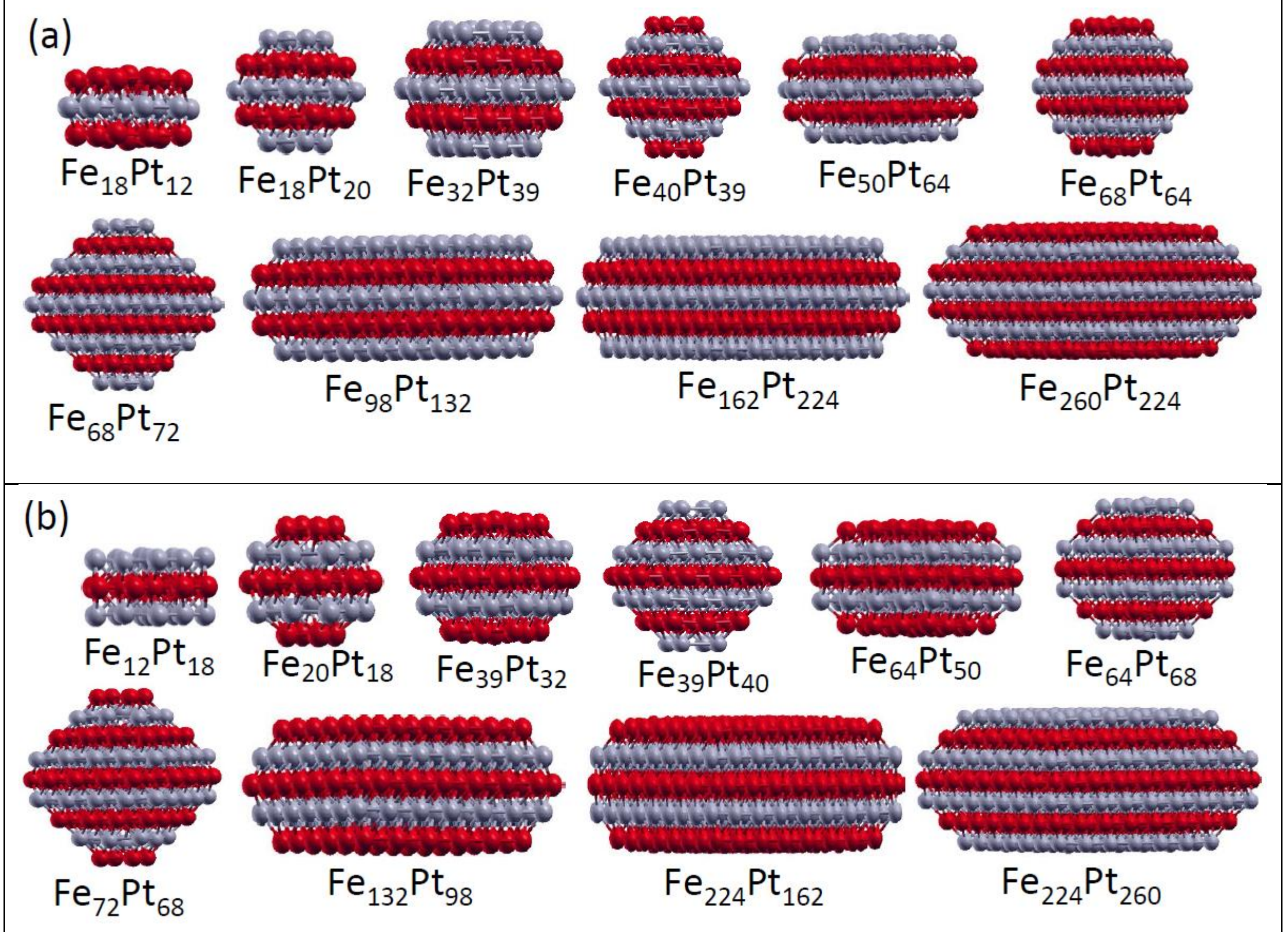

Figure 43. Clusters of the twenty $L1_0$ FePt nanoparticles under comparative study here. Dark (red) and light (gray) balls represent Fe and Pt atoms, respectively. The clusters whose central layer is composed of Pt atoms are presented in (a), and the clusters with central layer composed of Fe atoms are presented in (b).

The values of MCA for these clusters obtained with both direct and torque methods are presented in Fig. 44.

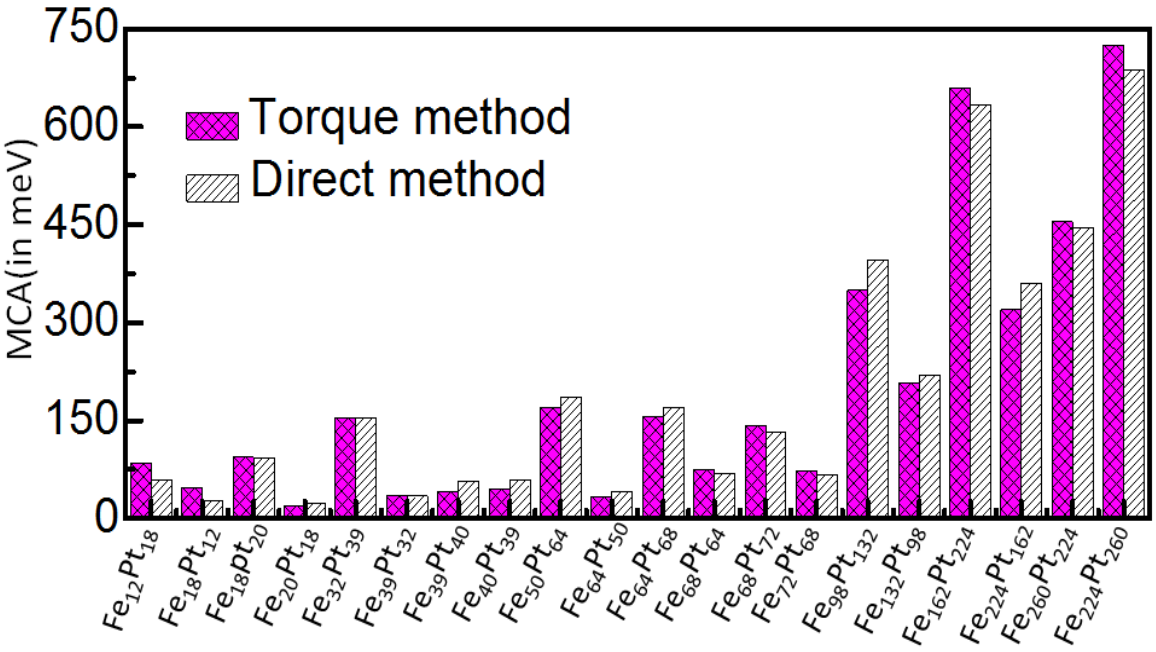

Figure 44: The light (white striped) bars represent MCA energy calculated by the direct approach and the dark (magenta crossed) bars indicate results under the torque approach.

The results for MCA calculated with the direct and torque methods agree well except for the smallest clusters ($Fe_{18}Pt_{12}$ and $Fe_{12}Pt_{18}$), for both of which the direct method gives higher MCA. One might expect that the torque method is not very accurate in the case of such small clusters, since torque calculations presuppose uniaxial symmetry of the system, and smaller clusters lose their symmetry upon relaxation. However, since there are no experimental values for MCA for such clusters, it is difficult to judge which method is more accurate for these systems. The overall agreement of the results for (many-atom) nanosystems by using these two different approaches is encouraging, because the direct approach is much more computationally demanding. One definite conclusion comes from our calculations is that those nanoparticles with a larger number of Pt atoms have larger MCA than their counterparts with a larger number of Fe atoms. Our calculations also show that the atoms inside the clusters have smaller magnetic moments than the surface atoms. As an example, the magnetic moments of $Fe_{72}Pt_{68}$ and $Fe_{68}Pt_{72}$ clusters are shown in Fig. 45. The green arrow in Fig. 45(a) indicates the line through which we calculate the magnetic moment. In Fig. 45(b), the red line with solid circles represents the magnetization of Fe atoms in the middle layer of $Fe_{72}Pt_{68}$ and the blue line with open circles represents the magnetization of Pt atoms in the middle layer of $Fe_{68}Pt_{72}$. It is clear from the Fig. 45(b) that the outer atoms in the cluster have larger magnetization than the inner atoms. This can be explained by a smaller number of neighbors for the exterior atoms.

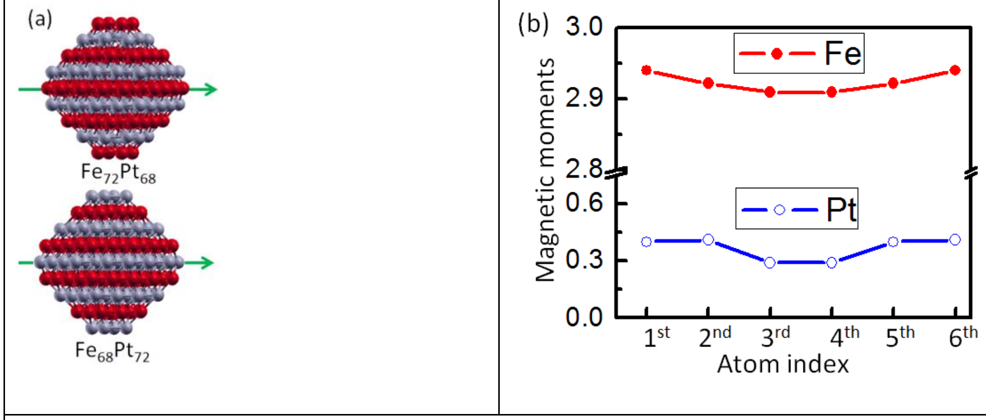

Figure 45: Magnetic moment of atoms at different positions in the central layer of the clusters. The green arrows in (a) indicate the atomic rows for which we plot the magnetization in Fig. b).

Though the Pt atoms in the bulk show zero magnetic moment, in the case of nanoparticles the moment is nonzero. The magnetic moments of the Fe atoms in the FePt clusters are higher than the moments of the bulk Fe atoms. The magnetization of the atoms inside the clusters is smaller than the magnetization of the outside atoms. These differences (between magnetization of atoms in pure bulk and in composite clusters, and between that of the interior and exterior atoms within the clusters of the same size) are due to the orbital hybridization of the Pt and Fe atoms. Because of the lower number of neighbors of the surface atoms, the spread of the corresponding Fe 3d- and Pt 5d-peaks in the DOS is smaller comparing to the bulk atoms, which leads to a larger unoccupied spin-down DOS, and hence larger magnetic moment of the surface atoms. The projected DOS for the atoms at different positions in the clusters are presented in Fig. 46.

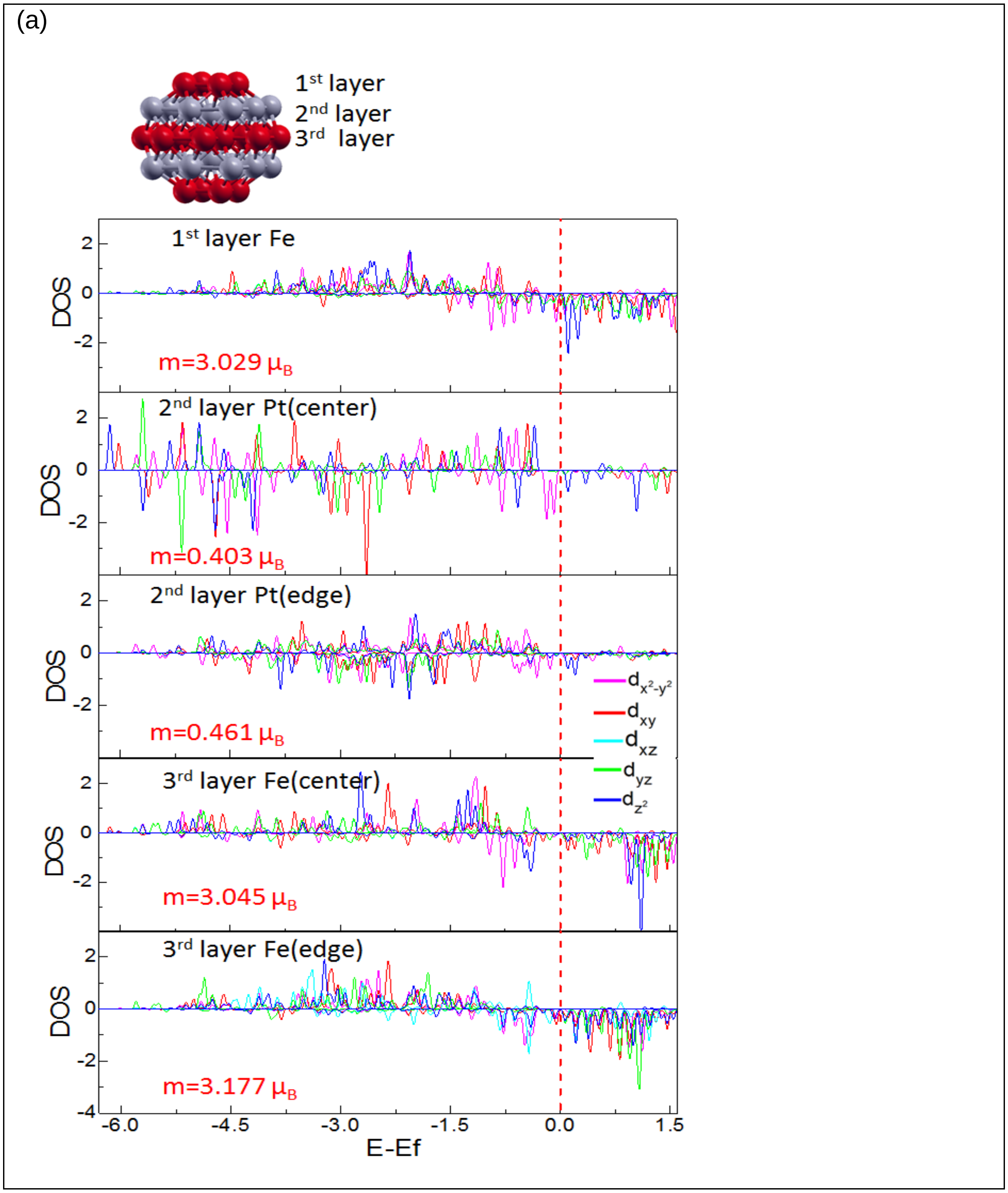
(a)
1st layer
2nd layer
3rd layer
1st layer Fe
m=3.029 μB
2nd layer Pt(center)
m=0.403 μB
2nd layer Pt(edge)
m=0.461 μB
3rd layer Fe(center)
m=3.045 μB
3rd layer Fe(edge)
m=3.177 μB
DOS
2
0
-2
-4
-6.0
-4.5
-3.0
-1.5
0.0
1.5
E-Ef
dx²-y²
dxy
dxz
dyz
dz²

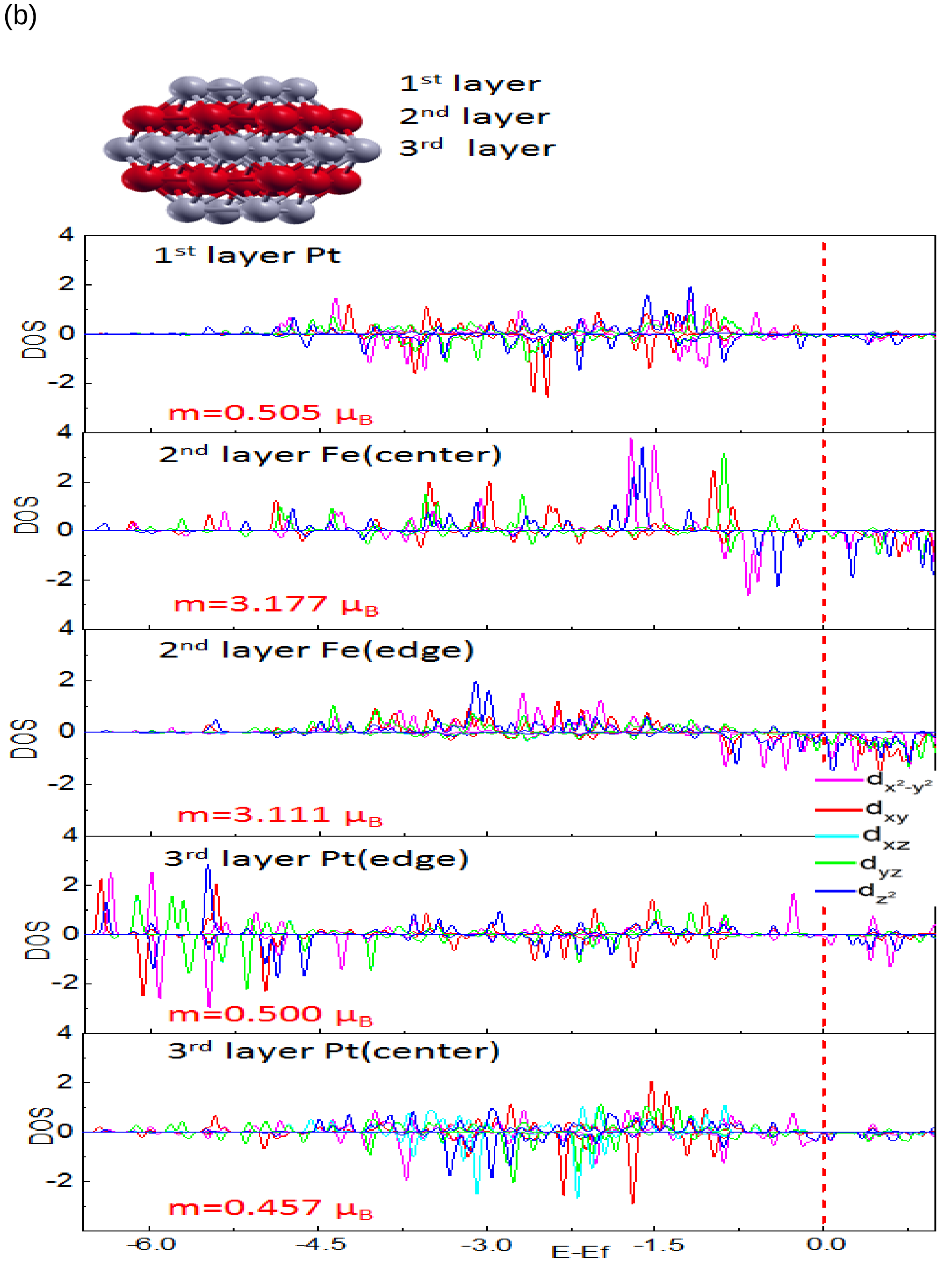

Figure 46: Projected DOS for the atoms at different positions in the (a) $Fe_{20}Pt_{18}$ and (b) $Fe_{18}Pt_{20}$ clusters. The values of the magnetic moment per atom in each layer m are also given.

It is clear from Fig. 46 that the projected DOS for the Pt atoms within the interior and at the periphery of the $Fe_{18}Pt_{20}$ cluster differ significantly, and the main contribution to this difference comes from the less-filled spin-down $d_{x^2-y^2}$ orbital in the case of the inside Pt atoms. This difference of projected DOS leads to a significant difference in the orbital moments of the inside and periphery atoms and hence to a high MCA. In the case of "flipped" cluster $Fe_{20}Pt_{18}$, the difference in the orbital occupancies between the inner and the periphery atoms is small for both Fe and Pt atoms. This difference leads to higher MCA per atom for bi-pyramidal structures with large central Pt layer as compared to the cuboctahedral ones.[201,202] For example, we get an MCA per atom 1.14 meV for the $Fe_{64}Pt_{68}$ versus 0.86 meV reported in Ref.[201] for the 147 atom cuboctahedral $L1_0$ FePt cluster. This difference can be traced to the larger percentage of Pt atoms in the center of the cluster in the bi-pyramidal structure as compared to the cuboctahedral one.

Table 8: The magnetic moments, orbital moments, and MCA of clusters along the parallel and perpendicular to the (001) direction of the cluster.

	Magnetic Moment (μ_B)		Orbital Moment (μ_B)		MCA (meV)
	m_x	m_z	l_x	l_z	MCA=(E_x-E_z)
$Fe_{12}Pt_{18}$	46.74	46.26	2.283	2.037	84.60
$Fe_{18}Pt_{12}$	62.33	62.03	2.14	2.54	47.60
$Fe_{18}pt_{20}$	68.16	68.06	3.31	2.97	94.37
$Fe_{20}Pt_{18}$	72.76	72.75	3.30	3.09	20.01
$Fe_{32}Pt_{39}$	117.18	115.19	5.86	4.46	154.28
$Fe_{39}Pt_{32}$	134.18	134.14	5.39	5.22	34.15
$Fe_{39}Pt_{40}$	133.57	132.46	5.74	5.17	81.05
$Fe_{40}Pt_{39}$	137.26	136.53	6.13	5.63	71.82
$Fe_{50}Pt_{64}$	175.97	175.67	7.95	6.91	170.11
$Fe_{64}Pt_{50}$	213.24	213.44	8.52	7.91	33.33
$Fe_{64}Pt_{68}$	214.84	214.76	9.64	8.24	155.90
$Fe_{68}Pt_{64}$	232.88	232.64	10.08	9.11	75.06
$Fe_{68}Pt_{72}$	233.90	231.71	10.59	10.06	142.80
$Fe_{72}Pt_{68}$	242.69	242.95	10.15	10.51	73.65
$Fe_{98}Pt_{132}$	350.02	350.78	16.90	14.57	349.38
$Fe_{132}Pt_{98}$	452.21	451.98	15.86	13.42	340.99
$Fe_{162}Pt_{224}$	583.97	583.97	28.11	23.63	659.77
$Fe_{224}Pt_{162}$	722.66	722.07	27.47	26.32	320.27
$Fe_{260}Pt_{224}$	870.00	870.21	36.10	33.38	454.44
$Fe_{224}Pt_{260}$	773.98	773.94	34.581	30.38	725.53

The spin moment and orbital moment were calculated by taking SOC into account. As Table 8 makes it clear, the total magnetic moment does not change significantly as the direction of the magnetization shifts from the parallel to the perpendicular one, contrary to the orbital moment. The change in value of orbital moment is such that, the easy (z-) axis of magnetization is always along the direction of its lower value. This finding does not follow Bruno's prediction,[170] according to which the easy axis of magnetization always coincides with the direction of the highest orbital moment. On the other hand, the direction of easy magnetization for dimers (Table 7) follows the Bruno's prediction. Thus, as our calculations show, there is change of the direction of easy magnetization upon the cluster size increase in the FePt system.

In general, the values of MCA also depend on the magnitude of the difference in the values of the x- and z-components of the orbital moments per atom, $\Delta l = l_x - l_z$. Indeed, Table 8 shows that for the majority of clusters the anisotropy is proportional to Δl. For the clusters of the same size, the anisotropy is higher in the clusters with higher SOC per atom (Pt atoms in this case). On the other hand, it is not easy to explain in simple terms the dependence of MCA on clusters composition.

The MCA of different layers of atoms within the clusters was also studied. Fig. 47 shows the results for the 38-atom clusters, as an example.

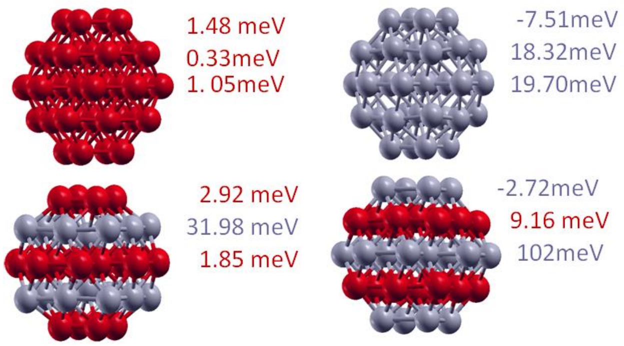

Figure 47: MCA of different layers of atoms in the four clusters consisting of 38 atoms. Dark (red) corresponds to Fe and light (gray) to Pt atoms.

As it follows from this Figure, the cluster has much higher MCA when the central plane consists of Pt atoms and the adjoined layers are built from Fe atoms. This conclusion is valid for all clusters studied in this thesis. The effect can be attributed to the hybridization of Pt 5d- and Fe 3d-orbitals. Namely, the orbital moment of Pt atom increases because of this hybridization (In the example above, the Pt atom in the $Fe_{20}Pt_{18}$ cluster shows an orbital moment of $0.11\,\mu_B$ but in $Fe_{18}Pt_{20}$ its orbital moment increases to $0.145\,\mu_B$). This increase in the orbital moments, along with high SOC of the Pt atoms, increases the MCA of the central Pt layer in the cluster. The values of the orbital moments of the Pt atoms in the $Fe_{18}Pt_{20}$ cluster are much higher than in Pt_{38}

system$(0.02\,\mu_B)$, and then the moment of Fe atoms in Fe_{38} $(0.06\,\mu_B)$, $Fe_{20}Pt_{18}$ $(0.06\,\mu_B)$ and $Fe_{18}Pt_{20}$ $(0.04\,\mu_B)$. The same pattern holds for all sizes of clusters we studied in this thesis.

Since the widths of the part of the d-bands that contribute to SOC are much smaller than the total width of the d-bands as a whole, the MCA can be explained by a simple perturbation theory in d-orbital occupancy. In this case, all the majority spin states are completely occupied (see Fig. 48), so all the empty states belong to the minority spins only and MCA is defined by the minority band. There are two possible types of the SO interactions in these systems: the coupling between the occupied spin-down and unoccupied spin-down states and the coupling between the occupied spin-up and unoccupied spin-down states. The MCA energy can be calculated by using the following formula:[192]

$$E_X - E_Z \sim \xi^2 \sum_{o,u} \frac{|\langle o|\hat{\boldsymbol{L}}_{\boldsymbol{z}}|u\rangle|^2 - |\langle o|\hat{\boldsymbol{L}}_{\boldsymbol{x}}|u\rangle|^2}{\varepsilon_u - \varepsilon_o} \tag{6.9}$$

where ξ is the spin-orbit coupling constant, ⟨o| and ⟨u| are the occupied and unoccupied minority spin states, respectively, and $\hat{\boldsymbol{L}}_{\boldsymbol{z}}$ and $\hat{\boldsymbol{L}}_{\boldsymbol{x}}$ are the z- and x-components of the angular momentum operators. The orbital occupancies of both empty and filled states of both spin arrangements for $Fe_{20}Pt_{18}$ cluster are shown in Fig. 48 and Table 9. By using equation (6.9) and values from Table 9 we find that for the Fe atom in the 1st layer of $Fe_{20}Pt_{18}$ $E_x - E_z = 0.24\xi^2$, for the atoms in the 3rd layer (exterior) of $Fe_{20}Pt_{18}$ this value is $E_x - E_z = 0.17\xi^2$ and for the atoms in the 3rd layer(interior) of $Fe_{20}Pt_{18}$ one gets $E_x - E_z = 0.08\xi^2$.

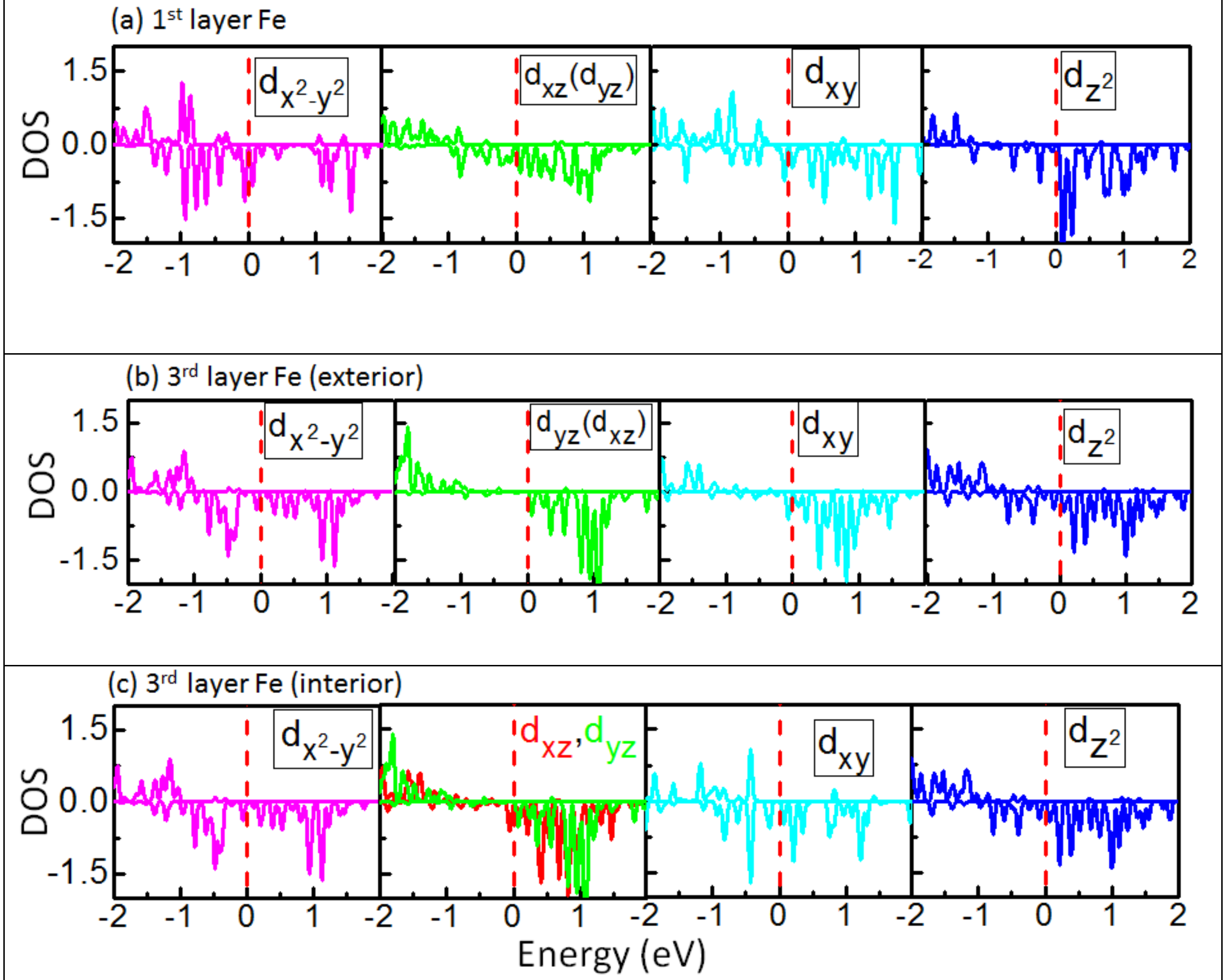

Figure 48: Projected DOS for the Fe atom (a) in the 1st layer, (b) on the edge of 3rd layer and (c) in the interior of the 3rd layer of the $Fe_{20}Pt_{18}$ cluster.

The contribution of SOC is lower by half for 3rd-layer exterior atoms than that of the 1st-layer atoms (all of which are on the cluster's surface), and this contribution for the 3rd-layer interior atom is lower by one-third than that of the 1st-layer atoms. Next, in the 3rd-layer of $Fe_{20}Pt_{18}$ there 12 atoms (4 interior, 8 exterior) and if one assumes that each interior and exterior atom gives the same contribution to the MCA, one obtains that the anisotropy for the 1st layer is 2.5 times greater than that for the 3rd layer. The DFT calculations give the value 3 for this quantity (see Fig. 47). The discrepancy between the estimated and DFT results may take place due to simplicity of the estimation used. In particular, for more accurate estimation, the differences in hybridization for the orbitals on each individual atom need to be taken into account.

Table 9. The d orbitals occupancy of different atoms in the 1st and 3rd Fe layers in the $Fe_{20}Pt_{18}$ cluster.

Projected *d*-orbitals	1st-layer atom (all exterior)	3rd-layer atom (exterior)	3rd-layer atom (interior)
$d_{x^2-y^2}$	0.51	0.45	0.45
d_{xy}	0.29	0.17	0.25
d_{xz}, d_{yz}	0.30	0.10	0.16, 0.13
d_{z^2}	0.18	0.28	0.28

6.6: Thermal effects and the stability of magnetism

All the calculations above correspond to the case of zero temperature. For the potential applications of FePt nanoparticles in the magnetic storage of data one needs to take into account the temperature effects. In particular, it is possible that the direction of magnetization of small nanoparticles can be unstable at room temperature, thus making them unsuitable for memory storage. Usually, the magnetic stability time of magnetic particles (defined by the probability of “climbing” of the system over the energy barrier) is estimated by using the Arrhenius law[203]. According to this law, the stability time is defined by the (large value) ratio of the anisotropy energy to the thermal energy. In particular, for the stability time T = 25 years, one needs

$$\frac{KV}{k_B T} = ln\left({}^{T}\!/_{T_0}\right) \geq 41. \qquad (6.10)$$

In the last Equation, K is the anisotropy energy per unit volume, V is the volume of the system, and T_0 is the attempt time for the system to climb the anisotropy barrier. We have used $T_0 = 10^{-9} sec$ in our calculations. With the largest value of the anisotropy KV= 725 meV obtained for the $Fe_{224}Pt_{260}$ cluster in our calculations, one gets

$$\frac{KV}{k_B T} = 28, \qquad (6.11)$$

i.e. the total anisotropy energy of our largest nanoparticle is not large enough for 25 year magnetic stability. To get the desired ratio of the energies 41, one needs the anisotropy energy for the particle to be approximately 1060 meV. This means that to use the FePt nanoparticles in the magnetic storage devices their size needs to be larger than 484-atom structures. To estimate the desired size, we extrapolated our results for the MCA on the case of larger systems. As it follows from Fig. 44, for the clusters with fixed number of layers the MCA scales almost linearly with the number of Pt atoms in the cluster. The corresponding linear extrapolation in the case of 5-layer clusters with Pt as central layer is shown in Fig. 49.

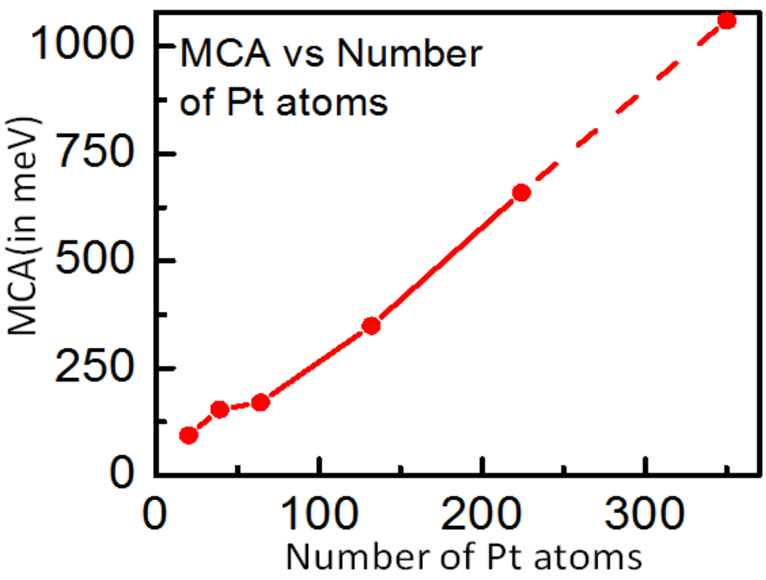

Figure 49: MCA as a function of the number of Pt atoms in the five-layer $L1_0$ FePt clusters with Pt as the central layer.

As it follows from Fig. 49, the $L1_0$ clusters that has central Pt layer with approximately 350 Pt atoms have the desired value of MCA 1060 meV. The corresponding number of Fe atoms for this type of structure is approximately 270. Thus, our estimation shows that the $L1_0$ $Fe_{270}Pt_{350}$ and larger particles should have sufficiently large MCA to be used in practical applications in the magnetic storage technologies. It is important to mention that for other applications, for example MRI, where the stability of the magnetization, not magnetic anisotropy, is important, one can use smaller nanoparticles.[204]

To understand better the thermal properties of the FePt clusters, one needs to calculate the temperature dependence of the magnetization M(T). The large numbers of the unknown exchange parameters in the nanoparticle makes this problem very difficult to solve exactly. Below, we perform an estimated analysis of how the magnetization varies with temperature for different sizes and shapes of nanoparticles, by using an effective spin model for the subsystem of the Fe atoms.

Namely, the thermal-averaged magnitude of the spin can be calculated as

$$\langle S\rangle = SB_S(x) \tag{6.12}$$

where

$$B_s(x) = \left(\frac{(2S+1)}{2S}\right) coth\left(\frac{(2S+1)x}{2S}\right) - \left(\frac{1}{2S}\right) coth\left(\frac{x}{2S}\right) \tag{6.13}$$

is the Brillouin function and its argument

$$x = \frac{g\mu_B S H_{eff}}{k_B T} \tag{6.14}$$

is the ratio of the magnetic energy to the thermal energy. In Eq. (6.14) g is the gyromagnetic ratio, S is the spin, H_{eff} is the effective magnetic field, and μ_B is the Bohr magneton.

For a body centered cubic structure of bulk Fe $H_{eff} = 8J\langle S\rangle$ where, J is the exchange constant and <S> is the thermal averaged magnitude of the spin. The coefficient 8 is the number of the nearest-neighbor atoms in the bulk iron system.

The exchange constant J can be estimated from the value of the critical temperature T_c. Near T = T_c the Brillouin function in equation (6.14) is

$$B(x) \approx \left(\frac{S+1}{3S}\right)x. \tag{6.15}$$

From equations (6.12) with (6.15) one gets

$$J = \frac{3kT_c}{8g\mu_B S(S+1)}, \tag{6.16}$$

where for T_c one can use the experimental value for the bulk iron 1043 K.

The standard mean-field theory of exchange cannot be applied to nanoparticles, since the system contains many non-equivalent atoms and the effective field is site-dependent. Therefore, we use a self-consistent local-mean-field magnetic model[205] in our analysis. We present the steps of the calculations in this approach on the example of the $Fe_{20}Pt_{18}$ cluster.

We label each Fe atom in the nanoparticle by a number, as shown in Fig. 50.

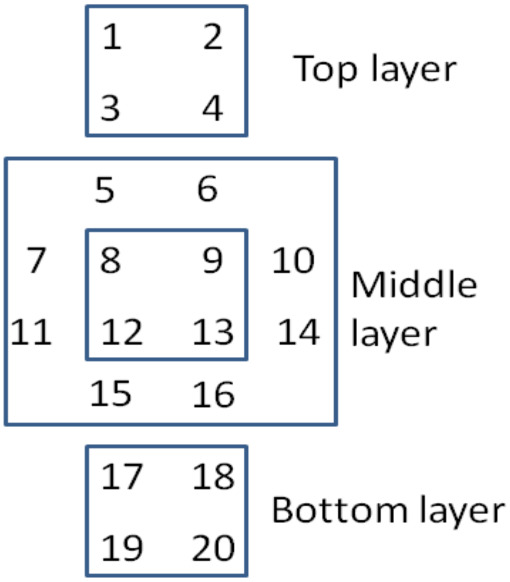

Figure 50: Schematic representation of the $Fe_{20}Pt_{18}$ cluster in the local mean-field model.

Then, we calculate the effective field for each spin, by taking into account the nearest-neighbor exchange coupling. Two types of coupling are identified:

1) In-plane nearest-neighbor coupling with the exchange constant J
2) Out-of-plane nearest-neighbor coupling with the exchange constant J_p

For example, the effective field that acts on spin 1 in Fig. 50 can be written as

$$H_1 = J(\langle S_2 \rangle + \langle S_3 \rangle) + J_p \langle S_8 \rangle \ , \tag{6.17}$$

here $\langle S_n \rangle$ is the thermal averaged magnitude of the spin at site n. Then, one can write the effective field equation for each of the site in the cluster:

$$\langle S_n \rangle = S_n B(x_n), \tag{6.18}$$

The site-dependent functions x_n are

$$x_n = \frac{g_n \mu_B S_n (\langle S_n \rangle H_n + H_0)}{KT}. \tag{6.19}$$

We solved the corresponding set of coupled equations for $<S_n>$ (n changes from 1 to number of Fe atoms in the cluster) iteratively by starting from an initially chosen values for $<S_n>$.

The following parameters were used in the calculations: $\mu_B = 9.27 \times 10^{-21}$ erg-Gauss, Boltzmann's constant is $k = 1.38 \times 10^{-16}$ erg/Kelvin, gyromagnetic ratio g = 2, exchange coupling $J = 1.455 \times 10^{6}$ Oe (bulk values of Fe), and spin S = 1. To help orient the moments in desired direction and speed up the convergence of our calculations we used a small external magnetic field $H_o = 100$ Oe. We used two different values for the perpendicular coupling J_p; $J_p = J$ and $J_p = 0.5J$ to see how the coupling between different planes of Fe atoms affects the results.

In Fig. 51 we present our results for the $Fe_{20}Pt_{18}$ and $Fe_{39}Pt_{40}$ clusters. The critical temperatures of the particles are substantially smaller than the critical temperature of bulk Fe ($T_c = 1043K$). However, the magnetic moments at room temperature are still substantially large. We attribute the reduction in T_c to the reduced coordination number of the Fe atoms in the FePt clusters as compared to the bulk Fe. For the larger clusters one might expect smaller effect of the reduced coordination, because the percentage of atoms at the surfaces and edges is decreasing with the increasing the particle size.

Indeed, the value of T_c is larger for the $Fe_{39}Pt_{40}$ particle comparing to the $Fe_{20}Pt_{18}$ one. We obtained higher values of the critical temperature for larger value of the perpendicular coupling, as expected. This trend is consistent with the experimental data showing that larger FePt nanoparticles have a higher $T_{c.}$[206]

In Fig. 51(b) we presented the thermal average values of spin at different sites of the cluster at $J_p = 0.5J$. As it follows from Fig. 51(b), there are only three unique types of the Fe sites for the $Fe_{20}Pt_{18}$ and six unique sites for the $Fe_{39}Pt_{40}$ clusters due to symmetry of the configurations. It is important to mention that the magnetic moments at the different sites are quite different even for moderate temperatures, and the thermal averaged values for spins at the center sites are significantly larger as compared to the outer surfaces and edges sites for a wide temperature range.

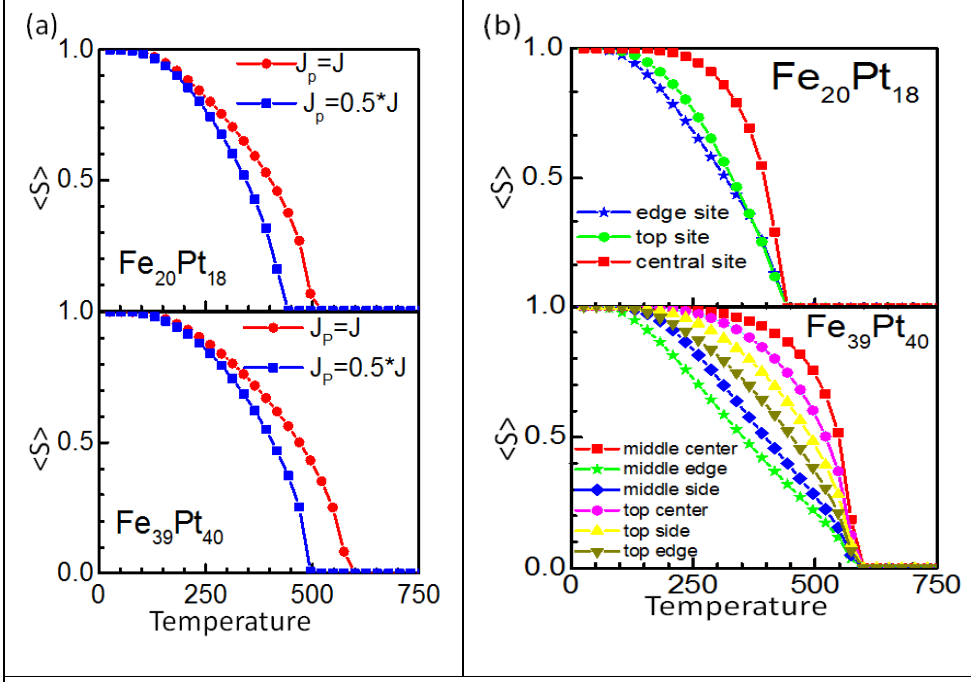

Figure 51: (a) Averaged spin as a function of temperature for $Fe_{20}Pt_{18}$ (top) and $Fe_{39}Pt_{40}$ (bottom) clusters; (b) averaged spin for non-equivalent sites in $Fe_{20}Pt_{18}$ (top) and $Fe_{39}Pt_{40}$ (bottom) clusters. The results in Fig. (b) Correspond to $J_p = 0.5J$.

Despite simplicity of the model one can get a rather general idea about the thermal properties of FePt nanoparticles.

6.7: Molecular Dynamics (MD) and the stability of $L1_0$ structures

To check the stability of the $L1_0$ configurations, we performed *ab-initio* molecular dynamic (MD) simulations for the $Fe_{18}Pt_{20}$ and $Fe_{20}Pt_{18}$ clusters. The clusters were heated to 1000k with 3.0 fs in 5000 steps with micro-canonical ensemble (NVE), and there was no symmetry imposed during the MD calculations. We took five minimum energy seeds for each of the clusters from the heating curve and allowed them to cool to 0 K with the temperature step of 300K. Finally, we took the resulting 0K structures as the initial structures and relaxed them within spin-polarized DFT.

The results of those MD simulations are presented in Fig. 52

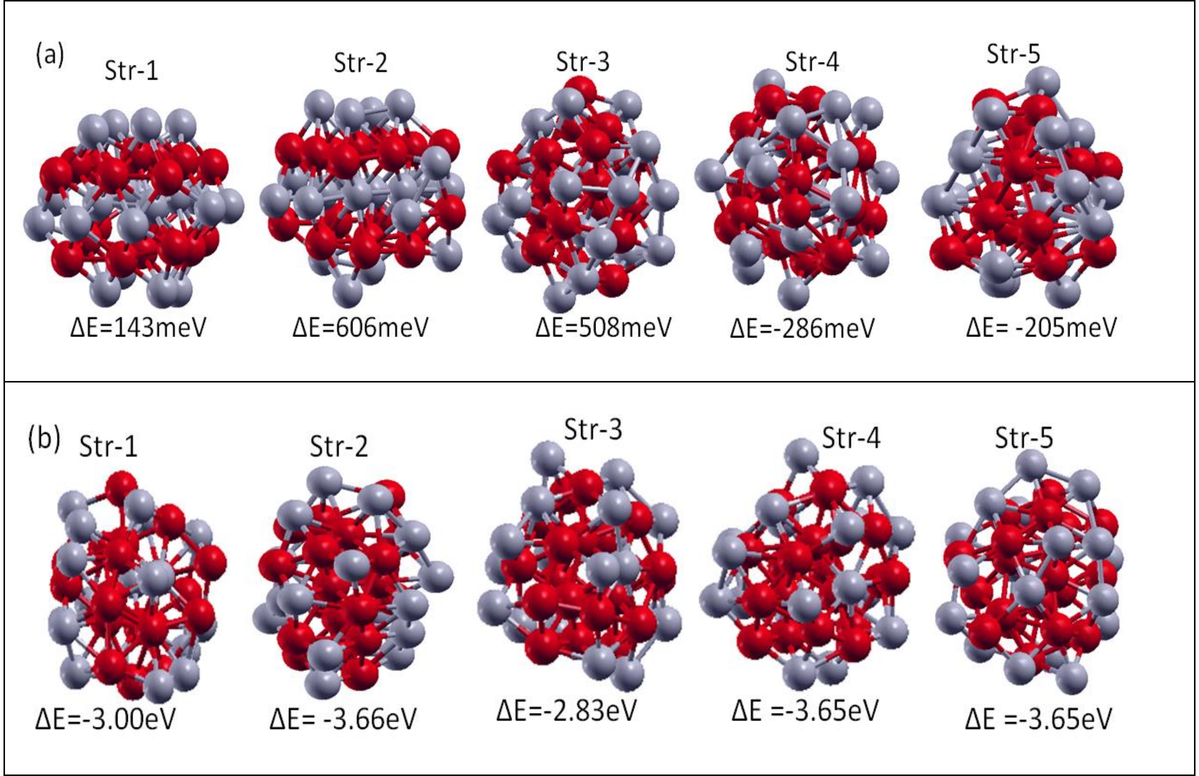

Figure 52: Relaxed structures of five minimum energy seeds from MD simulation for (a) $Fe_{18}Pt_{20}$ and (b) $Fe_{20}Pt_{18}$ clusters. $\Delta\boldsymbol{E}$ represent the energy of the cluster with respect to the energy of the perfect $L1_0$ structure of the same size.

Most of the structures in Fig.52 have lower energy than the perfect $L1_0$ structures presented in Fig. 43. This means that for such small clusters the $L1_0$ phase is not stable at high temperatures. Indeed, in the experiments[207] a transition from the disordered A1 to ordered $L1_0$ phase was observed at temperature around 500˚C, and it was found that the ordered phase started to generate on the surface of the nanoparticles and propagated towards the center of the structure. The complete ordering was observed for few minutes at a temperature of 600˚C. The size of the nanoparticles was less than 3nm. It was also found that the magnetic anisotropy of these disordered nanoparticles is much smaller than that of the ordered $L1_0$ nanoparticles, as can be seen from Table 10. It is worth mentioning here that the Str1 of the $Fe_{18}Pt_{20}$ is very close to the $L1_0$ structure as shown in Fig. 52, and it has anisotropy energy much higher than other disorder structures, and in all cases the $L1_0$ structures have much higher anisotropy than the disordered structures with same chemical composition, suggesting the special magnetic properties of the $L1_0$ systems.

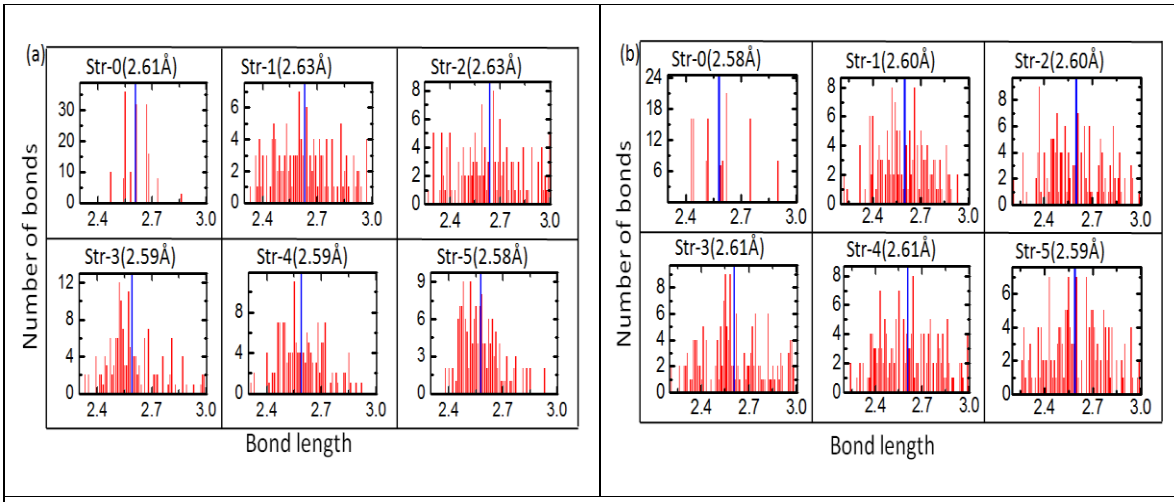

Figure 53: Bondlength distribution of (a) $Fe_{18}Pt_{20}$ and (b) $Fe_{20}Pt_{18}$ clusters. Str-0 represents perfect $L1_0$ cluster and Str-1 to Str-5 represent the relaxed structures obtained from the MD simulations.

The bondlength distribution of 38 atoms clusters are presented in Fig. 53. As it follows from this Figure, the bondlength distribution of the $L1_0$ structures is rather confined, contrary to the MD-relaxed systems. This suggests that after annealing the $L1_0$ structure got melted and it relaxed with structures completely different from the $L1_0$ type. This feature is clear also from the Fig. 53 that the Fe and Pt atoms are completely mixed up.

Table 10. MCA for different structures of 38-atoms FePt clusters.

Structures	MCA(meV) $Fe_{18}Pt_{20}$	MCA(meV) $Fe_{20}Pt_{18}$
$L1_0$	94.00	24.00
Str1	65.51	0.97
Str2	8.74	9.11
Str3	5.71	3.58
Str4	3.10	13.51
Str5	-11.18	10.51

The relation between the structure and MCA of FePt nanoparticles is not well understood so far. For example, 147-atom cuboctahedral FePt clusters encapsulated into Cu-, Au-, and Al matrices were studied theoretically in Ref. [51], as an alternative type of system. It was found in this paper that, contrary to our findings, the surface atoms have larger MCA than the bulk ones. Our results for the FePt bi-pyramidal nanoparticles suggest that one can avoid necessity to protect the MCA by encapsulating the particles, since the large MCA region in the bi-pyramidal structures is mostly located in the center of the particles.

6.8 Conclusions

The magnetic properties of $L1_0$ nanoparticles as a function of particle sizes (from 30 to 484 atoms) and compositions (i.e., consisting of pure Fe and Pt atoms and of alternating planes of Fe and Pt atoms) are studied systematically. The MCA of L1_0 FePt nanoparticles are found to be higher than the bulk system. This high MCA can be explained by the hybridization of the $5d(Pt)$ orbitals with $3d(Fe)$ orbitals in the layered FePt nanoparticles. Clusters with the central Pt layer atoms are found have much larger anisotropy than those with the central Fe layer. The explanation for this is that the central layer has more atoms than other layers in the cluster, and when *these* atoms are of high orbital moment – Pt atoms hybridizing with the Fe atoms below and above – the system as a whole exhibits higher anisotropy than when is central layer consists of Fe atoms, whose orbital moment, in hybridizing with the Pt atoms above and below, is markedly lower. To preserve MCA for practice applications one can eliminate the needs of capping in this case since the nanoparticles with bi-pyramidal structure studied in this thesis possess MCA mostly at the (large) central Pt layer. We extrapolate that five-layered L1_0 FePt nanoparticles with approximately 700 atoms can be expected to be useful in magnetic recording applications at room temperatures. The theoretical results obtained in our studies can help in experimental search of better candidates for magnetic applications that exploit MCA. The relation between the structure and MCA is not yet completely understood for FePt and other binary alloys in general. For example, the surface atoms was found to have larger MCA in 147-atom cuboctahedral FePt clusters encapsulated into Cu-, Au-, and Al in Ref.[201,202]. Another consideration is the particular role of electron-electron correlation in these systems. This was found to be important for small Fe and FePt clusters [47,48] and invite further study.

In the next Chapter, we give a summary of the results presented in this thesis.

CHAPTER 7 SUMMARY

In this thesis we studied the magnetic properties of TM nanosystems by taking into account the effects of strong electron-electron correlation within DFT+DMFT approach.

For this purpose we formulated a nanoDFT+DMFT approach and developed a numerical code, which was used in the calculations. We demonstrated that the correlation effects play an important role in these systems, and in order to take them properly into account one needs to go beyond the DFT+U approximation. Indeed, in the last case, important physical processes – time-resolved orbital occupancies – are ignored, which lead to oversimplified description of the materials with results in some cases very different from the experimental data. More explicitly, the following results were obtained.

In small Fe and FePt clusters, we found that dynamical correlation effects lead to a significant decrease of the magnetization with respect to DFT+U results. This can be explained by the following reasons. The time-dependence of the orbital occupancy taken into account in the DMFT approach leads to a significant decrease of the magnetization relative to “the staggered” DFT+U case. Also, the frequency-dependence of the self-energy can lead to a shift of the energy levels with respect to the Fermi energy, and hence to a change of the level occupancy and magnetization. The geometry, chemical composition, and local Coulomb repulsion dependencies of the magnetization of the clusters were also analyzed. We have found that correlation effects play a very important role in small clusters.

In the case of larger 10-147-atom, Fe nanoparticles, we have found that inclusion of the dynamical effects through DFT+DMFT results in overall better agreement between the theoretical and experimental [34,58] results for the magnetic moments. In particular, it was shown that contrary to DFT and DFT+U, DFT+DMFT is capable to describe oscillations of the magnetization per atom as function of the cluster size observed experimentally. We demonstrated that DFT+DMFT applied to experimentally realizable nanoparticles can produce accurate results. The methodology should have multiple applications, including larger (several-hundred atom systems). It can be readily applied to systems containing up to several hundred atoms. The computational speed of the developed code is such that the total computational time of the DFT+DMFT calculations is of the same order of magnitude as the corresponding time for the DFT calculations.

We analyzed also the electronic and magnetic properties of the (001) film of Fe_2O_3, paying a special attention to the properties of the surface. We found that, similar to bulk, there is a gap in the spectral function due to the strong electron-electron correlation in the system. The reduced magnetization of the surface atoms compared to the bulk atom is explained to be the effects of extra peaks in the projected DOS of some orbital, which can be obtained only with DFT+DMFT. The surface electronic and magnetic states are rather different from the bulk ones which might also have some applications in the magnetic technologies.

Finally we analyzed magnetic anisotropy of TM nanoparticles and presented results for $L1_0$ FePt nanoparticles of size up to 484 atoms. We find that nanoparticles have much higher magnetic moments and MCA than do bulk atoms. This is due to the fact that the

MCA arises from the orbital moment coupled with the spin moment and that in the bulk the system orbital moments are almost quenched, whereas in small clusters the orbital moments of the system's atoms are considerably enhanced. We propose that this explains why it is that (as earlier studies have shown) the hybridization of the $5d(Pt)$ orbitals with $3d(Fe)$ orbitals produces a high magnetic anisotropy for layered FePt nanoparticles. We also find that clusters with Pt atoms as the central layer have much larger anisotropy than those in which the central layer consists of Fe atoms. The explanation for this is that the central layer has more atoms than other layers in the cluster, and when *these* atoms are of high orbital moment – Pt atoms hybridizing with the Fe atoms below and above – the system as a whole exhibits higher anisotropy than when is central layer consists of Fe atoms, whose orbital moment, in hybridizing with the Pt atoms above and below, is markedly lower. In contrast to the cuboctahedral case, bi-pyramidal nanoparticles possess MCA mostly at the (large) central Pt layer. This fact may eliminate the need to cap them in order to preserve MCA. We hope that our results can help experimentalists in search of (larger) high-density nanoparticles exploitable in recording devices. Meanwhile, a deeper analysis of the electronic structure of these systems including the effects of strong electron correlations with localized *d*-orbitals needs to be performed.

APENDIX A: SLATER-KOSTER METHOD FOR CALCULATING HOPPING MATRIX ELEMENTS

To derive the general formula for the hopping parameters in the Slater-Koster approximation[126], and use it for the s-, p- and d-orbitals, we begin with the Schrödinger Equation for an electron with angular-momentum quantum number l that moves in the central (ion) field:

$$-\frac{\hbar^2\nabla^2}{2m}\psi(r)+v(r)\psi(r)=\varepsilon\psi(r), \qquad \text{(A.1)}$$

where $\psi(r)$ is the particle wave-function, ε is its eigen-energy and $v(r)$ is the central potential. For a spherically symmetric potential, the electronic wave-function can be decomposed into a product of the radial $R_l(r)$ and spherical $Y_l^m(\theta,\phi)$, parts. In the expression for the last, spherical harmonic, function l and m are the quantum numbers of the angular momentum and its projection, θ is the angle of the electron vector radius with respect to the Z-axis and ϕ is the azimuthal angle. For the $s-$ and $p-$states, the angular number l is zero and 1, respectively and for the d-states l=2. m, which is also called the magnetic quantum number, can have values $-l \leq m \leq l$ .The harmonics for different orbitals are shown in Fig. 54

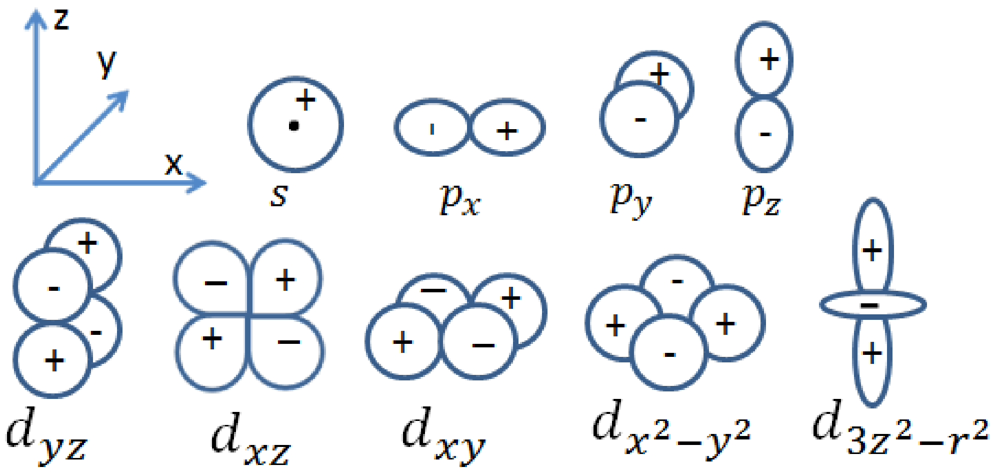

Figure 54: Schematic representation for possible angular harmonics of the electron wave functions in the atomic s-, p- and d-states.

The radial part of the wave function in equation (A.1) satisfies the following equation:

$$-\frac{\hbar^2}{2m}\frac{1}{r^2}\frac{\partial}{\partial r}r^2\frac{\partial}{\partial r}R_l(r)+V(r)R_l(r)+\frac{\hbar^2 l(l+1)}{2mr^2}R_l(r)=\varepsilon_l R_l(r). \qquad \text{(A.2)}$$

The solution of Equation (A.2) gives one the radial-dependence of the wave function, which will be needed to calculate hopping matrix elements. The elements (coupling) between two d states $|d\rangle$ and $|d'\rangle$ on different atoms can be written in the second-order perturbation theory expansion as

$$\langle d'|H|d\rangle=\sum_k\frac{\langle d'|H|k\rangle\langle k|H|d\rangle}{\varepsilon_d-\varepsilon_k}, \qquad \text{(A.3)}$$

Where k numerates all possible states, which can be expanded in the spherical harmonics (in volume Ω):

$$|k\rangle = \frac{1}{\sqrt{\Omega}} \sum_l (2l+1) i^l j_l(kr) \left(\frac{4\pi}{2l+1}\right)^{1/2} Y_l^0(\theta, \phi). \tag{A.4}$$

The $j_l(kr)$ are Bessel function solutions of equation (A.2) at $V(r) = 0$.

The atomic functions are orthogonal to the metallic states:

$$\left\langle k \middle| -\frac{\hbar^2}{2m}\nabla^2 + V_a \middle| d \right\rangle = \varepsilon_d \langle k|d\rangle = 0. \tag{A.5}$$

(where V_a is the atomic potential). In fact the potential experienced by electrons in solids is different from the atomic potential

$$V(r) - V_a(r) = \delta V, \tag{A.6}$$

Therefore, the hybridization (overlap) of the metallic and atomic states is defined by this difference of the potentials (for details, see Ref. [208]):

$$\langle k|H|d\rangle = \langle k|\delta V|d\rangle = \langle k|\delta V - \langle d|\delta V|d\rangle|d\rangle, \tag{A.7}$$

or

$$\langle k|H|d\rangle = \frac{-4\pi}{\sqrt{\Omega}} Y_l^m(\theta_k, \phi_k) e^{-ik.r_j} \int j_2(kr)(\delta V - \langle d|\delta V|d\rangle) R_2(r) r^2 dr, \tag{A.8}$$

where r_j the position of nucleus.

The approximate evaluation of the integral in the last equation can be performed and the result defined in terms of an effective orbital radius r_d (d-orbital used to be specific):

$$r_d{}^{3/2} = -\frac{1}{3}\sqrt{\frac{4\pi}{3}}\frac{m}{\hbar^2}\int r^4(\delta V(r) - \langle d|\delta V|d\rangle)R_2(r)dr, \tag{A.9}$$

which gives

$$\langle k|H|d\rangle = \sqrt{\frac{4\pi r_d{}^3}{3\Omega}}\frac{\hbar^2k^2}{m}Y_2^m(\theta_k,\phi_k)e^{-ik.r_j}. \tag{A.10}$$

The last expression needs to be substituted in Equation (A.3), which gives the hopping parameters in terms of the atomic radius r_d and the distance between two nuclei for the d −states, $d = r_j(d) - r_j(d')$.

For d-orbitals, one gets:

$$V_{ddm} = \frac{4\pi r_d^3}{3\Omega}\frac{\Omega}{(2\pi)^3}\int\left(\frac{\hbar^2k^2}{m}\right)^2\frac{Y_l^{m^*}(\theta,\phi)Y_l^m(\theta,\phi)e^{ikdcos\theta}}{\varepsilon_d-\varepsilon_k}d^3k \overset{\text{def}}{=} \eta_{ddm}\frac{\hbar^2r_d^3}{md^5}. \tag{A.11}$$

From the analysis of Harrison and Froyen,[208] one can obtain the numerical values of different coefficients η:

$$\eta_{dd\sigma} = -\frac{45}{\pi}, \eta_{dd\pi} = \frac{30}{\pi},\ \eta_{dd\delta} = -\frac{15}{2\pi}. \tag{A.12}$$

(corresponding to $m = 0, 1\ and\ 2$, respectively).

In the similar way, one can obtain the transition elements between the s- and p-states[209]:

$$V_{ll'm} = \eta_{ll'm}\left(\frac{\hbar^2}{md^2}\right), \tag{A.13}$$

with

$$\eta_{ss\sigma} = -\frac{9\pi^2}{64}, \tag{A.14}$$

$$\eta_{sp\sigma} = 3^{3/2}\frac{\pi^2}{64},$$

$$\eta_{pp\sigma} = \frac{3\pi^2}{16},$$

$$\eta_{pp\pi} = -\frac{3\pi^2}{32}.$$

In the case of different position of two atoms (as shown in Fig: 55), orbital orientation can have any possible form. Follow Slater and Koster's [126], one can obtain general expression for the hopping matrix elements by using the expressions for matrix element V and vector $\vec{d} = [l, m, n]d$ that connects two atoms (l, m, n are the unit vector components). The following notations are used below: the matrix element for the hopping between the states xy to yz separated by distance d is called $E_{xy,yz}$ and is expressed in terms of $V_{dd\sigma}$, $V_{dd\pi}$, $V_{dd\delta}$, l, m and n. The results are given in the Table-A1.

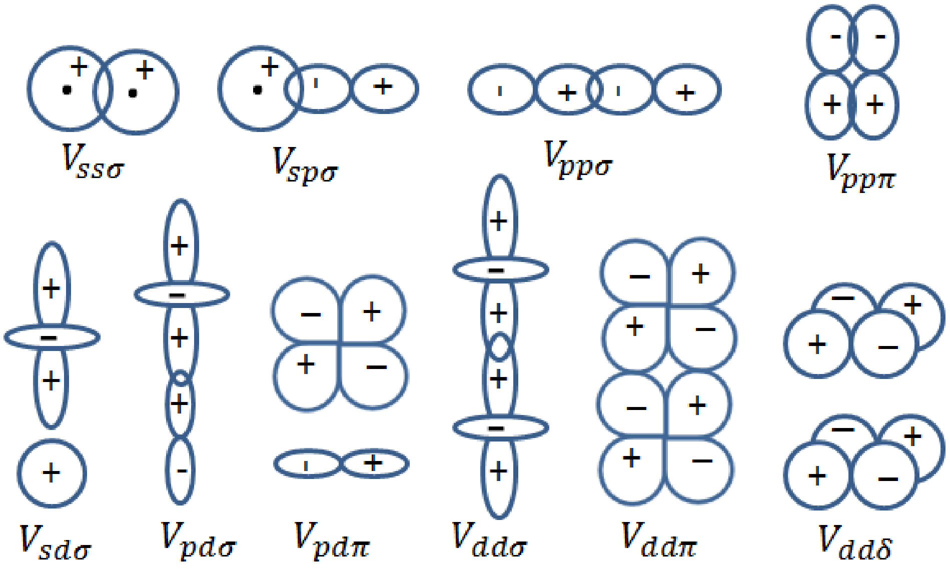

Figure 55: Schematic presentation of the interatomic matrix elements between s, p and d-states

Table-A1, The Slater-Koster hopping matrix elements for the s-, p- and d-orbitals at different relative positions of two atoms. The position between atoms is characterized by vector $\vec{d} = [l, m, n]d$, where $[l, m, n]$ is the unit vector.[126] Only independent matrix elements are given. Other matrix elements can be obtained from them by axis permutations ($n \leftrightarrow m$, etc.).

$E_{s,s} = V_{ss\sigma}$

$E_{s,x} = lV_{sp\sigma}$

$$E_{x,x} = l^2 V_{pp\sigma} + (1 - l^2) V_{pp\pi}$$

$$E_{x,y} = lmV_{pp\sigma} - lmV_{pp\pi}$$

$$E_{x,z} = lnV_{pp\sigma} - lnV_{pp\pi}$$

$$E_{s,xy} = \sqrt{3} lmV_{sd\sigma}$$

$$E_{s,x^2-y^2} = \frac{1}{2}\sqrt{3}(l^2 - m^2)V_{sd\sigma}$$

$$E_{s,3z^2-r^2} = [n^2 - \frac{1}{2}(l^2 + m^2)V_{sd\sigma}$$

$$E_{x,xy} = \sqrt{3} l^2 mV_{pd\sigma} + m(1 - 2l^2)V_{pd\pi}$$

$$E_{x,yz} = \sqrt{3} lmnV_{pd\sigma} + 2lmnV_{pd\pi}$$

$$E_{x,zx} = \sqrt{3} l^2 nV_{pd\sigma} + n(1 - 2l^2)V_{pd\pi}$$

$$E_{x,x^2-y^2} = \frac{1}{2}\sqrt{3} l(l^2 - m^2)V_{pd\sigma} + l(1 - l^2 + m^2)V_{pd\pi}$$

$$E_{y,x^2-y^2} = \frac{1}{2}\sqrt{3} m(l^2 - m^2)V_{pd\sigma} - m(1 + l^2 - m^2)V_{pd\pi}$$

$$E_{z,x^2-y^2} = \frac{1}{2}\sqrt{3} n(l^2 - m^2)V_{pd\sigma} - n(l^2 - m^2)V_{pd\pi}$$

$$E_{x,3z^2-r^2} = l[n^2 - \frac{1}{2}(l^2 + m^2)V_{pd\sigma} - \sqrt{3} ln^2 V_{pd\pi}$$

$$E_{y,3z^2-r^2} = m[n^2 - \frac{1}{2}(l^2 + m^2)V_{pd\sigma} - \sqrt{3} mn^2 V_{pd\pi}$$

$$E_{z,3z^2-r^2} = n[n^2 - \frac{1}{2}(l^2 + m^2)V_{pd\sigma} + \sqrt{3}n(l^2 + m^2)V_{pd\pi}$$

$$E_{xy,xy} = 3l^2m^2V_{dd\sigma} + (l^2 + m^2 - 4l^2m^2)V_{dd\pi} + (n^2 + l^2m^2)V_{dd\delta}$$

$$E_{xy,yz} = 3lm^2nV_{dd\sigma} + ln(1 - 4m^2)V_{dd\pi} + ln(m^2 - 1)V_{dd\delta}$$

$$E_{xy,zx} = 3l^2mnV_{dd\sigma} + mn(1 - 4l^2)V_{dd\pi} + mn(l^2 - 1)V_{dd\delta}$$

$$E_{xy,x^2-y^2} = \frac{3}{2}lm(l^2 - m^2)V_{dd\sigma} + 2lm(m^2 - l^2)V_{dd\pi} + \frac{1}{2}lm(l^2 - m^2)V_{dd\delta}$$

$$E_{yz,x^2-y^2} = \frac{3}{2}mn(l^2 - m^2)V_{dd\sigma} - mn[1 + 2(l^2 - m^2)]V_{dd\pi} + mn[1 + \frac{1}{2}(l^2 - m^2)]V_{dd\delta}$$

$$E_{zx,x^2-y^2} = \frac{3}{2}nl(l^2 - m^2)V_{dd\sigma} + nl[1 - 2(l^2 - m^2)]V_{dd\pi} - nl[1 - \frac{1}{2}(l^2 - m^2)]V_{dd\delta}$$

$$E_{xy,3z^2-r^2} = \sqrt{3}lm\left[n^2 - \frac{1}{2}(l^2 + m^2)\right]V_{dd\sigma} - 2\sqrt{3}lmn^2V_{dd\pi} + \frac{1}{2}\sqrt{3}lm(1 + n^2)]V_{dd\delta}$$

$$E_{yz,3z^2-r^2} = \sqrt{3}mn\ \left[n^2 - \frac{1}{2}(l^2 + m^2)\right]V_{dd\sigma} + \sqrt{3}mn(l^2 + m^2 - n^2)V_{dd\pi} - \frac{1}{2}\sqrt{3}mn(l^2 + m^2)]V_{dd\delta}$$

$$E_{zx,3z^2-r^2} = \sqrt{3}ln\left[n^2 - \frac{1}{2}(l^2 + m^2)\right]V_{dd\sigma} + \sqrt{3}ln(l^2 + m^2 - n^2)V_{dd\pi} - \frac{1}{2}\sqrt{3}ln(l^2 + m^2)]V_{dd\delta}$$

$$E_{x^2-y^2x^2-y^2} = \frac{3}{4}(l^2 - m^2)^2V_{dd\sigma} + [l^2 + m^2 - (l^2 - m^2)^2]V_{dd\pi} + \left[n^2 + \frac{1}{4}(l^2 - m^2)^2\right]V_{dd\delta}$$

$$E_{x^2-y^2,3z^2-r^2} = \frac{1}{2}\sqrt{3}(l^2 - m^2)\left[n^2 - \frac{1}{2}(l^2 + m^2)\right]V_{dd\sigma} + \sqrt{3}n^2(m^2 - l^2)V_{dd\pi} + \frac{1}{4}\sqrt{3}(1 + n^2)(l^2 - m^2)V_{dd\delta}$$

$$E_{3z^2-r^2,3z^2-r^2} = \left[n^2 - \frac{1}{2}(l^2+m^2)\right]^2 V_{dd\sigma} + 3n^2(l^2+m^2)V_{dd\pi} + \frac{3}{4}(l^2+m^2)^2 V_{dd\delta}$$

APPENDIX B: PADE APPROXIMATION

To solve the DMFT equations for the self-energy Σ and Green function G in real frequency representation is rather complicated problem. The self-energy $\Sigma(i\omega_n)$ and Green function $G(i\omega_n)$ in the DMFT formalism are usually calculated by using the imaginary (Matsubara) frequency representation, for fermions $i\omega_n = i2\pi T(2n+1)$, n are integers. Then, to get the spectral function and other physical quantities, one needs to know the Green function and self-energy for real frequencies, for which it is necessary to perform an analytical continuation of the results by using $i\omega_n \rightarrow \omega + i\delta$. There are different ways to perform such a continuation. We use probably the most popular one, based on the Pade approximation [123].

The main idea of the Pade approximation is the following. Let us assume that we know the values u of a function *C* of complex variable z, at M points $z_i(i = 1{,}2 \ldots \ldots \ldots, M)$:

$$C_N(z_i) = u_i. \tag{B.1}$$

In order to extend the function to any other value of the variable z, Pade proposed to approximate it in terms of fractional expansion in complex variable z:

$$C_N(z) = \frac{a_1}{1+\frac{a_2(z-z_2)}{1+\cdots.\frac{a_N(z-z_{N-1})}{1}}} \tag{B.2}$$

(N is the order of expansion).

Indeed, this function automatically satisfies $C_N(z_i) = u_i$. Using these results, one can write down M complex equations that connect the unknown parameters $a_1 to\ a_N$ with values u_i.

The solution for the coefficients a_i can be obtained by the recursion procedure as follows.

1. Define

$$a_1 = g_1(z_1),\ a_2 = g_2(z_2),\ a_3 = g_3(z_3)\ ,\ldots\ldots\ldots\ldots.,\ a_N = g_N(z_N), \quad \text{(B.3)}$$

where $g_1(z_1) = u_1, g_1(z_2) = u_2, g_1(z_3) = u_3, \dots \dots \dots \dots, g_1(z_N) = u_N$. (B.4)

2. It can be shown that the unknown parameters a_i are equal to $g_i(z_i)$, The values for $g_i(z_i)$ can be obtained by using the recursive procedure:

$$g_2(z) = \frac{g_1(z_1) - g_1(z)}{(z - z_1)g_1(z)}\ ,\quad g_3(z) = \frac{g_2(z_2) - g_2(z)}{(z - z_2)g_2(z)}\ ,\quad g_4(z) = \frac{g_3(z_3) - g_3(z)}{(z - z_3)g_3(z)},$$

$$g_p(z) = \frac{g_{p-1}(z_{p-1}) - g_{p-1}(z)}{(z - z_{p-1})g_{p-1}(z)} \dots \dots \quad \text{(B.5)}$$

3. Then the analytically continued function can be written as:

$$C_N(z) = \frac{A_N(z)}{B_N(z)}, \quad \text{(B.6)}$$

where the expressions for the polynomial functions $A_N(z)$ and $B_N(z)$ for large N can be obtained by using $A_0 = 0,\ A_1 = a_1, B_0 = B_1 = 1$ in the following recursive formula:

$$A_{n+1}(z) = A_n(z) + (z - z_n)a_{n+1}A_{n-1}(z),$$

$$B_{n+1}(z) = B_n(z) + (z - z_n)a_{n+1}B_{n-1}(z). \quad \text{(B.7)}$$

Changing *n* from *1* to *N-1* in the last two expression will give the values for $A_N(z)$ and $B_N(z)$, the analytically continued function $C_N(z)$ Eq. (B.6) for any desired value of the complex variable z.

REFERENCES

[1] A. Asamitsu, Y. Tomioka, H. Kuwahara, Y. Tokura, Nature 388 (1997) 50.

[2] P. Fulde, Correlated Electrons in Quantum Matter, World Scientific, New Jersey • London• Singapore, 2012.

[3] L. Xiao, B. Tollberg, X. Hu, L. Wang, The Journal of chemical physics 124 (2006) 114309.

[4] A.T. Bell, Science 299 (2003) 1688.

[5] E. Ozbay, Science 311 (2006) 189.

[6] R. Elghanian, J.J. Storhoff, R.C. Mucic, R.L. Letsinger, C.A. Mirkin, Science 277 (1997) 1078.

[7] S.E. Lee, L.P. Lee, Current Opinion in Biotechnology 21 (2010) 489.

[8] I.M.L. Billas, A. Châtelain, W.A. de Heer, Science 265 (1994) 1682.

[9] J. Lyubina, B. Rellinghaus, O. Gutfleisch, M. Albrecht, Handbook of Magnetic Materials, Vol. 19, edited by KHJ Buschow. Amsterdam: Elsevier, 2011.

[10] S. Sun, C.B. Murray, D. Weller, L. Folks, A. Moser, Science 287 (2000) 1989.

[11] R.S. Chaughule, S. Purushotham, R.V. Ramanujan, Proc. Natl. Acad. Sci., India, Sect. A Phys. Sci. 82 (2012) 257.

[12] C. Alexiou, R. Schmid, R. Jurgons, M. Kremer, G. Wanner, C. Bergemann, E. Huenges, T. Nawroth, W. Arnold, F. Parak, Eur Biophys J 35 (2006) 446.

[13] D.K. Kim, D. Kan, T. Veres, F. Normadin, J.K. Liao, H.H. Kim, S.-H. Lee, M. Zahn, M. Muhammed, Journal of Applied Physics 97 (2005) 10Q918.

[14] J. Henderson, S. Shi, S. Cakmaktepe, T.M. Crawford, Nanotechnology 23 (2012) 185304.

[15] J.P.K. Doye, D.J. Wales, Physical Review Letters 80 (1998) 1357.

[16] R.L. Johnston, Dalton Transactions (2003) 4193.

[17] V. Anisimov, Y. Izyumov, Electronic Structure of Strongly Correlated Materials, Springer, 2010.

[18] M. Imada, A. Fujimori, Y. Tokura, Reviews of Modern Physics 70 (1998) 1039.

[19] V.I. Anisimov, J. Zaanen, O.K. Andersen, Physical Review B 44 (1991) 943.

[20] G. Kotliar, S.Y. Savrasov, K. Haule, V.S. Oudovenko, O. Parcollet, C.A. Marianetti, Reviews of Modern Physics 78 (2006) 865.

[21] V.I. Anisimov, A.I. Poteryaev, M.A. Korotin, A.O. Anokhin, G. Kotliar, Journal of Physics: Condensed Matter 9 (1997) 7359.

[22] W. Metzner, D. Vollhardt, Physical Review Letters 62 (1989) 324.

[23] A. Georges, G. Kotliar, W. Krauth, M.J. Rozenberg, Reviews of Modern Physics 68 (1996) 13.

[24] J.S. Griffith, The theory of transition-metal ions, University Press, Cambridge; England, 1964.

[25] J. Stöhr, H.C. Siegmann, Magnetism : from fundamentals to nanoscale dynamics, Springer, Berlin ; London, 2006.

[26] N.F. Mott, Proceedings of the Physical Society 47 (1935) 571.

[27] J.C. Slater, Physical Review 49 (1936) 537.

[28] E.C. Stoner, Proceedings of the Royal Society of London. Series A, Mathematical and Physical Sciences 165 (1938) 372.

[29] E.C. Stoner, Proceedings of the Royal Society A: Mathematical, Physical and Engineering Sciences 154 (1936) 656.

[30] R. Hoffmann, Solids and Surfaces: A Chemist's View of Bonding in Extended Structures, WILEY-VCH, United States of America, 1988.

[31] J.H.d. Boer, E.J.W. Verwey, Proceedings of the Physical Society 49 (1937) 59.

[32] N.F. Mott, R. Peierls, Proceedings of the Physical Society 49 (1937) 72.

[33] I.M.L. Billas, A. Chatelain, W.A. deHeer, Journal of Magnetism and Magnetic Materials 168 (1997) 64.

[34] I.M.L. Billas, J.A. Becker, A. Chatelain, W.A. Deheer, Physical Review Letters 71 (1993) 4067.

[35] S.E. Apsel, J.W. Emmert, J. Deng, L.A. Bloomfield, Physical Review Letters 76 (1996) 1441.

[36] J.A. Alonso, Structure and Properties of Atomic Nanoclusters, Imperial College Press, Londo, 2012.

[37] J.J. Zhao, X.S. Chen, Q. Sun, F.Q. Liu, G.H. Wang, Physics Letters A 205 (1995) 308.

[38] A. Vega, J. Dorantes-Dávila, L.C. Balbás, G.M. Pastor, Physical Review B 47 (1993) 4742.

[39] J. Friedel, The Physics of Metals, Cambridge University Press, Cambridge, 1969.

[40] G.M. Pastor, J. Dorantesdavila, K.H. Bennemann, Chemical Physics Letters 148 (1988) 459.

[41] P.J. Jensen, K.H. Bennemann, Z Phys D Atom Mol Cl 35 (1995) 273.

[42] G. Rollmann, P. Entel, Lecture Series on Computer and Computational Sciences. ed G Maroulis (Leiden: Brill Academic) 2006, p. 145.

[43] G. Rollmann, P. Entel, S. Sahoo, Computational Materials Science 35 (2006) 275.

[44] G. Kim, Y. Park, M.J. Han, J. Yu, C. Heo, Y.H. Lee, Solid State Communications 149 (2009) 2058.

[45] M.L. Tiago, Y. Zhou, M.M.G. Alemany, Y. Saad, J.R. Chelikowsky, Physical Review Letters 97 (2006) 147201.

[46] S. Florens, Physical Review Letters 99 (2007) 046402.

[47] V. Turkowski, A. Kabir, N. Nayyar, T.S. Rahman, Journal of Physics: Condensed Matter 22 (2010) 462202.

[48] V. Turkowski, A. Kabir, N. Nayyar, T.S. Rahman, The Journal of chemical physics 136 (2012) 114108.

[49] G. Rollmann, H.C. Herper, P. Entel, Journal of Physical Chemestry A 110 (2006) 10799.

[50] T.L. Haslett, K.A. Bosnick, S. Fedrigo, M. Moskovits, The Journal of chemical physics 111 (1999) 6456.

[51] G. Rollmann, P. Entel, Computing Letters 1 (2004) 288.

[52] D.M. Cox, D.J. Trevor, R.L. Whetten, E.A. Rohlfing, A. Kaldor, Physical Review B, Condens Matter 32 (1985) 7290.

[53] K. Boufala, L. Fernández-Seivane, J. Ferrer, M. Samah, Journal of Magnetism and Magnetic Materials 322 (2010) 3428.

[54] L. Xiao, L.C. Wang, Journal of Physical Chemistry A 108 (2004) 8605.

[55] L. Fernandez-Seivane, J. Ferrer, Physical Review Letters 99 (2007) 183401.

[56] H. Ebert, S. Bornemann, J. Minar, P.H. Dederichs, R. Zeller, I. Cabria, Computational Materials Science 35 (2006) 279.

[57] A. Kabir, V. Turkowski, T.S. Rahman, Journal of Physics: Condensed Matter 27 (2015) 125601.

[58] M.B. Knickelbein, Chemical Physics Letters 353 (2002) 221.

[59] S.Y. Jiang, R. Frazier, E.S. Yamaguchi, M. Blanco, S. Dasgupta, Y.H. Zhou, T. Cagin, Y.C. Tang, W.A. Goddard, J Phys Chem B 101 (1997) 7702.

[60] S. Ramachandran, B.L. Tsai, M. Blanco, H. Chen, Y.C. Tang, W.A. Goddard, Langmuir 12 (1996) 6419.

[61] G.E. Brown, V.E. Henrich, W.H. Casey, D.L. Clark, C. Eggleston, A. Felmy, D.W. Goodman, M. Gratzel, G. Maciel, M.I. McCarthy, K.H. Nealson, D.A. Sverjensky, M.F. Toney, J.M. Zachara, Chemical Reviews 99 (1999) 77.

[62] D.A. Dzombak, Surface complexation modeling: hydrous ferric oxide, John Wiley & Sons, 1990.

[63] W. Weiss, W. Ranke, Progress in Surface Science 70 (2002) 1.

[64] X.G. Wang, W. Weiss, S.K. Shaikhutdinov, M. Ritter, M. Petersen, F. Wagner, R. Schlögl, M. Scheffle, Physical Review Letters 81 (1998) 1038.

[65] C.M. Eggleston, American Minerallogist 84 (1999) 1061.

[66] A. Kiejna, T. Pabisiak, Journal of Physics: Condensed Matter 24 (2012) 095003.

[67] A. Kiejna, T. Pabisiak, The Journal of Physical Chemistry C 117 (2013) 24339.

[68] L.M. Sandratskii, M. Uhl, J. Kübler, Journal of Physics: Condensed Matter 8 (1996) 983.

[69] A. Bandyopadhyay, J. Velev, W. Butler, S. Sarker, O. Bengone, Physical Review B 69 (2004).

[70] V. Mazurenko, V. Anisimov, Physical Review B 71 (2005).

[71] G. Rollmann, A. Rohrbach, P. Entel, J. Hafner, Physical Review B 69 (2004) 165107.

[72] J. Kunes, A.V. Lukoyanov, V.I. Anisimov, R.T. Scalettar, W.E. Pickett, Nature materials 7 (2008) 198.

[73] J. Kunes, D.M. Korotin, M.A. Korotin, V.I. Anisimov, P. Werner, Physical Review Letters 102 (2009) 146402.

[74] C. Antoniak, J. Lindner, M. Spasova, D. Sudfeld, M. Acet, M. Farle, K. Fauth, U. Wiedwald, H.G. Boyen, P. Ziemann, F. Wilhelm, A. Rogalev, S. Sun, Physical Review Letters 97 (2006) 117201.

[75] R.P. Cowburn, Journal of Applied Physics 93 (2003) 9310.

[76] J.M.D. Coey, Rare-earth iron permanent magnets, Oxford University Press, 1996.

[77] G.H. Daalderop, P.J. Kelly, M.F. Schuurmans, Physical review. B, Condensed matter 44 (1991) 12054.

[78] I.V. Solovyev, P.H. Dederichs, I. Mertig, Physical Review B 52 (1995) 13419.

[79] A.B. Shick, O.N. Mryasov, Physical Review B 67 (2003) 172407.

[80] D.R. Hartree, Proceedings of the Cambridge Philosophical Society 24 (1928) 89.

[81] P. Hohenberg, W. Kohn, Physical Review 136 (1964) B864.

[82] W. Kohn, L.J. Sham, Physical Review 140 (1965) 1133.

[83] J.P. Perdew, A. Zunger, Physical Review B 23 (1981) 5048.

[84] O. Gunnarsson, M. Jonson, B.I. Lundqvist, Physical Review B 20 (1979) 3136.

[85] E.K.U. Gross, R.M. Dreizler, Z Phys a-Hadron Nucl 302 (1981) 103.

[86] J.P. Perdew, Physical Review Letters 55 (1985) 1665.

[87] J.P. Perdew, K. Burke, M. Ernzerhof, Physical Review Letters 77 (1996) 3865.

[88] J.P. Perdew, J.A. Chevary, S.H. Vosko, K.A. Jackson, M.R. Pederson, D.J. Singh, C. Fiolhais, Physical Review B 46 (1992) 6671.

[89] K. Terakura, T. Oguchi, A.R. Williams, J. Kubler, Physical Review B 30 (1984) 4734.

[90] M. Cococcioni, S. de Gironcoli, Physical Review B 71 (2005).

[91] S.V. Vonsovskii, M.I. Katsnelson, A.V. Trefilov, The Physics of Metals and Metallography 76 (1993) 247.

[92] S.V. Vonsovskii, M.I. Katsnelson, A. V.Trefilov, The Physics of Metals and Metallography 76 (1993) 343.

[93] D. Sarma, N. Shanthi, S. Barman, N. Hamada, H. Sawada, K. Terakura, Physical Review Letters 75 (1995) 1126.

[94] A. Yanase, K. Siratori, Journal of Physical Society of Japan 53 (1984) 312.

[95] Z. Zhang, S. Satpathy, Physical Review B Condens Matter 44 (1991) 13319.

[96] A.I. Liechtenstein, V.V. Anisimov, J. Zaanen, Physical Review B Condens Matter 52 (1995) R5467.

[97] I.A. Vladimir, F. Aryasetiawan, A.I. Lichtenstein, Journal of Physics: Condensed Matter 9 (1997) 767.

[98] J. Kohanoff, Electronic Structure Calculations for Solids and Molecules Theory and Computational Methods, Cambridge University Press, 2006.

[99] M.S. Hybertsen, S.G. Louie, Physical Review Letters 55 (1985) 1418.

[100] A.L. Fetter, J.D. Walecka, Quantum Theory of Many-Particle Systems, McGrow-Hill Book Company.

[101] L. Hedin, Physical Review 139 (1965) A796.

[102] M.S. Hybertsen, S.G. Louie, Physical review. B, Condensed matter 32 (1985) 7005.

[103] J.K. Freericks, M. Jarrell, D.J. Scalapino, Physical review. B, Condensed matter 48 (1993) 6302.

[104] M. Potthoff, W. Nolting, Physical Review B 60 (1999) 7834.

[105] M. Potthoff, Eur Phys J B 36 (2003) 335.

[106] J.K. Freericks, V.M. Turkowski, V. Zlatic, Physical Review Letters 97 (2006) 266408.

[107] H. Aoki, N. Tsuji, M. Eckstein, M. Kollar, T. Oka, P. Werner, Reviews of Modern Physics 86 (2014) 779.

[108] K. Held, I.A. Nekrasov, G. Keller, V. Eyert, N. Blumer, A.K. McMahan, R.T. Scalettar, T. Pruschke, V.I. Anisimov, D. Vollhardt, Phys Status Solidi B 243 (2006) 2599.

[109] A.I. Lichtenstein, M.I. Katsnelson, Physical Review B 57 (1998) 6884.

[110] J.C. Lashley, A. Lawson, R.J. McQueeney, G.H. Lander, Physical Review B 72 (2005) 054416.

[111] S.Y. Savrasov, G. Kotliar, E. Abrahams, Nature 410 (2001) 793.

[112] J. Hubbard, Proceedings of the Royal Society of London. Series A. Mathematical and Physical Sciences 276 (1963) 238.

[113] M.C. Gutzwiller, Physical Review Letters 10 (1963) 159.

[114] J. KANAMORI, Progress of Theoretical Physics 30 (1963) 275.

[115] E.R. Ylvisaker, PhD Thesis, University of California Davis, 2008.

[116] J.E. Hirsch, R.M. Fye, Physical Review Letters 56 (1986) 2521.

[117] M. Feldbacher, K. Held, F.F. Assaad, Physical review letters 93 (2004) 136405.

[118] A.N. Rubtsov, V.V. Savkin, A.I. Lichtenstein, Physical Review B 72 (2005) 035122.

[119] P. Werner, A. Comanac, L. de' Medici, M. Troyer, A.J. Millis, Physical Review Letters 97 (2006) 076405.

[120] M. Jarrell, Physical review letters 69 (1992) 168.

[121] R. Helmes, PhD Thesis, Universität zu Köln, 2008.

[122] J. Rammer, Quantum Field Theory of Non-equilibrium States, Cambridge University Press, United States of America, 2007.

[123] H.J. Vidberg, J.W. Serene, Journal of Low Temperature Physics 29 (1977) 179.

[124] H. Kajueter, G. Kotliar, Physical review letters 77 (1996) 131.

[125] M. Potthoff, T. Wegner, W. Nolting, Physical Review B 55 (1997) 16132.

[126] J.C. Slater, G.F. Koster, Physical Review 94 (1954) 1498.

[127] T. Volodymyr, K. Alamgir, N. Neha, S.R. Talat, Journal of Physics: Condensed Matter 22 (2010) 462202.

[128] G. Kresse, J. Hafner, Physical Review B 47 (1993) 558.

[129] S.H. Vosko, L. Wilk, M. Nusair, Canadian Journal of Physics 58 (1980) 1200.

[130] G. Kresse, D. Joubert, Physical Review B 59 (1999) 1758.

[131] G. Paolo, B. Stefano, B. Nicola, C. Matteo, C. Roberto, C. Carlo, C. Davide, L.C. Guido, C. Matteo, D. Ismaila, C. Andrea Dal, G. Stefano de, F. Stefano, F. Guido, G. Ralph, G. Uwe, G. Christos, K. Anton, L. Michele, M.-S. Layla, M. Nicola, M. Francesco, M. Riccardo, P. Stefano, P. Alfredo, P. Lorenzo, S. Carlo, S. Sandro, S. Gabriele, P.S. Ari, S. Alexander, U. Paolo, M.W. Renata, Journal of Physics: Condensed Matter 21 (2009) 395502.

[132] D.J. Wales, J.P. K.Doye, A. Dullweber, M.P. Hodges, F.Y. Naumkin, F. Calvo, J. Hernández-Rojas, T.F. Middleton, The Cambridge Cluster Database.

[133] M.W. Finnis, J.E. Sinclair, Philosophical Magazine A 50 (1984) 45.

[134] A. Grechnev, I. Di Marco, M.I. Katsnelson, A.I. Lichtenstein, J. Wills, O. Eriksson, Physical Review B 76 (2007) 035107.

[135] D. Chandesris, J. Lecante, Y. Petroff, Physical Review B 27 (1983) 2630.

[136] A. Gutiérrez, M.F. López, Physical Review B 56 (1997) 1111.

[137] P. Gambardella, S. Rusponi, M. Veronese, S.S. Dhesi, C. Grazioli, A. Dallmeyer, I. Cabria, R. Zeller, P.H. Dederichs, K. Kern, C. Carbone, H. Brune, Science 300 (2003) 1130.

[138] J.T. Lau, A. Föhlisch, R. Nietubyc̀, M. Reif, W. Wurth, Physical Review Letters 89 (2002) 057201.

[139] V. Madhavan, W. Chen, T. Jamneala, M.F. Crommie, N.S. Wingreen, Science 280 (1998) 567.

[140] W.A. Harrison, Elementary Electronic Structure, World Scientific, Singapore, 2004.

[141] P.A. Montano, G.K. Shenoy, Solid State Communications 35 (1980) 50.

[142] H. Purdum, P.A. Montano, G.K. Shenoy, T. Morrison, Physical Review B 25 (1982) 4412.

[143] M. Castro, C. Jamorski, D.R. Salahub, Chemical Physics Letters 271 (1997) 133.

[144] T. Oda, A. Pasquarello, R. Car, Physical Review Letters 80 (1998) 3622.

[145] Z. Sljivancanin, A. Pasquarello, Physical Review Letters 90 (2003) 247202.

[146] R.M. Cornell, U. Schwertmann, The Iron Oxides: Structure, Properties, Reactions, Occurences and Uses, WILEY-VCH, 2003.

[147] A.S. Teja, P.-Y. Koh, Progress in Crystal Growth and Characterization of Materials 55 (2009) 22.

[148] G. Wang, T. Liu, Y. Luo, Y. Zhao, Z. Ren, J. Bai, H. Wang, Journal of Alloys and Compounds 509 (2011) L216.

[149] J. Singh, M. Srivastava, J. Dutta, P.K. Dutta, Int. J. Biol. Macromol. 48 (2011) 170.

[150] M.F. Hassan, Z. Guo, Z. Chen, H. Liu, Materials Research Bulletin 46 (2011) 858.

[151] A.K. Gupta, M. Gupta, Biomaterials 26 (2005) 3995.

[152] E.A. Mendoza, D. Sunil, E. Wolkow, H.D. Gafney, M.H. Rafailovich, J. Sokolov, G.G. Long, P.R. Jemian, S.A. Schwartz, B.J. Wilkens, Applied Physics Letters 57 (1990) 209.

[153] B.V. Reddy, S.N. Khanna, Physical Review Letters 93 (2004) 068301.

[154] M.N. Huda, A. Walsh, Y. Yan, S.-H. Wei, M.M. Al-Jassim, Journal of Applied Physics 107 (2010) 123712.

[155] A. Rohrbach, J. Hafner, G. Kresse, Physical Review B 70 (2004) 125426.

[156] A. Bandyopadhyay, J. Velev, W.H. Butler, S.K. Sarker, O. Bengone, Physical Review B 69 (2004).

[157] N.G. Condon, F.M. Leibsle, A.R. Lennie, P.W. Murray, D.J. Vaughan, G. Thornton, Physical Review Letters 75 (1995) 1961.

[158] A. Vladimir, I. Yuri, Electronic Structure of Strongly Correlated Materials, Springer, 2010.

[159] S.L. Dudarev, G.A. Botton, S.Y. Savrasov, C.J. Humphreys, A.P. Sutton, Physical Review B 57 (1998) 1505.

[160] U. Schwertmann, R. M.Cornell, Iron Oxides in the Laboratory Preparation and Characterization, WILEY-VCH, New York, 2000.

[161] R.M. Cornell, U. Schwertmann, The iron oxides: structure, properties, reactions, occurrences and uses, John Wiley & Sons, 2006.

[162] G. Shirane, S.J. Pickart, R. Nathans, Y. Ishikawa, Journal of Physics and Chemistry of Solids 10 (1959) 35.

[163] S. Fysh, P. Clark, Phys Chem Minerals 8 (1982) 257.

[164] N. Dzade, A. Roldan, N. de Leeuw, Minerals 4 (2014) 89.

[165] L.M. Sandratskii, M. Uhl, J. Kübler, Journal of Physics: Condensed Matter 8 (1996) 983.

[166] M. Catti, G. Valerio, R. Dovesi, Physical Review B 51 (1995) 7441.

[167] L.M. Finger, R.M. Hazen, Crystal structure and isothermal compression of Fe2O3,Cr2O3,and V2O3 to 50 bars. , Geophysical Laboratory,Carnegie Institution of Washington,Washinghton,D.C.20008. , 1980.

[168] K. Sivula, F. Le Formal, M. Grätzel, ChemSusChem 4 (2011) 432.

[169] E. Krén, P. Szabó, G. Konczos, Physics Letters 19 (1965) 103.

[170] P. Bruno, Physical Review B 39 (1989) 865.

[171] X. Wang, R. Wu, D. Wang, A.J. Freeman, Physical review. B, Condensed matter 54 (1996) 61.

[172] R. Wu, A.J. Freeman, Journal of Magnetism and Magnetic Materials 200 (1999) 498.

[173] G.H. Daalderop, P.J. Kelly, M.F. Schuurmans, Physical review. B, Condensed matter 41 (1990) 11919.

[174] J.G. Gay, R. Richter, Physical Review Letters 56 (1986) 2728.

[175] J.N. W. Karas, and L. Fritsche, J. Chim. Phys. Phys.-Chim. Biol. 86 (1989) 861.

[176] S. Okamoto, N. Kikuchi, O. Kitakami, T. Miyazaki, Y. Shimada, K. Fukamichi, Physical Review B 66 (2002) 024413.

[177] J.U. Thiele, L. Folks, M.F. Toney, D.K. Weller, Journal of Applied Physics 84 (1998) 5686.

[178] A. Shick, O. Mryasov, Physical Review B 67 (2003).

[179] T. Shima, T. Moriguchi, S. Mitani, K. Takanashi, Applied Physics Letters 80 (2002) 288.

[180] S. Rohart, C. Raufast, L. Favre, E. Bernstein, E. Bonet, V. Dupuis, Physical Review B 74 (2006).

[181] J. Miyawaki, D. Matsumura, H. Abe, T. Ohtsuki, E. Sakai, K. Amemiya, T. Ohta, Physical Review B 80 (2009).

[182] C. Barreteau, D. Spanjaard, Journal of physics: Condensed matter 24 (2012) 406004.

[183] P. Blonski, J. Hafner, Journal of physics: Condensed matter 21 (2009) 426001.

[184] D. Hobbs, G. Kresse, J. Hafner, Physical Review B 62 (2000) 11556.

[185] M. Marsman, J. Hafner, Physical Review B 66 (2002).

[186] J. Lyubina, I. Opahle, M. Richter, O. Gutfleisch, K.-H. Müller, L. Schultz, O. Isnard, Applied Physics Letters 89 (2006) 032506.

[187] R.P. Andres, T. Bein, M. Dorogi, S. Feng, J.I. Henderson, C.P. Kubiak, W. Mahoney, R.G. Osifchin, R. Reifenberger, Science 272 (1996) 1323.

[188] A.R. Mackintosh, O.K. Andersen, Electrons at the Fermi Surface Cambridge University Press, Cambridge, 1980.

[189] P. Blonski, J. Hafner, Journal of Physics: Condensed matter 21 (2009) 426001.

[190] D. Fritsch, K. Koepernik, M. Richter, H. Eschrig, Journal of Computational Chemistry 29 (2008) 2210.

[191] L. Ferrnandez-Seivane, J. Ferrer, Physical Review Letters 99 (2007) 183401.

[192] M. Müller, P. Erhart, K. Albe, Physical Review B 76 (2007) 155412.

[193] T.T. Järvi, D. Pohl, K. Albe, B. Rellinghaus, L. Schultz, J. Fassbender, A. Kuronen, K. Nordlund, EPL (Europhysics Letters) 85 (2009) 26001.

[194] Y.K. Takahashi, T. Koyama, M. Ohnuma, T. Ohkubo, K. Hono, Journal of Applied Physics 95 (2004) 2690.

[195] T. Miyazaki, O. Kitakami, S. Okamoto, Y. Shimada, Z. Akase, Y. Murakami, D. Shindo, Y. Takahashi, K. Hono, Physical Review B 72 (2005) 144419.

[196] R.M. Wang, O. Dmitrieva, M. Farle, G. Dumpich, M. Acet, S. Mejia-Rosales, E. Perez-Tijerina, M.J. Yacaman, C. Kisielowski, J Phys Chem C 113 (2009) 4395.

[197] R.M. Wang, O. Dmitrieva, M. Farle, G. Dumpich, H.Q. Ye, H. Poppa, R. Kilaas, C. Kisielowski, Physical Review Letters 100 (2008).

[198] C. Antoniak, M. Spasova, A. Trunova, K. Fauth, F. Wilhelm, A. Rogalev, J. Minar, H. Ebert, M. Farle, H. Wende, Journal of Physics: Condensed Matter 21 (2009) 336002.

[199] O. Šipr, M. Košuth, H. Ebert, Physical Review B 70 (2004) 174423.

[200] C. Antoniak, M. Spasova, A. Trunova, K. Fauth, M. Farle, H. Wende, Journal of Physics: Conference Series 190 (2009) 012118.

[201] M.E. Gruner, physica status solidi (a) 210 (2013) 1282.

[202] C. Antoniak, M.E. Gruner, M. Spasova, A.V. Trunova, F.M. Römer, A. Warland, B. Krumme, K. Fauth, S. Sun, P. Entel, M. Farle, H. Wende, Nature Communications 2 (2011) 528.

[203] L. Néel, Ann. Géophys 5 (1949) 99.

[204] S. Maenosono, T. Suzuki, S. Saita, J Magn Magn Mater 320 (2008) 79.

[205] R.E. Camley, D.R. Tilley, Physical Review B 37 (1988) 3413.

[206] C.-b. Rong, D. Li, V. Nandwana, N. Poudyal, Y. Ding, Z.L. Wang, H. Zeng, J.P. Liu, Advanced Materials 18 (2006) 2984.

[207] M. Delalande, M.J.F. Guinel, L.F. Allard, A. Delattre, R. Le Bris, Y. Samson, P. Bayle-Guillemaud, P. Reiss, The Journal of Physical Chemistry C 116 (2012) 6866.

[208] W.A. Harrison, S. Froyen, Physical Review B 21 (1980) 3214.

[209] W.A. Harrison, Physical Review B 24 (1981) 5835.